DOCTOR OF SCIENCES

Development of a sum-frequency generation spectrometer

Mani, Alaa Addin

Award date:
2004

Awarding institution:
University of Namur

FUNDP
Faculté des Sciences
Département de Physique
Laboratoire de Spectroscopie Moléculaire de Surface

Rue de Bruxelles, 61
B-5000 Namur
Tél. +32 (0)81 724706
Fax +32 (0)81 724718
E-mail: aladin.mani@fundp.ac.be
Site Web: www.sciences.fundp.ac.be/physique/lasmos

Development of a Sum-Frequency Generation Spectrometer

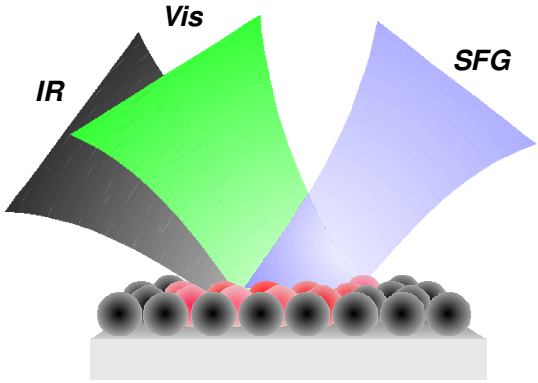

Dissertation présentée par
Alaa Addin MANI
en vue de l'obtention du grade
de Docteur en Sciences
2004

Composition du Jury:

Prof. Ghislain BLANQUET

Dr Eric FREYSZ

Prof. Etienne GOOVAERTS

Dr André PEREMANS

Prof. Paul THIRY (Promoteur)

Rempart de la Vierge, 13
B - 5000 Namur (Belgique)

Imprimé en Belgique
ISBN: 2-87037-448-8
Dépôt légal: D / 2004 / 1881 / 22

Facultés Universitaires Notre-Dame de la Paix
Faculté des Sciences
rue de Bruxelles, 61, B-5000 Namur, Belgium

Développement d'un spectromètre de génération de fréquence-somme

par Alaa Addin MANI

Résumé: Cette thèse est le fruit de plusieurs années de travail passées à développer un spectromètre de génération de fréquence somme dans le laboratoire LASMOS. Ce spectromètre comprend essentiellement deux lasers accordables, un échantillon non linéaire et un monochromateur. Mélanger les deux faisceaux laser accordables sur l'échantillon non linéaire résulte en la génération d'une onde supplémentaire de fréquence égale à la somme des deux fréquences incidentes (SFG). Détecter le signal SFG et accorder une, ou les deux fréquences, permettent la caractérisation de la réponse non linéaire de l'échantillon. Dans notre montage, le premier faisceau laser est accordable dans l'infrarouge de 2,5 jusqu'à 20 µm et le deuxième est accordable dans la région visible de 400 à 700 nm. La génération des deux faisceaux laser accordables est faite par des oscillateurs paramétriques optiques (OPO) qui sont construits autour de cristaux de $LiNbO_3$, d'$AgGaS_2$ et de BBO. Une étape supplémentaire de génération de fréquence différence (DFG) étend l'accordabilité de 10 à 20 µm. L'étape de la DFG est basée sur un tandem de cristaux non linéaire de KTP et de CdSe. Une structure en train d'impulsions est nécessaire pour pomper optiquement le système de l'OPO. Le train d'impulsions peut être engendré par la technique de verrouillage des modes. Nous avons focalisé notre travail sur le verrouillage des modes de l'oscillateur Nd:YAG par le miroir non linéaire à doublage de fréquence (FDNLM). Cette dernière technique combinée avec un absorbeur saturable à deux photons (comme une plaquette de GaAs) permet d'obtenir des impulsions optiques courtes et stables à partir d'un laser Nd:YAG pulsé et pompé par des lampes flashes à bas taux de répétition. Des impulsions aussi courtes que 12 ps sont émises à un taux de répétition de 100 MHz. Par ce résultat, nous nous approchons de la limite physique de la durée de l'impulsion dans un oscillateur Nd:YAG. Cette technologie « tout d'état solide » présente les mérites suivants: stabilité photochimique, temps de réponse rapide, applicabilité à une gamme spectrale relativement large et simplicité. Une approche théorique complète également notre étude pour déterminer le domaine d'opération de ce dispositif.

Facultés Universitaires Notre-Dame de la Paix
Faculté des Sciences
rue de Bruxelles, 61, B-5000 Namur, Belgium

Development of a Sum-Frequency Generation spectrometer

By Alaa Addin MANI

Abstract: This thesis describes the efforts of several years devoted to developing a Sum-Frequency Generation spectrometer in the LASMOS laboratory. The Sum-Frequency Generation spectrometer relies mainly on two tunable lasers, a nonlinear sample and a monochromator. Mixing the tunable laser beams on the nonlinear sample will result in the generation of an additional beam at the sum frequency (SFG) of the incident beams. Detecting the SFG signal and tuning one of the incident frequencies or both frequencies permit the characterization of the nonlinear response of the sample. In our setup, the first laser beam is tunable in the IR spectral region from 2.5 up to 20 µm and the second one is tunable in the visible spectral region from 400 to 700 nm. The generation of both tunable laser beams is carried out by the optical parametric oscillators (OPO) built around a $LiNbO_3$, an $AgGaS_2$ and a BBO nonlinear crystals. An additional difference-frequency generation (DFG) stage based on a tandem of KTP and CdSe crystals is built to extend the tunability up to 20 µm. A pulse-train structure is necessary for pumping the OPO. Pulse trains can be generated by the mode-locking technique. In our work, we focused on the mode locking of the Nd:YAG oscillator using a frequency-doubling nonlinear mirror (FDNLM). This technique combined with a two-photon saturable absorber (for example: a GaAs platelet) can generate short and stable optical pulses from a flash-pumped Nd:YAG laser oscillator at a low repetition rate. Pulses as short as 12 ps are generated at 100 MHz repetition rate. With this result, we approach the physical limit of pulse duration in the Nd:YAG laser. This all-solid-state technology presents the following merits: photochemical stability, fast response time, applicability to a wide spectral range, and simplicity. A theoretical model is used to analyze the domain of operation of this device.

To whom I love,

God,

my parents,

my wife,

who constantly support me.

I make a point of thanking the head of LASMOS laboratory, Professor Paul Thiry, for having engaged me in his team and having encouraged me throughout my entire thesis. I will not forget that we have worked together on all illustrations in this thesis; that taught me a lot. Really, I appreciate all that he did for me.

In addition, I would like to thank Dr. André Peremans for supervising my work. Indeed, he initiated the project of the mode locking using a frequency-doubling nonlinear mirror.

I appreciate the efforts of the members of committee for reading with great attention my manuscript and I thank them for being present at the public defense:

- Professor Ghislain Blanquet from the University of Namur and his assistant, Dr. Muriel Lepère;
- Professor Etienne Goovaerts from the University of Antwerp;
- Doctor Eric Freysz, who is Research Director at the Université de Bordeaux 1 in the CPMOH unit;
- Doctor André Peremans, who is a Reaserch Associeted of the FNRS;
- My promoter, Professor Paul Thiry.

A big thank you to the team of the LASMOS laboratory, including the previous members, for their linear solidarity:

Dr. Yves Caudano	Dr. Philippe Hollander	Dr. Christophe Silien
Dr. Jacques Darville	Dr. Christophe Humbert	Dr. Priscilla Simonis
Dr. Laurent Dreesen	Dr. Daniel Lambot	Mr. Cédric Volcke
Eng. Vincent Froidbise	Mr. Jean-Jacques Lemaire	
Mr. Laurent Grawet	Mr. Yannick Sartenaer	

I would like to add a special thank to Dr. Yves Caudano for his particular comments on the written manuscript.

I also thank Mr. Bauduin Thibaut the engineer of Euroscan Instruments for his technical support.

Thanks from the heart to all my friends and neighbors, especially Prof. Peter Kelly for supporting me.

I would like to thank the following laboratories and their members for working together in developing the SFG spectrometer:

- Laboratoire pour l'Utilisation du Rayonnement Electromagnétique (LURE) at Orsay: Dr. Abderrahmane Tadjeddine, Dr. Bertrand Busson, Dr. Catherine Six, and Dr. Franck Vidal.
- The Frederick Seitz Materials Research Laboratory (FS-MRL), University of Illinois at Urbana-Champaign: Prof. Jeffrey O. White, Prof. Andrew A. Gewirth, Dr. G. Q. Lu, and Dr. Zachary Schultz.
- Forschungszentrum Karlsruhe in der Helmholtz-Gemeinschaft: Dr. Mathias Floersheimer and Mr. Klaus Kruse.

At this point, I would like to present my gratitude to the Syrian government and especially the Atomic Energy Commission for allowing me to continue my studies in Belgium and to obtain a Ph.D.

I also take this opportunity to express my gratitude to the Belgian people for their hospitality and their open-mindedness. It is essential that these qualities be shared on our small planet.

Contents

Chapter I Introduction

In this thesis, we present our experimental achievement after several years of working on the development of a sum-frequency generation spectrometer (SFG). A good part of this work focused on improving the performances of the active, passive mode locking of the Nd:YAG oscillator that is used as the injection laser.

Our aim was to develop a SFG spectrometer dedicated to studying the vibrational fingerprint of adsorbed molecules and interfaces on centrosymmetric materials. These measurements do not require ultra-high vacuum conditions and can be realized under normal laboratory environment.

SFG is a nonlinear optical spectroscopy based on a second-order nonlinearity, which requests the use of tunable laser sources in the infrared and visible spectral regions. These tunable sources should provide short optical pulses with narrow bandwidths. The narrow bandwidth ensures a good spectral resolution, and the short pulsewidth permits a good sensitivity and prevents possible optical damage of the sample. In this case, the optical damage of the sample defines the physical limit of the sensitivity.

Nd:YAG lasers are widely used for their reliability and economic features. These systems are readily able to generate short optical pulses with sufficiently narrow bandwidth by employing passive mode-locking techniques. In our laboratory, we began using the saturable dye absorber cell (SDAC) which is a well-established technique for passive mode locking. The nonlinear absorption of saturable absorbers was first successfully employed for simultaneously Q-switching and mode locking of solid-state lasers in 1965.[1,2] The traditional saturable absorber consists of organic dyes that have an absorption at the laser wavelength. For sufficiently intense laser radiation, the ground state of the dye becomes depleted, which decreases the loss in the resonator for increasing pulse intensity. An efficient mode locking of flashlamp-pumped Nd:YAG was reported by A.D. Corno et *al.*[3] where trains of about 90 pulses of 10 ps were generated using a GaAs semiconductor platelet as a passive, negative element inside the laser cavity.

From our experience, mixing and handling the dye solution (involving possible chemical hazard), and maintaining proper dye concentration (to avoid unstable function and possible damage of the optical elements) proved cumbersome. Because of these inherent shortcomings, we replaced this technique by an all-solid-state one that we called frequency-doubling nonlinear mirror (FDNLM) or Stankov mirror. In 1988, Stankov demonstrated the first passive mode locking of a pulsed Nd:YAG laser using a FDNLM.[4] In comparison to other means of passive mode locking, like the use of a saturable dye absorber, this technology presents the following merits: photochemical stability, small response time, applicability to a wide spectral range, simplicity, self-starting mode locking; moreover, it enables passive, positive feedback as well as passive negative one.[2,5,6,7,8,9,10,11,12,13]

The first work on passive, positive mode locking using a FDNLM demonstrated the achievement of pulse duration of 100 ps with a flashlamp-pumped YAG laser.[6] This earliest performance has since been improved to 45 ps and 25 ps pulse duration for the second-harmonic output pulse, using a 6 mm thick KTP crystal[7] and a 8 mm thick BBO SHG crystal,[8] respectively. To our knowledge, the shortest duration ever achieved with that technology applied to a pulsed YAG laser is the 25 ps recently reported by Chekhlov.[9] Briefly, this technique has shown very good performances in continuous wave regime (CW); however, it has presented shortcomings in pulsed wave (PW) regime for generating what we call transform-limited pulses.

In this work, we report on the new performances of the mode locking of a flashlamp-pumped Nd:YAG laser using a frequency-doubling nonlinear mirror combined with a passive, negative element. Pulsewidths between 12 and 8 ps FWHM are generated and we show that the flat shape of the pulse train envelope generated by the oscillator is well adapted for the synchronous pumping of optical parametric oscillators (OPO's). In addition, we show in chapter VI the development of mid-infrared OPO's based on $LiNbO_3$ and $AgGaS_2$ crystals, which permit tuning from 2.5 to 10 μm. Longer wavelengths up to 20 μm can be generated using a KTP OPO operated around the degenerated frequency and followed by difference-frequency generation (DFG) inside a semiconductor crystal like CdSe as shown in Chapter VII.

Scanning the wavelength in the visible spectral region is readily achieved by an OPO built around a β-BBO crystal pumped by the third harmonic of Nd:YAG as we shall see in chapter VIII. The complete view of the experimental setup of the SFG spectrometer will be presented in chapter IX.

Finally, we conclude our work in chapter X and we try to clarify some problems in the appendices.

Chapter II Neodymium-Doped Yttrium Aluminum Garnet Laser Oscillator

In a general way, a laser oscillator consists of a gain medium where the laser* effect takes place under proper conditions and of an optical feedback system that ensures the oscillation of optical waves inside the medium. In this chapter, we will describe the major characteristics of a laser oscillator based on a Nd-doped Yttrium Aluminum Garnet (YAG) crystal, beginning with the description of the material and ending with a general analysis of the setup.

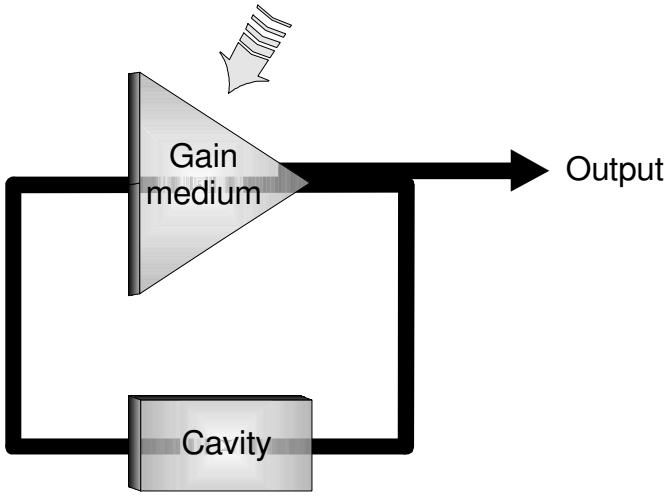

* LASER stands for Light Amplification by Stimulated Emission of Radiation, which designates only the optical amplification process.

Nd:YAG gain medium

The chemical formula of YAG is $Y_3Al_5O_{12}$. The different atoms are distributed in a cubic structure characteristic of *garnets*. The unit cell contains eight $Y_3Al_5O_{12}$ units each one is as that one represented in Figure II-1, where one can find tetrahedral, octahedral and dodecahedral sites. Sixteen octahedral sites and 24 tetrahedral sites are occupied by Al atoms bound to oxygen. The twenty-four Y^{3+} ions occupy dodecahedral sites. About one percent of Y^{3+} ions will be replaced by Nd^{3+} ions, which are responsible for the laser effect. Table II-1 summarizes some selected physical and optical properties of Nd:YAG.[14] The YAG is characterized by a good thermal conductivity as indicated in Table II-2 that gives several thermal properties.

The first lasing with the Nd:YAG crystal has been reported by Geusic *et al.*[15] The Nd:YAG laser is a four-level system as schematized in Figure II-2. Initially, the optical pumping process promotes electrons of the Nd ions from the ground energy level ($^4I_{9/2}$) up to bands situated between 0.75 and 0.8 µm, which are clearly visible in the absorption spectrum of Figure II-1.

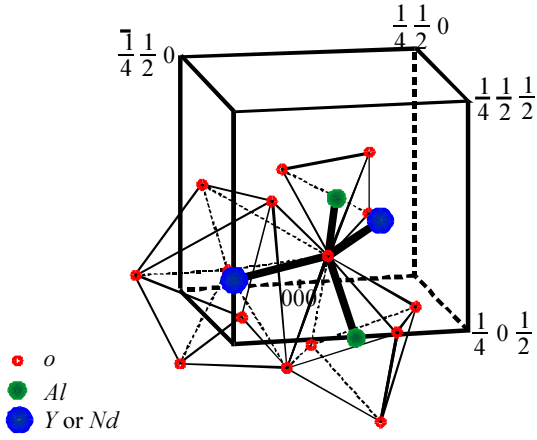

Figure II-1: Motif of one-eighth of the garnet structure of the YAG crystal.

Chemical formula	Nd: $Y_3Al_5O_{12}$
Weight percentage of Nd	0.725
Atomic percentage of Nd	1.0
Nd atoms/cm^3	1.38×10^{20}
Melting point	1970 °C
Knoop hardness	1215
Density	4.56 g/cm^3
Rupture stress	1.3-2.6×10^3 kg/cm^3
Thermal expansion coefficients [100] orientation [110] orientation [111] orientation	 8.2×10^{-6} K^{-1}, 0 - 250 °C 7.7×10^{-6} K^{-1}, 10 - 250 °C 7.8×10^{-6} K^{-1}, 10 - 250 °C
Bandwidth $\Delta\omega_a$	~2π×120 GHz*
Stimulated emission cross section σ_s $R_2 \rightarrow Y_3$ $^4F_{3/2} \quad ^4I_{11/2}$	 6.5×10^{-19} cm^2 2.8×10^{-19} cm^2
Spontaneous fluorescence lifetime	230 μs
Index of refraction	1.82 (at 1.0 μm)
Scatter losses	0.002 cm^{-1}

Table II-1: Physical and optical properties of Nd:YAG.

Property	**Units**	**100 K**	**200 K**	**300 K**
Thermal conductivity	W cm^{-1} K^{-1}	0.58	0.21	0.14
Specific heat	W s g^{-1} K^{-1}	0.13	0.43	0.59
Thermal diffusivity	cm^2 s^{-1}	0.92	0.10	0.046
Thermal expansion	K^{-1}	4.25	5.8	7.5
Thermal variation of refractive index $\partial n/\partial T$	K^{-1}	-	-	7.3×10^{-6}

Table II-2: Thermal properties of Nd:YAG crystal.

* The most cited value. For example, see reference 17.

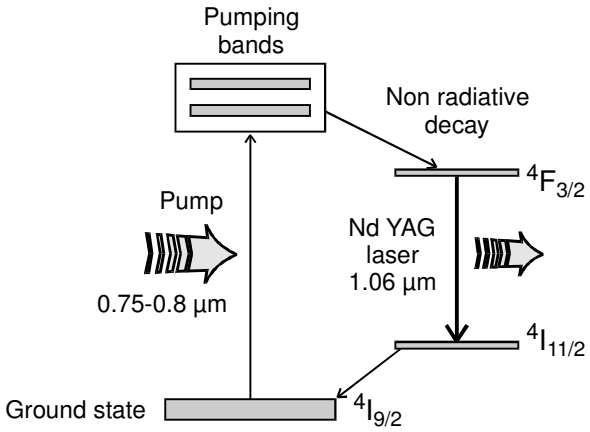

Figure II-2: Energy level diagram of the Nd:YAG and its four-level laser excitation process.

Several absorption bands match the emission of both Krypton and Xenon arc lamps. This makes such flashlamps very efficient for the optical pumping. The excited electrons will rapidly decay to the upper laser level $^4F_{3/2}$ due to nonradiative processes, which introduce an energy loss by transforming part of the pumping energy into heat. The population inversion takes then place between the $^4F_{3/2}$ and $^4I_{11/2}$ levels where the laser effect can occur.

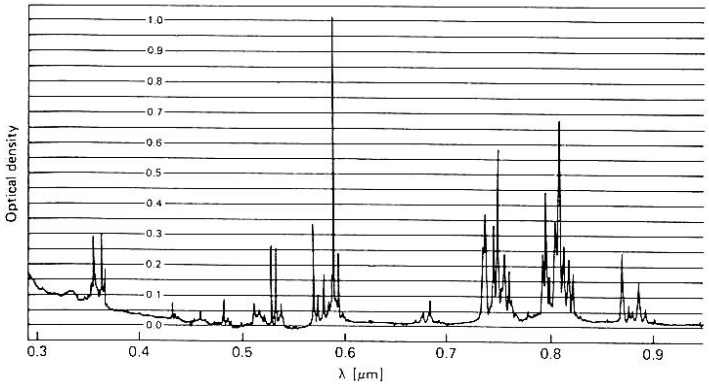

Figure II-3: Absorption spectrum of Nd:YAG at 300 K.

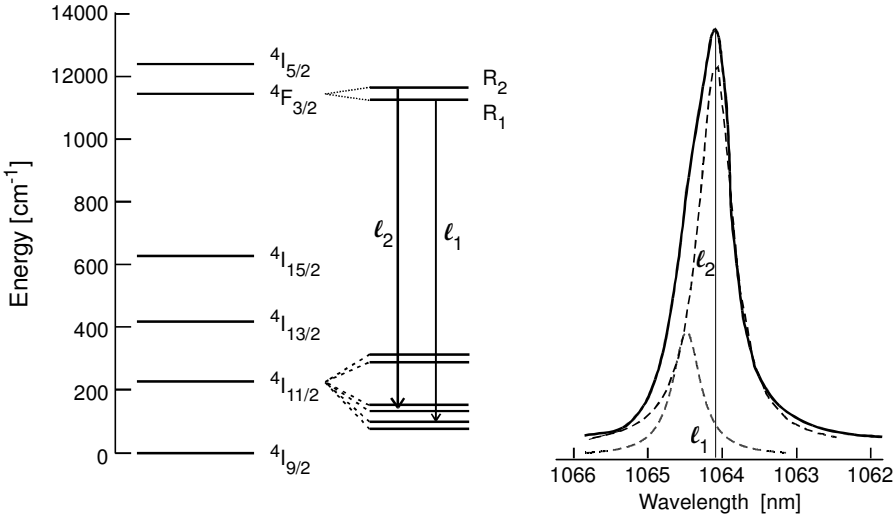

Figure II-4: Emission spectrum of 1.064-μm laser line at room temperature. Two Lorentzian lines contributing to the laser transition are shown by dashed curves.

As shown in the energy diagram (Figure II-4) the $^4F_{3/2}$ level is split into R_2 and R_1. These give rise two Lorentzian lines ℓ_2 at 1.06415 μm and ℓ_1 at 1.0646 μm. Because they are so close to each other, these two lines appear as one single asymmetric one in Figure II-4. The small width of the $^4F_{3/2}$ line indicates a long lifetime of 230 μs appropriate for population inversion. The deexcitation scheme from the $^4F_{3/2}$ level is the following: $^4F_{3/2} \rightarrow {}^4I_{9/2} = 0.25$, $^4F_{3/2} \rightarrow {}^4I_{11/2} = 0.6$, $^4F_{3/2} \rightarrow {}^4I_{13/2} = 0.14$, and $^4F_{3/2} \rightarrow {}^4I_{15/2} < 0.01$. Thus sixty percent of the ions will participate in the lasing laser effect by decaying to the $^4I_{11/2}$ level.

Finally, these electrons will loose their remaining energy by a second nonradiative transition to the ground state $^4I_{9/2}$.

ND:YAG LASER HEAD

The Nd:YAG laser rods are usually grown by the Czochralski method. The rods are cut as cylinders of 114 mm in length and 6, 7 or 9 mm in diameter. The optimum concentration of Nd^{3+} ions in YAG corresponds to the maximum luminescence intensity, which is located around 1.1% as shown in Figure II-5, and to the minimum value of the laser threshold (dashed curve).

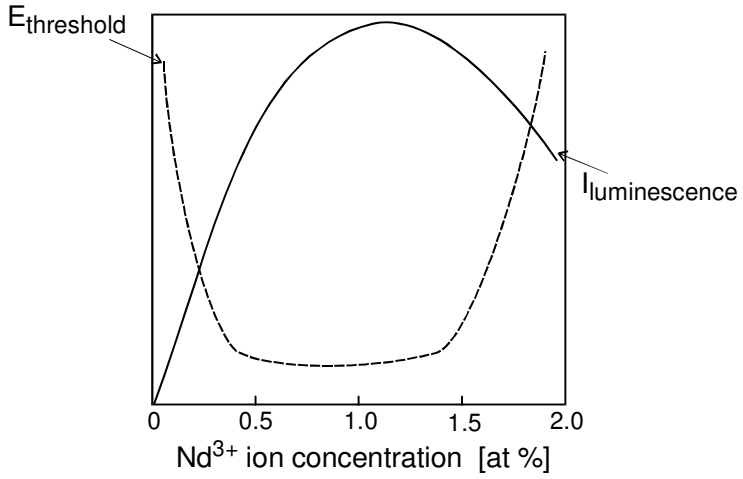

Figure II-5: Luminescence intensity (solid curve) and laser threshold (dotted curve) of the 1.06415 μm line in Nd:YAG crystal.[16]

This fact makes a solid argument in favor of about 1.1% Nd^{3+} concentration value.[16] In order to avoid parasitic oscillations, the rod surfaces are miscut at 1° with respect to the rod axis and they have an antireflection coating in order to minimize reflection losses. The laser rod and the pumping flashlamps are assembled in a laser head as illustrated in Figure II-6. The optical coupling between the laser rod and the flashlamps is done by an elliptical cavity design where the rod and the flashlamp take the foci positions. The oscillator head is pumped by one Krypton flashlamp, whereas two lamps are needed to pump the amplifier rod. A water-cooling system is required to evacuate the heat produced by the flashlamps and the laser rod.

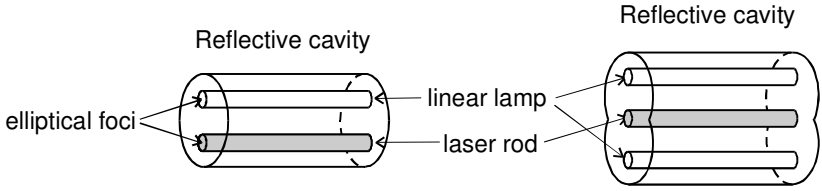

Figure II-6: Flashlamp pumping arrangement for a Nd:YAG rod. On the right side of the figure is presented a configuration of an amplifier head with two flashlamps.

Laser oscillation

Starting the laser oscillations requires the installation of the laser head inside a cavity that, in the simplest case, is delimited by two parallel plane mirrors.

CONDITION FOR BUILD-UP OF LASER OSCILLATION

In the beginning, the gain medium is optically pumped by an appropriate optical source that maintains the population inversion process as long as possible. The steady-state situation can be achieved when the excitation time due to the flashlamp operation is longer than the electron lifetime in the upper laser level as shown in Figure II-7-a. Electron transition from the upper laser level E_2 to the lower level E_1 occurs thanks to a radiative process which in turn creates spontaneous emission of photons with energy equal to $\Delta E = E_2 - E_1$. The latter process does not restrict the direction of emission, which gives a photon emission in all directions as schematized in Figure II-7-b. Some of the generated photons strike one of the parallel mirrors, which reflect them into the laser rod. Inside the rod, the reinjected photon can stimulate an excited electron to liberate its energy as a second photon. This shows the physical process behind the optical amplification with a total yield of two photons for a single incident one; moreover, the two generated photons are coherent. That means they have same energy, same direction of propagation, and same phase as shown in Figure II-7-c.

An avalanche of these multiple coherent photons will build up the radiation inside the laser cavity under the condition that photon generation compensates the photon losses, which are principally introduced by the output mirror. When the laser radiation starts up, a spatial electromagnetic field distribution profile will take place inside the laser cavity, as shown in Figure II-7-d. At this moment, we can speak about electromagnetic distribution field modes regardless of the gain medium. Figure II-7-d shows the build-up of the first order transverse electromagnetic wave TEM_{00}.

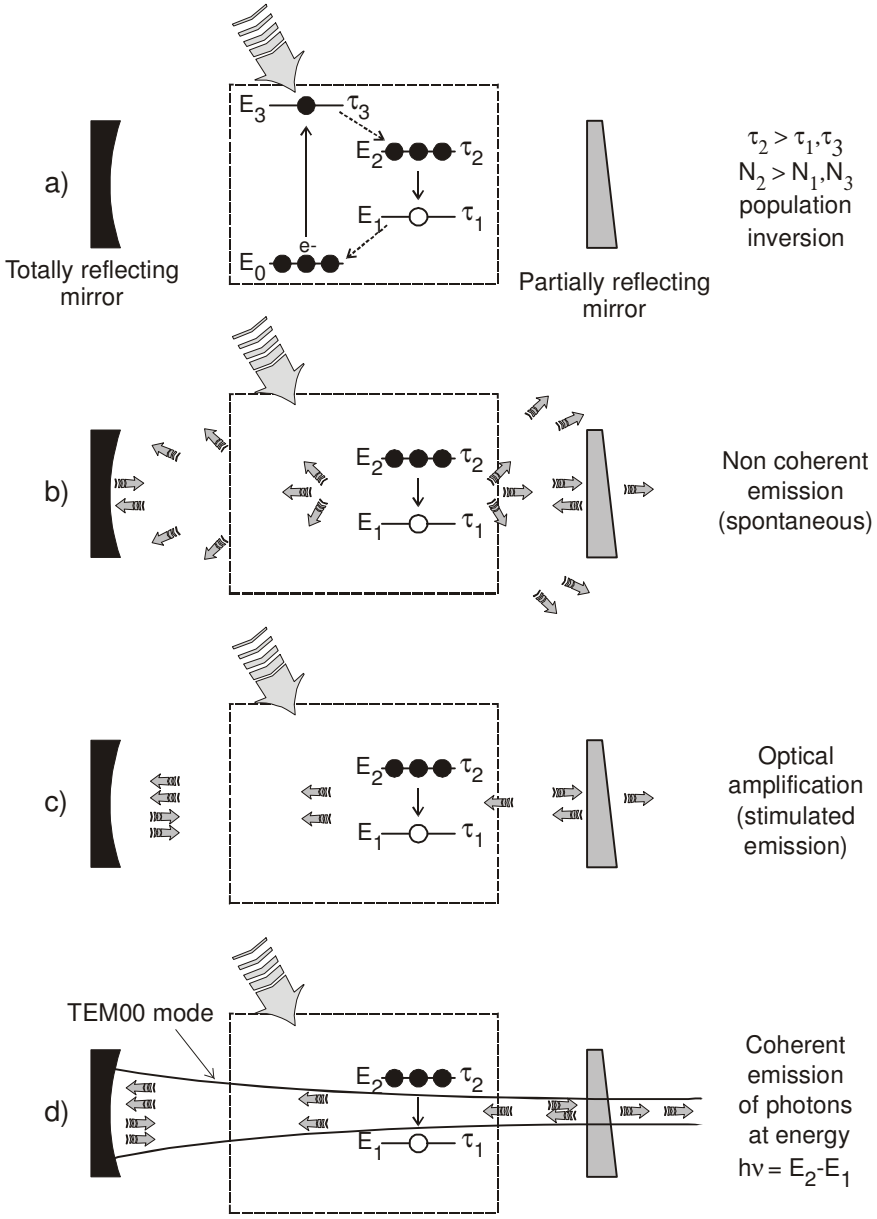

Figure II-7: Dynamics of coherent photon emission:
a) population inversion maintained by the optical pumping,
b) emission of first photons in all directions,
c) cavity feeds back of the photons into the laser rod,
d) beginning of coherent emission by laser effect.

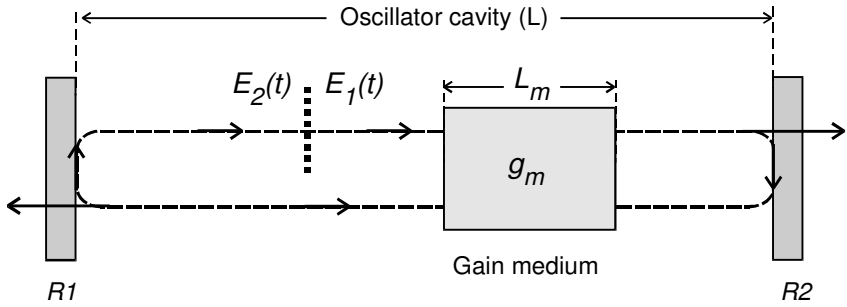

Figure II-8: Round-trip field model of a laser oscillator.

ROUND-TRIP AMPLITUDE CONDITION

Let us analyze the steady-state condition when the electromagnetic (EM) wave makes infinity of round trips inside the cavity without change in the EM field properties like phase or amplitude. Figure II-8 shows a simple model that describes the round-trip conditions inside the laser cavity with spacing L between the mirrors and a gain medium of length L_m.

In mathematical terms, the total amplitude gain and phase shift for a signal wave at frequency ω after one complete round trip must satisfy the following condition:

$$\frac{\tilde{E}_2}{\tilde{E}_1} \equiv r_1 r_2 \exp\left(2g_m - j\frac{2\omega L}{c}\right) = 1 \quad \text{at steady state}, \tag{II.1}$$

where the coefficients r_1 and r_2 ($|r| \le 1$) are the wave-amplitude reflection coefficients of the end mirrors; $exp(2g_m)$ is the round-trip amplitude amplification through the laser gain medium and $exp(-j2\omega L/c)$ the round-trip phase shift around the laser cavity of length L.

As we used here the complex representation of the electric field, we can separate the condition in equation (II.1) into two conditions: one for the phase and the second one for the amplitude. The amplitude condition is

$$r_1 r_2 \exp(2g_m) = 1 \quad \Leftrightarrow \quad 2g_m = \ln\left(\frac{1}{\sqrt{R_1 R_2}}\right) \quad , \tag{II.2}$$

where $R_1 = |r_1|^2$ and $R_2 = |r_2|^2$ are the power reflectivities of the two end mirrors. This condition describes the fact that the amplitude gain should

overcome the loss introduced by the cavity mirrors. The gain coefficient is related to the net inversion population $\Delta N \equiv N_2 - N_1$ and to the stimulated cross section σ_s (see Ref. 14), by the expression

$$g_m = \sigma_s \, \Delta N \, L_m . \tag{II.3}$$

The peak cross section for stimulated emission is written as:

$$\sigma_s = \frac{\lambda^2 \, \gamma_{rad}}{2\pi \, \Delta\omega_a}, \tag{II.4}$$

where $\Delta\omega_a$ is the transition linewidth (see Table II-I), λ is the emission wavelength and γ_{rad} is the radiative decay rate of the upper laser level. Combining the condition (II.2) with the expression (II.3) yields the minimum or threshold population inversion ΔN_{th}

$$\Delta N \equiv N_2 - N_1 \geq \Delta N_{th} \equiv \frac{\pi \, \Delta\omega_a}{\lambda^2 \, \gamma_{rad} \, L_m} \ln\left(\frac{1}{\sqrt{R_1 R_2}}\right). \tag{II.5}$$

The latter equation gives the threshold population inversion ΔN_{th} that must be created by the pumping process; moreover, equations (II.2) and (II.5) give the saturated gain coefficient g_m or the saturated inversion densities ΔN that must just be maintained in order to have unity net gain at steady state. Equation (II.5) makes clear that the laser threshold is low for a narrow transition linewidth $\Delta\omega_a$ and low cavity losses, including $R_1, R_2 \rightarrow 1$. In addition, one can see that the laser action will be more difficult for short wavelengths.

ROUND-TRIP PHASE OR FREQUENCY CONDITION

The phase part of equation (II.1) gives the round-trip *phase shift condition,* which can be expressed by

$$\exp\left(-j\frac{2\omega L}{c}\right) = \exp\left(-jm2\pi\right) \;\Leftrightarrow\; \frac{2\omega L}{c} = m2\pi, \quad \text{with } m \in \mathbb{Z} \tag{II.6}$$

This states that the round-trip phase shift $2\omega L/c$ inside the cavity is an integer multiple of 2π. Introducing the frequency separately in one member of equation (II.6) yields

$$\omega_m \equiv m\Delta\omega \quad \text{with} \quad \Delta\omega = 2\pi\frac{c}{2L}, \tag{II.7}$$

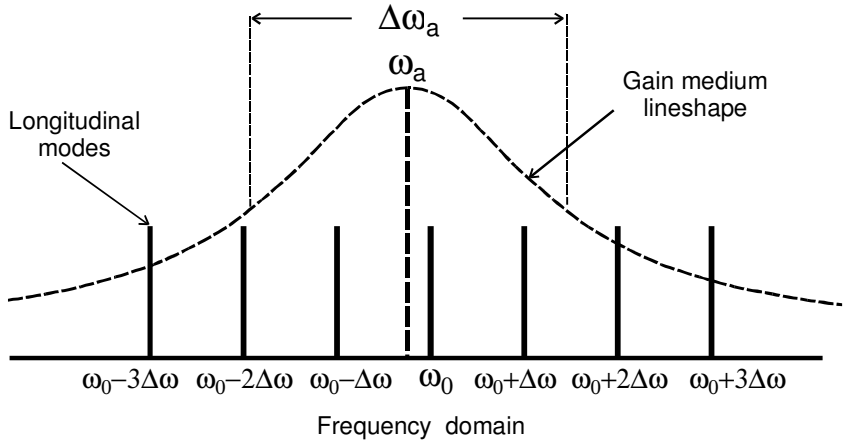

Figure II-9: Longitudinal-mode frequencies under the atomic gain profile in a typical homogeneously broadened gain medium.

where $\Delta\omega$ is the frequency spacing between the oscillating frequencies ω_m. The set of frequencies ω_m where m is an integer is called the *axial-mode frequency set.*

In the case of an optical oscillator, the optical frequency ω_a is about 2.82×10^{14} Hz, which is the laser frequency of the Nd:YAG crystal, one of the axial frequencies ω_0 that corresponds to a very large integer value will oscillate around the optical frequency. This integer value is about 2.82×10^{6} for a round-trip frequency $\Delta\omega$ of $2\pi\times10^{8}$ Hz corresponding to a cavity length of 1.5 m. The number of these axial modes will be limited by the bandwidth of the gain medium. In our Nd:YAG laser, the number of the selected axial modes is of order of 1200[*] taking into account a Nd:YAG bandwidth $\Delta\omega_a$ equal to $2\pi\times120$ GHz. The relevant subset of axial-mode set is called the *longitudinal-mode* set. Figure II-9 illustrates a gain medium homogeneously broadened around the atomic frequency ω_a with atomic linewidth $\Delta\omega_a$, and the oscillating longitudinal modes for which the laser output power is strongly enhanced.

[*] This value is obtained by dividing the bandwidth of Nd:YAG (~120 GHz) by the round-trip frequency of 100 MHz (cavity length of 1.5 m).

Configuration and stability of the laser cavity

In a general way, we can classify the laser cavities into two categories: the stable and the unstable cavity. The stable cavity has a lower laser threshold than the unstable one. This is a major reason for using such a cavity design. Figure II-10 shows a variety of stable cavities consisting of two curved mirrors with radii of curvatures R_1 and R_2, and a separation distance L. Inside these cavities the same lateral spatial distribution (the wavefront) can be reproduced after each round trip. In our work, we use a more complicated cavity design including two lenses and a nonlinear crystal that will be described in a further section. The study of the cavity stability is performed by using a matrix-based analysis for paraxial wave propagation.[17] In addition to the simulation, we take into consideration the thermal effect in the laser rod.

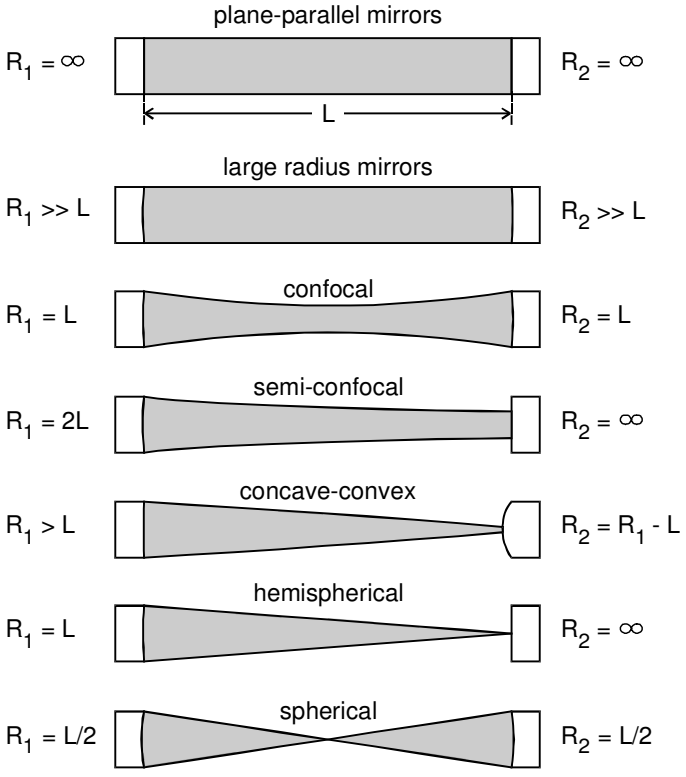

Figure II-10: Possible two-mirror laser cavity configurations indicating the relationship of the radii of curvature of the mirrors with respect to the separation between mirrors.

Concluding remarks

In this chapter, we described the YAG gain medium and its characteristics, the optical pumping mechanism and the condition to obtain stable oscillations inside the laser cavity. The Nd:YAG emits laser radiation at 1064 nm wavelength with maximum bandwidth of 120 GHz. A laser operating in these conditions is called *free running laser*. In order to get a laser beam useful for our purpose, we need to generate intense coherent pulses. This is achieved by the technique of *mode locking* that will be described in the next chapters.

Chapter III Mode-Locked Nd:YAG Oscillator

In this chapter, we shall try to describe briefly the evolution of the laser pulse inside the laser oscillator. We shall obtain some analytical expressions under the steady-state conditions. These expressions give a way of understanding the physical limits of the pulse duration that can be generated by mode-locking techniques.

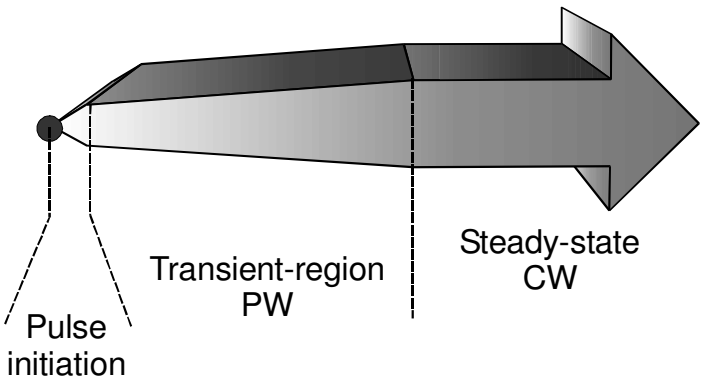

Optical pulse evolution

Linear propagation of Gaussian pulses

In this work, we are interested in the generation of short optical pulses that can be produced thanks to the well-known mode-locking methods. Thus, it seems necessary to introduce the basic theoretical concepts concerning the optical pulse duration. We shall limit our treatment to the steady-state behavior and to Gaussian pulses.

GAUSSIAN PULSES

Physically, the optical pulses generated by mode-locking techniques are readily very close in shape to the Gaussian pulses, as we shall describe in a further section. In addition, the analysis performed on Gaussian pulses will be valid for almost all the pulse shapes.

Let us consider an optical pulse with a carrier frequency ω_0 and a complex Gaussian envelope given by

$$\tilde{E}(t) = e^{-\gamma t^2} e^{j\omega_0 t} \tag{III.1}$$

where the complex Gaussian parameter γ is equal to

$$\gamma = a - j\ b \quad \text{where} \quad a, b \in R\,. \tag{III.2}$$

The instantaneous intensity *I(t)* associated with this pulse can be written as

$$I(t) \approx \left|\tilde{E}(t)\right|^2 = e^{-2a\ t^2} = \exp\left[-\left(\frac{t}{\tau_p}\right)^2 4\ln 2\right]. \tag{III.3}$$

In this form, the time interval τ_p is the full width at half maximum (FWHM) of the pulse intensity function. We shall use τ_p as a measure of the width of the optical pulse. Using the latter definition, we can relate τ_p to a (the real part of the complex Gaussian parameter γ) by

$$\tau_p = \sqrt{\frac{2\ln 2}{a}}\,. \tag{III.4}$$

It is noteworthy that the energy density is proportional to the product of the peak intensity I_{peak} and width τ_p of the pulse. For a Gaussian pulse, the proportionality constant is equal to 1.064,[§] which is practically equal to 1.

[§] It is a pleasure to see the YAG wavelength appearing again here!

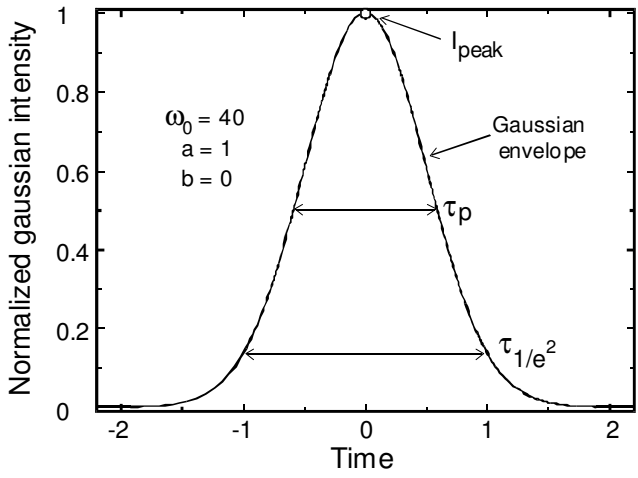

Figure III-1: Intensity of a Gaussian pulse function. The important parameters are the pulsewidth τ_p, the pulse peak intensity I_{peak}, and the pulse duration $\tau_{1/e2}$.

Figure III-1 shows the principal parameters of a Gaussian pulse. Rewriting equation (III.1) with the value of the complex Gaussian parameter yields,

$$\tilde{E}(t) = \exp(-at^2)\exp\left[\, j(\omega_0 t + bt^2)\,\right] = \exp(-at^2)\exp(j\Phi_{tot})\,, \quad \text{(III.5)}$$

where $\Phi_{tot} = \omega_0 t + bt^2$ is the instantaneous relative phase[**] of the pulse, which has a parabolic behavior versus time. Setting the quadratic parameter b to zero retrieves the usual linear case as shown on Figure III-2. The variation of the phase with time or, simply, the radial frequency is the time derivative of the total phase Φ_{tot}:

$$\omega_{inst}(t) \equiv \frac{d}{dt}\left[\Phi_{tot}(t)\right] = \omega_0 + 2bt\,. \quad \text{(III.6)}$$

We can see that the radial frequency ω_{inst} is a linear function of time, which means that the frequency is changing during the pulse duration: it is increasing (decreasing) with time when b is positive (negative), which corresponds to a *positive* (*negative) chirp*.

[**] We assume usually $\Phi_{tot}(0) = 0$ i.e. our phase measurements are relatives.

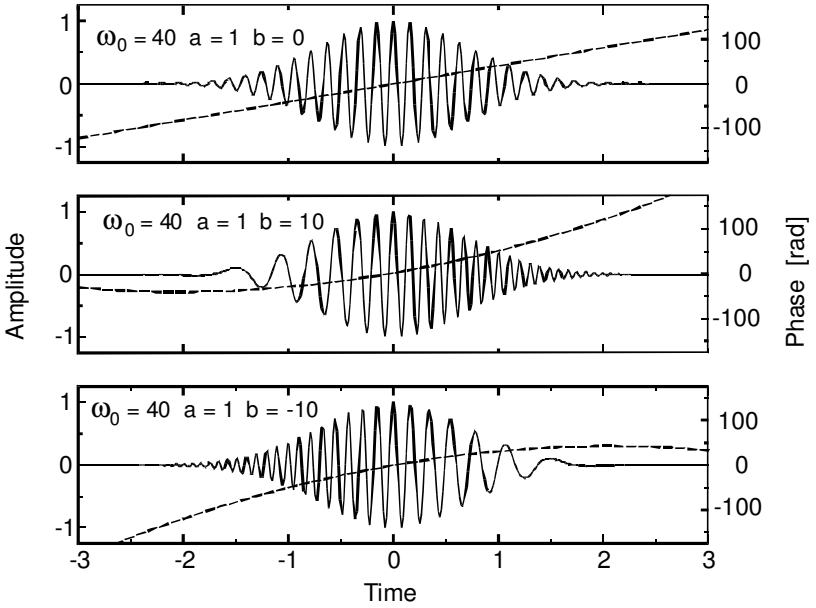

Figure III-2: Upper panel: Example of unchirped (*b = 0*) Gaussian pulse. Center panel: Example of positive (*b = 10*) chirped Gaussian pulse. Lower panel: negative (*b = -10*) chirped Gaussian pulse. The dashed curves correspond to the time evolution of the optical phases.

GAUSSIAN PULSE SPECTRUM

Using Fourier transform, we can get the frequency spectrum of the complex Gaussian pulse:

$$\tilde{E}(t) = \tilde{E}_0 \exp(-\gamma t^2 + j\omega_0 t) \underset{FT^{-1}}{\overset{FT}{\rightleftharpoons}} \tilde{E}(\omega) = \sqrt{\frac{\pi}{\gamma}} \tilde{E}_0 \exp\left[-\frac{(\omega-\omega_0)^2}{4\gamma}\right]. \quad \text{(III.7)}$$

In this case, the Gaussian temporal function is transformed into a Gaussian spectral function, which is another advantage of using a Gaussian shape. Taking the square modulus of the pulse spectrum (III.7) yields the power spectral density $\left|\tilde{E}(\omega)\right|^2$:

$$\frac{\pi}{|\gamma|}\left|\tilde{E}_0\right|^2 \exp\left[-\frac{a}{a^2+b^2}\frac{(\omega-\omega_0)^2}{2}\right] = \frac{\pi}{|\gamma|}\left|\tilde{E}_0\right|^2 \exp\left[-4\ln 2\frac{(\omega-\omega_0)^2}{\Delta\omega_p}\right], \quad \text{(III.8)}$$

where $\Delta\omega_p$ is the pulse bandwidth (FWHM).

We can convert this into a pulse bandwidth Δf_p measured in *Hz* by writing

$$\Delta f_p \equiv \frac{\Delta\omega_p}{2\pi} = \frac{\sqrt{2\ln 2}}{\pi}\sqrt{a\left[1+(b/a)^2\right]} = \frac{2\ln 2}{\pi\ \tau_p}\sqrt{1+(b/a)^2} \qquad \text{(III.9)}$$

It results that the bandwidth Δf_p of a complex Gaussian pulse is inversely proportional to its pulsewidth τ_p by a factor depending on the parameters *a, b.*

TIME–BANDWIDTH PRODUCT AND FOURIER-TRANSFORM-LIMITED PULSE

By rearranging equation (III.9) we can see that the product between pulsewidth and bandwidth for a complex Gaussian pulse will give

$$\Delta f_p\,\tau_p = \frac{2\ln 2}{\pi}\sqrt{1+(b/a)^2} \simeq 0.44\sqrt{1+(b/a)^2}\,. \qquad \text{(III.10)}$$

This law is called a *time–bandwidth product* law, which is readily applicable to other pulse shapes with different constants. The right hand side of equation (III.10) is constant for a given complex Gaussian pulse and it reaches its lowest value for unchirped pulses i.e. $\Delta f_p\ \tau_p \sim 0.44$. As a rule of thumb, if the optical pulse possesses a time–bandwidth product close to 0.5, the pulse is called *Fourier-transform limited*.

Active mode locking

As we mentioned in the previous chapter, there is a set of axial modes that can oscillate in the laser cavity, which are called longitudinal modes. These modes have a constant frequency spacing given by

$$\Delta\omega = 2\pi\frac{c}{2L}. \qquad \text{(III.11)}$$

Therefore, we can say that the frequency domain of the laser output is well structured. However, this is not the case for the time domain because each mode in the time domain is a sinusoidal function with determined frequency and free phase, which means that the phase is generally different from one mode to another and that there is no relation between them. As a result, the output of the laser will exhibit a random behavior, called free-running regime as shown in Figure III-3.

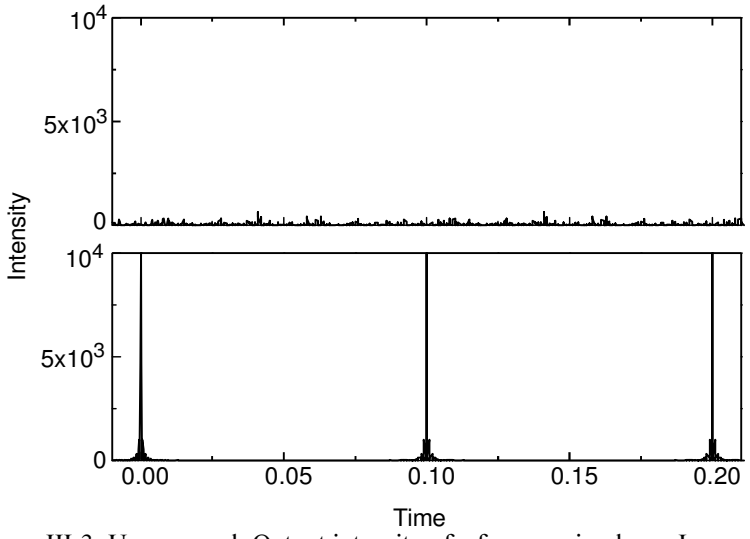

Figure III-3: Upper panel: Output intensity of a free-running laser. Lower panel: Output of a mode-locked laser. Example calculated for 100 modes and a frequency spacing of 10 Hz.

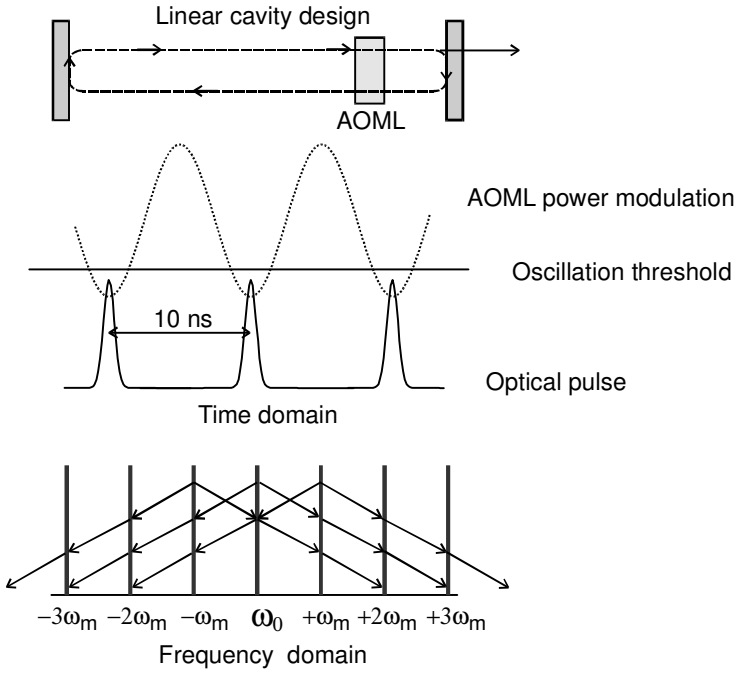

Figure III-4: Active mode locking by inserting an AOML in a linear cavity, and description of the output power in the time and the frequency domains.

To transpose into the time domain the spectral organization existing already in the frequency domain, the phases of the oscillating longitudinal modes should be related to each other. This is achieved in practice, by inserting a loss modulator at a fixed position inside the laser cavity as schematized in Figure III-4. This device shall modulate the loss at a frequency ω_{AM} matching the frequency spacing $\Delta\omega$ (100 MHz) of the longitudinal modes. Matching the modulation frequency and the frequency spacing will allow the longitudinal modes to interfere constructively. The resulting output intensity will display a huge peak for each round trip time as shown in the lower panel of Figure III-3.

Because it is based upon an acousto-optic interaction, the loss modulator is called an *acousto-optic mode locker* (AOML). Furthermore, the technique used is designated as *active mode locking* because the AOML is connected to an external source, which is an electronic RF power supply operating at a frequency of 50 MHz. Figure III-5 shows a schematic view of such an AOML device which in our case consists of a quartz crystal with a front face area of 1 cm^2 and a length of 62 mm. The excitation of vertical stationary ultrasonic waves inside the crystal creates variations of the refractive index that follow the intensity of the waves. In other words, the periodic variation will create a diffraction grating with spatial period equal to half the ultrasonic wavelength. This grating appears and disappears at twice the frequency of the applied RF signal. Finally, the whole process will result in an electro-optical switch working at a frequency of 100 MHz and consequently, the cavity length should be about 1.5 m.[††]

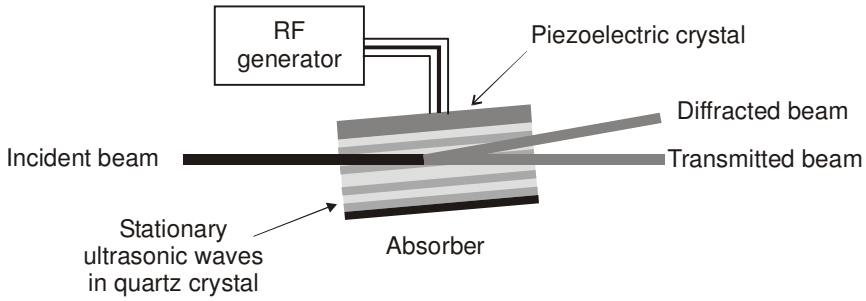

Figure III-5: Schematic view of an acousto-optic mode locker (AOML)

[††] This apparent length could be shorter due to the refractive indices of the elements present inside the cavity.

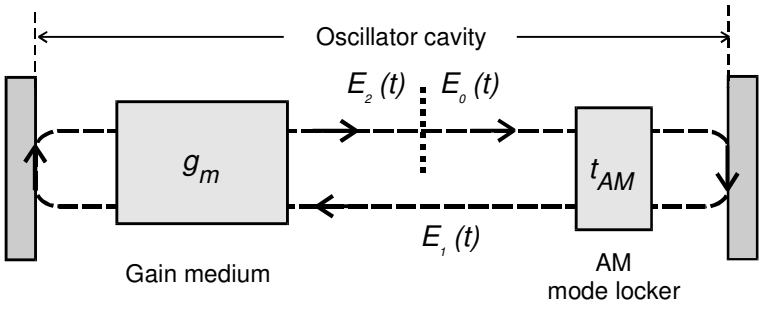

Figure III-6: Pulse round-trip inside the actively modelocked laser cavity

After being created by the active mode locking, the pulse will become shorter each time it passes through the AOML. In the spectral domain, this mechanism corresponds to spectral broadening of the oscillating pulse. This spectral broadening will continue until it becomes relatively comparable to the laser linewidth when the amplifying medium will provide less gain. Thus, the balance between pulse shortening by AOML and gain narrowing will determine the pulse duration.[17]

Analysis of circulating Gaussian pulse in an actively mode-locked oscillator

In this section, we shall try to derive an analytical expression that represents the steady state pulse duration inside a cavity containing a gain medium and an AOML for active mode locking as drawn in Figure III-6. Let us first look at the influence of the gain medium on a Gaussian optical pulse after round-trip propagation in the cavity. The latter process can be represented by the convolution between the spectrum of the optical pulse $\tilde{E}_0(t)$ and the round-trip gain $\tilde{g}(t)$, then in the frequency domain we have:.

$$\tilde{E}_2(\omega) = \tilde{g}(\omega)\tilde{E}_1(\omega), \tag{III.12}$$

where $\tilde{E}_2(\omega)$ is the spectrum of the transmitted pulse after one round trip. The round-trip amplitude gain $\tilde{g}(\omega)$ is given by

$$\tilde{g}(\omega) = \exp\left[\frac{g_m}{1+2j(\omega-\omega_a)/\Delta\omega_a} - j\frac{2\omega L}{c}\right], \tag{III.13}$$

where g_m is the peak round-trip gain coefficient and $2\omega L/c$ the round-trip phase shift in the empty cavity. In the case of active mode locking, it is interesting to approximate equation (III.13) by taking into account the fact that the pulse spectrum will in practice remain smaller than the bandwidth $\Delta\omega_a$ of the gain medium. Mathematically, the condition $(\omega - \omega_a)/\Delta\omega_a < 1$ leads to the following approximation

$$\tilde{g}(\omega) \simeq \exp\left\{ g_m \left[1 - 4\left(\frac{\omega - \omega_a}{\Delta\omega_a} \right)^2 \right] - 2j \left(\frac{\omega L}{c} + g_m \frac{\omega - \omega_a}{\Delta\omega_a} \right) \right\}. \quad \text{(III.14)}$$

The linear part in ω of the round-trip phase is given by:

$$\frac{2\omega L}{c}\left(1 + \frac{g_m}{\Delta\omega_a}\frac{c}{L} \right) = \frac{2\omega L}{c}\left(1 + \frac{g_m}{\Delta\omega_a}\frac{\Delta\omega}{\pi} \right). \quad \text{(III.15)}$$

It is clear that an additional phase shift appears due to the presence of the gain medium. This term will change the effective frequency spacing between the longitudinal modes by the ratio

$$\frac{\Delta\omega - \Delta\omega'}{\Delta\omega} \simeq \frac{\Delta\omega}{\Delta\omega_a}\frac{g_m}{\pi}. \quad \text{(III.16)}$$

As an example, in a Nd:YAG laser cavity, there may be about 1,000 longitudinal modes that can oscillate, and the peak round-trip gain factor under normal operating conditions may have a value $g_m \sim 0.2$. The ratio is of the order of 1 in 10,000 meaning that the frequency is shifted by about 13 kHz out of a modulation frequency of ~100 MHz. This leads us to discard this effect in our analysis and keep the following approximation for $\tilde{g}(\omega)$:

$$\tilde{g}(\omega) \simeq \exp\left[-4 g_m \left(\frac{\omega - \omega_a}{\Delta\omega_a} \right)^2 \right]. \quad \text{(III.17)}$$

PULSE PROPAGATION THROUGH THE LASER GAIN MEDIUM

Including the previous approximation of the gain spectrum $\tilde{g}(\omega)$ in equation (III.12) will yield for the transmitted pulse:

$$\exp\left[-\frac{(\omega - \omega_a)^2}{4\gamma_0} \right] \cdot \exp\left[-\frac{4 g_m}{\Delta\omega_a{}^2} (\omega - \omega_a)^2 \right] = \exp\left[-\frac{(\omega - \omega_a)^2}{4\gamma_1} \right] \cdot \quad \text{(III.18)}$$

This shows that the Gaussian pulse will keep its shape after passing trough the gain medium but with a new Gaussian parameter γ_1 given by:

$$\frac{1}{\gamma_2} = \frac{1}{\gamma_1} + \frac{16\, g_m}{\Delta\omega_a^2}, \qquad \text{(III.19)}$$

assuming that $\omega_0 = \omega_a$, which means that the pulse spectrum is centered on the atomic gain profile. In order to clarify this, let us assume that the incident pulse is unchirped and by consequence the transmitted pulse will also have no chirp $b_2 = b_1 = 0$. In addition, the broadening ratio of the resulting pulse ($PBR = \tau_{out}/\tau_{in}$) is given by the expression

$$PBR = \sqrt{1 + \frac{32\ln 2}{\pi^2}\frac{g_m}{PFTR^2}}, \qquad \text{(III.20)}$$

where $PFTR$ is the ratio of incident pulsewidth to the gain Fourier-transform-limited pulsewidth as defined by the equation

$$PFTR = \frac{\tau_{in}}{\tau_{FT}} \quad \text{with} \quad \tau_{FT} \simeq \frac{0.5}{\Delta f_a}. \qquad \text{(III.21)}$$

The function (III.20) is plotted in Figure III-7. It results, for unchirped pulses, that the closer the pulsewidth is to τ_{FT} the higher is the PBR.

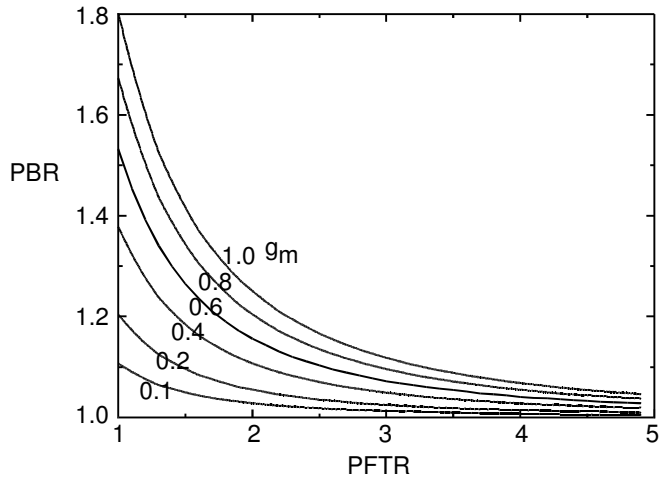

Figure III-7: Plot of the pulse–broadening ratio (PBR) versus the ratio of incident pulsewidth to the gain Fourier-transform-limited pulsewidth (PFTR). The different curves correspond to different gain values.

This fact shows that *the broadening effect of the gain medium prevents the pulsewidth to reach its minimum that is the gain Fourier-transform-limited pulse* τ_{FT}. In the case of Nd:YAG laser, τ_{FT} is about *4* ps.

PULSE PROPAGATION THROUGH AN AOML

As a second step we shall look at the effect of the AOML on the Gaussian optical pulse taking into account that the amplitude transmission function for AOML is given by

$$\tilde{t}_{AM}(t) = \exp\left\{-\delta_{AM}\left[1-\cos(\omega_{AM}t)\right]\right\}, \qquad \text{(III.22)}$$

where ω_{AM} is the loss modulation frequency and $2\delta_{AM}$ the modulation depth parameter, as shown in Figure III-8. Thus the transmitted pulse $\tilde{E}_2(t)$ is given by

$$\tilde{E}_1(t) = \tilde{t}_{AM}(t)\,\tilde{E}_0(t). \qquad \text{(III.23)}$$

As we can expect, the transmitted pulse is centered at the maximum of the transmission function $\tilde{t}_{AM}(t)$. In addition, we can say that the pulsewidth is shorter than the modulation period of the AOML, for example, the period of the used AOML is about 10 ns in comparison to the active mode-locked pulse of about 100 ps. Using the latter fact, we can make the following approximation:

$$\tilde{t}_{AM}(t) = \exp\left(-\frac{\delta_{AM}\omega_{AM}^2}{2}t^2\right), \quad |t| \ll T_{AM}. \qquad \text{(III.24)}$$

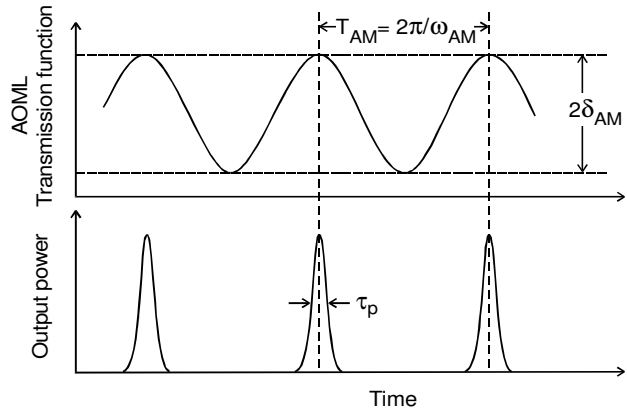

Figure III-8: Pulse transmission through an acousto-optic mode locker (AOML).

Applying this approximation to Equation (III.23) yields

$$\exp\left(-\gamma_1 t^2\right)\exp\left(-\frac{\delta_{AM}\omega_{AM}^2}{2}t^2\right)=\exp\left[-\gamma_2 t^2\right]. \qquad \text{(III.25)}$$

From the latter equation, we can get the Gaussian pulse parameter γ_2 of the transmitted pulse as follows

$$\gamma_2-\gamma_1\simeq\frac{\delta_{AM}\omega_{AM}^2}{2}. \qquad \text{(III.26)}$$

In the absence of chirp, the pulse shortening ratio $PSR = \tau_2/\tau_1$ is given by

$$PSR=\left(1+\frac{\pi^2}{\ln 2}\delta_{AM}PMPR^2\right)^{-1}, \qquad \text{(III.27)}$$

where $PMPR = \tau_1/T_{AM}$ is the ratio of the incident pulsewidth to the modulation period T_{AM}. The behavior of the function is plotted in Figure III-9: the higher the modulation depth δ_{AM}, the shorter the pulsewidth; moreover, no shortening effect is observed for PMPR smaller than 0.01. This indicate that the temporal pulse profile is no longer confined by the temporal variation of the AOML transmission function for pulse durations less than one hundredth of the modulation period T_{AM}.

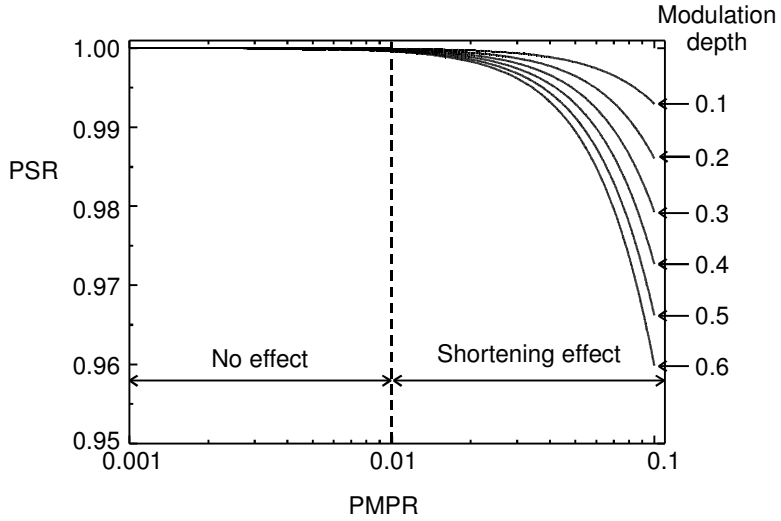

Figure III-9: Pulse shortening ratio (PSR) as a function of the PMPR.

STEADY-STATE SOLUTIONS FOR ACTIVE MODE LOCKING

After discussing briefly the effect of the presence of the gain medium and the AOML inside the cavity, we can find the total variation of the complex Gaussian parameter $\gamma_2 - \gamma_0$ for one complete round trip as follows

$$\gamma_2 - \gamma_0 = (\gamma_2 - \gamma_1) + (\gamma_1 - \gamma_0) \simeq \frac{\delta_{AM}\omega_{AM}^2}{2} - \frac{16\, g_m}{\Delta\omega_a^2}\gamma_0^{\,2}, \quad \text{(III.28)}$$

where we used the following approximation for equation (III.19)

$$\gamma_1 - \gamma_0 = -\frac{16\, g_m}{\Delta\omega_a^2}\gamma_0^{\,2}. \quad \text{(III.29)}$$

The steady-state condition implies that the oscillatory electric field should repeat itself without any distortion, which yields:

$$\tilde{E}_2(t) \equiv \tilde{E}_0(t) \;\Rightarrow\; \gamma_2 = \gamma_0 = \gamma_{\rm ss} \quad \text{in the steady-state}. \quad \text{(III.30)}$$

In other words, this represents the stable pulse duration that is determined by the competition between pulse shortening by AOML and pulse broadening by the gain medium. As we can see from (III.28), the resulting pulse is Gaussian which implies that the steady-state (*ss*) pulse is also Gaussian with parameter γ_{ss} (III.30); therefore, equation (III.28) becomes

$$\frac{\delta_{AM}\omega_{AM}^2}{2} - \frac{16\, g_m}{\Delta\omega_a^2}\gamma_{ss}^{\,2} = 0 \;\Rightarrow\; \gamma_{ss} = \sqrt{\frac{\delta_{AM}}{g_m}}\,\frac{\omega_{AM}\Delta\omega_a}{4\sqrt{2}}. \quad \text{(III.31)}$$

One can see that there is no chirp in this process, i.e. β_{ss}= 0 and it follows that

$$\tau_{ss} \simeq \sqrt{\frac{2^{3/2}\ln 2}{\pi^2}}\left(\frac{g_m}{\delta_{AM}}\right)^{1/4}\frac{1}{\sqrt{f_{AM}\Delta f_a}}. \quad \text{(III.32)}$$

where τ_{ss} designates the steady state pulse duration in actively modelocked oscillator when the gain medium is homogeneously broadened. It results from equation (III.32) that the pulsewidth increases slightly with the saturation gain coefficient g_m and decreases with the modulation depth δ_{AM}, which is proportional to the applied RF power:

$$\delta_{AM} \propto P_{AM} \quad \text{(III.33)}$$

In other words, the mode-locked pulsewidth will thus decrease with increasing modulation power as $P_{AM}^{\,1/4}$.

Finally, as both coefficients g_m and δ_{AM} have approximately the same value, the steady-state pulsewidth can be given by the approximate expression

$$\tau_{ss} \cong \frac{0.45}{\sqrt{f_{AM}\Delta f_a}}. \qquad \text{(III.34)}$$

In the case of Nd:YAG, where Δf_a = 120 GHz and the modulation frequency f_{AM} is 100 MHz, (III.34) gives τ_{ss} ~ 130 ps. This is in keeping with our experimental observations; moreover, (III.34) shows that gain FT limited pulses are very difficult to be generated by this technique of mode locking especially for pulsed laser (transient regime), which we will analyze in the next section.

Transient active mode locking

In flashlamp-pumped lasers, the number of round trips inside the cavity is readily limited by the applied electrical pulsewidth, which is about 160 μs. In this case, the steady-state condition is very difficult to reach. The work of Kuizenga,[18,19] about active mode locking, has shown that the transient pulsewidth after M round trip can be given by

$$\tau_{tr} = \frac{\tau_{ss}}{\sqrt{\tanh(M/M_0)}}, \qquad \text{(III.35)}$$

where M_0 is the number of round trips for which the pulsewidth τ_{tr} is equal to $1.15\tau_{ss}$. M_0 is given by

$$M_0 = \frac{1}{\sqrt{8g_m}} \frac{\Delta\omega_a}{\delta_{AM}\,\omega_{AM}}. \qquad \text{(III.36)}$$

It results that M_0 decreases with increasing modulation depth δ_{AM} and in turn with the modulation power. The plot of Equation (III.35), in Figure III-10, shows that the transient pulsewidth τ_{tr} practically reaches the steady-state value τ_{ss} after M_{ss} = 1.52M_0 round trips inside the laser cavity. It yields

$$M_{ss} = \frac{0.54\Delta\omega_a}{\sqrt{g_m}\delta_{AM}\omega_{AM}}. \qquad \text{(III.37)}$$

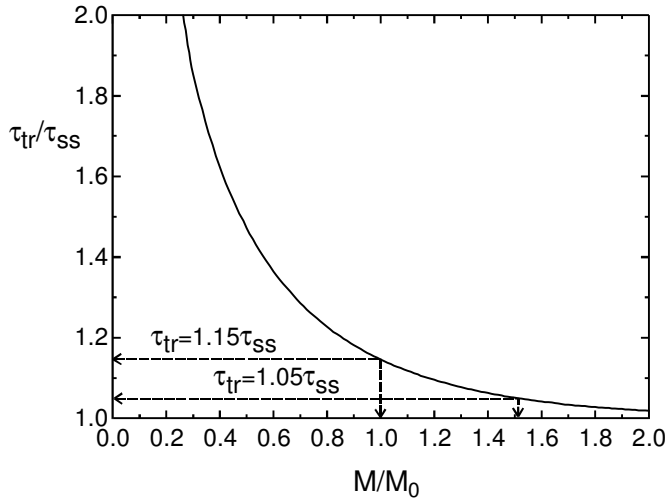

Figure III-10: Transient behavior of actively mode-locked pulse. The steady-state τ_{ss} pulsewidth is practically reached for M round trips larger than 1.52 M_0.

In our flashlamp-pumped Nd YAG laser, we can obtain M_{ss} = 1833 round trips for the following parameters: $\Delta f_a = \Delta\omega_a/2\pi$ = 120 GHz, g_m = 0.5, δ_{AM} = 0.5 and f_{AM} = 100 MHz; therefore, a minimum of 1833×10^{-8} =18.3 μs are required for the pulses to reach steady-state pulsewidth within 5%. In addition, the relaxation oscillations (or natural Q-switch) will limit the laser output to pulse trains with durations in the range of 100 - 300 ns. The latter fact makes the main argument to look for a more efficient method, which will be the passive mode locking.

Passive mode locking

Unlike the technique of active mode locking, the passive mode locking depends generally on the intensity-dependent behavior of the used materials. Within this field, we can distinguish two major classes: *passive, positive* and *passive, negative* mode locking.

PASSIVE, POSITIVE MODE LOCKING

In the passive mode locking, the gain inside the oscillator increases with increasing intracavity intensity. This mechanism is very attractive to obtain short optical pulses thanks to the dependence of the device response on the pulse intensity profile, which makes the intracavity pulse shorter and

shorter until it becomes limited by the gain Fourier-transform pulsewidth. In a general way, one can divide the passive mode locking into two categories as follows:

- First, the passive mode locking device for continuous wave (CW) mode locked oscillators. The steady-state pulsewidth can be achieved easily because of the very large number of round trips effectuated inside the oscillator. We present in Table III-1 the most cited methods for CW.

- The second category contains the devices for pulsed wave (PW) mode locking. In these devices, the transient behavior is the dominant regime and the achievement of the steady-state condition is a challenge. The most used technique for mode locking Nd:YAG oscillator is the dye saturable absorber cell (DSAC or FSA). In this work, we show that FDNLM presents comparable performances with DSAC for modelocking a PW Nd:YAG oscillator.

From Table III-1, one can notice that the passive methods for PW can be used for the CW but not vice versa. In our opinion, this is due to the fact that the passive PW devices support higher intensity than CW devices. Figure III-11 shows the schematic arrangement of the optical elements inside the resonator for both DSAC and FDNLM passive methods.

Passive mode-locking method	Abbreviation	Operation
Frequency-doubling nonlinear mirror	FDNLM	CW, PW
Dye saturable absorber cell or Fast saturable absorber	DSAC or FSA	CW, PW
Adding pulse mode locking	APM	CW
Semiconductor saturable absorber mirror	SeSAM	CW
Soliton mode locking		CW
Saturable Bragg reflector	SBA	CW
Colliding pulse mode locking	CPM	CW
Kerr lens mode locking	KLM	CW

Table III-1: List of passive mode-locking methods and their operation domains.

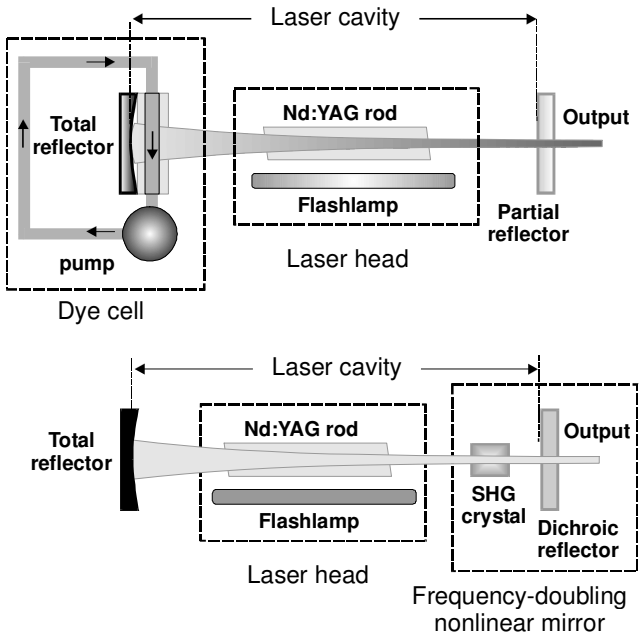

Figure III-11: Passive mode locking of a pulsed laser by a dye saturable absorber cell (upper panel) and by a frequency-doubling nonlinear mirror (lower panel).

PASSIVE, NEGATIVE MODE LOCKING

In this case, the gain inside the laser cavity decreases with increasing intracavity intensity. This mechanism permits from one hand to protect the optical elements of the laser from the over intensity and, on the other hand, it can stabilize the intracavity intensity at constant level. The previous phenomenon is responsible for generating long pulse trains by retaining the energy stored in the laser rod as long as possible, that means the best situation to overcome the natural Q-switch effect.

In our setup, we used the two-photon absorption (TPA) process in GaAs platelet. In normal condition, GaAs shows no absorption at 1.064 μm wavelength unless the intensity exceeds the TPA threshold, which is about 55 MW/cm^2. Therefore, the intracavity intensity will be limited at the level that permits the optical pulse to perform as large a number of round trips as possible, which is the key factor for approaching the steady-state regime.

Hybrid mode locking

Hybrid mode locking indicates the use of both active and passive mode locking, and provides a stable shot-to-shot operation thanks to the pulse initiation inside the laser cavity by the AOML.

Conclusion

We can conclude that the generation of short optical pulses calls for mode-locking techniques, which permit the use of the total bandwidth of the laser gain medium. In the case of the Nd:YAG laser, active mode locking by AOML can generate pulses as short as 130 ps, whereas passive mode locking gives pulse durations about 4 ps for continuous-wave laser. The latter pulse durations are a challenge for pulsed lasers (transient regime) due to the limited number of round trips inside the oscillator.

The two techniques of passive mode locking used for pulsed Nd:YAG laser operation are day saturable absorber cell (DSAC) and frequency-doubling nonlinear mirror (FDNLM). In the literature, the FDNLM technique has a lower pulse duration performance in comparison with DSAC; however, we shall show in chapter V that it is possible to improve considerably the performances of FDNLM and to reach those of the DSAC technique.

In order to model correctly the FDNLM, we need first to solve Maxwell's equations in a nonlinear medium. This will be done in detail in the next chapter, in the case of second-order processes and within the slowly varying envelope approximation (SVEA).

Chapter IV Wave Propagation in Linear and Nonlinear Media

In this section, we shall try to derive the wave propagation equation from Maxwell's and material equations for a nonlinear medium.[20] Maxwell's* equations (IV.1) describe the coupling between the electric and the magnetic fields for dynamic charges (time varying current).

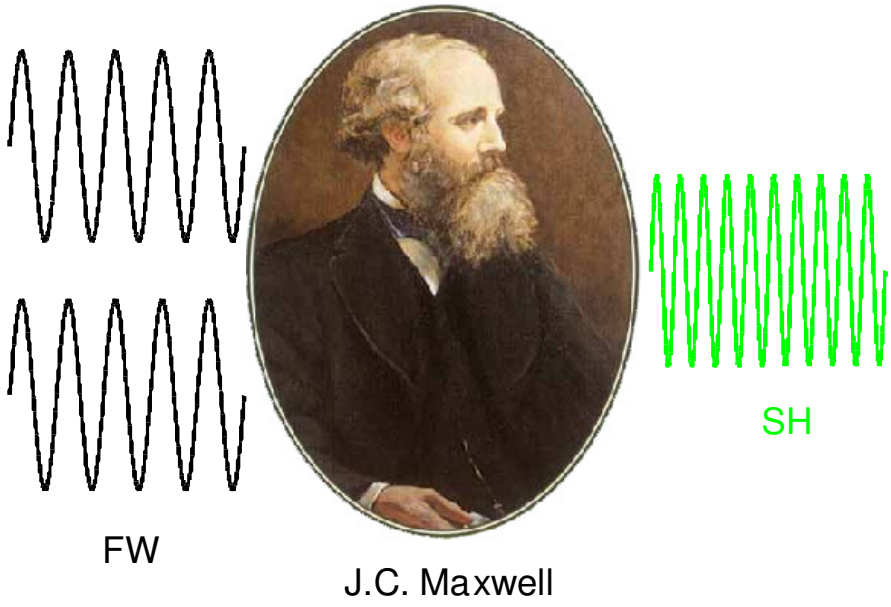

* MAXWELL, James Clerk, 1831-1879, Scottish mathematician and physicist.

The first couple of equations (IV.1) shows that an electric field $\vec{E}(\vec{r},t)$ can be generated in the presence of electric charge density $\rho(\vec{r},t)$ or a varying magnetic induction field $\vec{B}(\vec{r},t)$ through a closed circuit. The latter phenomena are known as Gauss* theorem and as Faraday's† law, respectively; the sign of the right hand member of Faraday's law results from Lenz‡ law. The third equation in (IV.1) describes the fact that no free magnetic charges can be found in nature. In the last equation, a magnetic field $\vec{H}(\vec{r},t)$ can be generated in the presence of a current density flux $\vec{J}(\vec{r},t)$, which is Ampere's§ law, or when the displacement electric field $\vec{D}(\vec{r},t)$ varies with time giving a displacement current $\partial\vec{D}/\partial t$. This last term has been introduced by Maxwell himself.

$$\begin{aligned}
&\vec{\nabla}\cdot\vec{D}(\vec{r},t)=\rho(\vec{r},t)\\
&\vec{\nabla}\times\vec{E}(\vec{r},t)=-\frac{\partial}{\partial t}\vec{B}(\vec{r},t)\\
&\vec{\nabla}\cdot\vec{B}(\vec{r},t)=0\\
&\vec{\nabla}\times\vec{H}(\vec{r},t)=\vec{J}(\vec{r},t)+\frac{\partial}{\partial t}\vec{D}(\vec{r},t)
\end{aligned} \qquad \text{(IV.1)}$$

However, these expressions are not sufficient to completely describe electromagnetic wave propagation through a medium. In the medium, the induction fields (D, B) are related to the fields (E, H) by the material equations (IV.2). The third equation of (IV.2) describes Ohm's** law.

$$\begin{aligned}
&\vec{D}(\vec{r},t)=\varepsilon_0\vec{E}(\vec{r},t)+\vec{P}(\vec{r},t)\\
&\vec{B}(\vec{r},t)=\mu_0\vec{H}(\vec{r},t)+\vec{M}(\vec{r},t)\\
&\vec{J}(\vec{r},t)=\vec{\sigma}\cdot\vec{E}(\vec{r},t)
\end{aligned} \qquad \text{(IV.2)}$$

In these equations, the parameters ε_0 and μ_0 are the electric permittivity and the magnetic permeability of the vacuum. The vectors $\vec{P}(\vec{r},t)$ and $\vec{M}(\vec{r},t)$ are the material polarization under applied electric field and the material magnetization under applied magnetic field. It is obvious that these

---

* GAUSS, Karl Friedrich, 1777-1855, German mathematician.

† FARADAY, Michael, 1791-1867, English physicist.

‡ LENZ, Heinrich Friedrich Emil, 1804-1865, Russian German physicist.

§ AMPERE, Andre Marie, 1775-1836, French mathematician and physicist.

** OHM, Georg Simon, 1787-1854, German physicist.

vectors vanish in the vacuum. The tensor of the electrical conductivity is represented by $\ddot{\sigma} \equiv \sigma_{ij}$. Both sets of equations (IV.1) and (IV.2) give a constitutive first order-differential equation system that can be solved from point to point starting with initial conditions. From the mathematical point of view, one can say that the four fields propagate, which is not completely right from the physical point of view because no propagation can take place without velocity. Let us clarify this idea by elimination of the field $\vec{H}$ from Maxwell's equations (IV.1) using (IV.2), which yields

$$\vec{\nabla}\times\vec{\nabla}\times\vec{E}(\vec{r},t) = -\mu_0\ddot{\sigma}\cdot\frac{\partial}{\partial t}\vec{E}(\vec{r},t) - \mu_0\left[\varepsilon_0\frac{\partial^2}{\partial t^2}\vec{E}(\vec{r},t) + \frac{\partial^2}{\partial t^2}\vec{P}(\vec{r},t)\right]. \qquad \text{(IV.3)}$$

By rearranging the latter equation and supposing that no ohmic loss and no free charges are present in the homogenous dielectric medium (i.e., $\ddot{\sigma} \cong 0$ and $\vec{\nabla}\cdot\vec{E} = 0$), one obtains the wave equation of the electromagnetic field (EM):

$$\nabla^2\vec{E}(\vec{r},t) - \mu_0\varepsilon_0\frac{\partial^2}{\partial t^2}\vec{E}(\vec{r},t) = \mu_0\frac{\partial^2}{\partial t^2}\vec{P}(\vec{r},t). \qquad \text{(IV.4)}$$

The last equation shows that the electric field propagates with velocity equal to $c = (\varepsilon_0\mu_0)^{-1/2}$ in the vacuum (i.e., $\vec{P} = \vec{0}$) and this velocity is slower in the presence of the polarization of the dielectric medium. Transforming this equation into the frequency domain using the Fourier* spectra $\vec{E}(\vec{r},\omega)$ and $\vec{P}(\vec{r},\omega)$, we obtain:

$$\left[\nabla^2 - \varepsilon_0\mu_0\omega^2\right]\vec{E}(\vec{r},\omega) = \mu_0\omega^2\vec{P}(\vec{r},\omega). \qquad \text{(IV.5)}$$

The polarization spectrum can be divided into linear and nonlinear parts with respect to the electric field inside the matter $\vec{E}(\vec{r},\omega)$:

$$\vec{P}(\vec{r},\omega) = \vec{P}_L(\vec{r},\omega) + \vec{P}_{NL}(\vec{r},\omega). \qquad \text{(IV.6)}$$

In the last expression, the nonlinear polarization contains all polarization orders higher than the first one

$$\vec{P}_{NL}(\vec{r},\omega) = \sum_{n\geq 2}\vec{P}^{(n)}(\vec{r},\omega). \qquad \text{(IV.7)}$$

The linear polarization is proportional to the electric field by a factor $\chi(\omega)$

$$\vec{P}_L(\vec{r},\omega) = \varepsilon_0 \ddot{\chi}(\omega) \cdot \vec{E}(\vec{r},\omega). \tag{IV.8}$$

In the general case, the susceptibility of a dielectric medium is a tensor of second rank $\ddot{\chi} \equiv \chi_{ij}$. Using this latter definition one can extend the permittivity in the vacuum to the permittivity in the matter:

$$\ddot{\varepsilon}(\omega) = \varepsilon_0 \left[\ddot{I} + \ddot{\chi}(\omega) \right], \tag{IV.9}$$

where $\ddot{I}$ is the unity matrix. Substituting (IV.6) and (IV.9) into (IV.5) yields:

$$\left[\nabla^2 - \mu_0 \omega^2 \ddot{\varepsilon} \cdot \right] \vec{E}(\vec{r},\omega) = \mu_0 \omega^2 \vec{P}_{NL}(\vec{r},\omega). \tag{IV.10}$$

Considering a monochromatic wave at frequency ω_0, we obtain for complex phasors[†] the equation:

$$\left[\nabla^2 - \mu_0 {\omega_0}^2 \ddot{\varepsilon} \cdot \right] \hat{E}(\vec{r},\omega_0) = \mu_0 {\omega_0}^2 \hat{P}_{NL}(\vec{r},\omega_0). \tag{IV.11}$$

Coupled-wave equations in nonlinear medium

In order to simplify equation (IV.10) we take the following physical assumptions:

- We consider an EM plane wave, monochromatic and linearly polarized, propagating along the $\vec{e}_z$ direction (which is an arbitrary axis). In this case the complex phasor takes the following form

$$\hat{E}(z,\omega) = \vec{e}(\omega)\, \overline{E}(z,\omega)\, e^{-j(kz)}, \tag{IV.12}$$

  where $\overline{E}(z,\omega)$ and $\vec{e}(\omega)$ are the complex amplitude and the polarization direction of the electric field, respectively.
- In an isotropic medium: $\varepsilon_{ij} = \varepsilon \delta_{ij}$.
- The complex function $\overline{E}(z,\omega)$ is weakly dependent on *z*. This assumption is called *the slowly varying envelope approximation* (SVEA) and is given:

$$\left| \frac{\partial^2}{\partial z^2} \overline{E} \right| \ll \left| k \frac{\partial}{\partial z} \overline{E} \right|. \tag{IV.13}$$

---

[*] FOURIER, Jean Baptiste Joseph, 1768-1830, French mathematician.

[†] The complex phasor is related to the field vector by $\vec{E}(\vec{r},\omega_0) = \mathrm{Re}\left[\hat{E}(\vec{r},\omega_0) \right]$.

Thus, we get the SVEA differential equation:

$$\frac{\partial}{\partial z}\bar{E}(z,\omega) = -j\frac{\mu_0\omega^2}{2k}\hat{P}_{NL}(z,\omega)\cdot\vec{e}(\omega)\, e^{jkz}. \qquad \text{(IV.14)}$$

We restrict our study to only the second order term of the nonlinear polarization i.e. $\vec{P}_{NL} = \vec{P}^{(2)}$, resulting from the interaction between two monochromatic plane waves (see references [21,22])

$$\hat{P}_i^{(2)}(z,\omega) = C\varepsilon_0 \sum_{j,k} \chi_{ijk}(-\omega,\omega',\omega-\omega')\, \hat{E}_j(z,\omega')\hat{E}_k(z,\omega-\omega')$$
$$\text{with } C = \begin{cases} 1 \text{ for } \omega \neq 0, \omega \neq 2\omega' \\ \frac{1}{2} \text{ for } \omega = 0, \omega = 2\omega' \end{cases} \qquad \text{(IV.15)}$$

Substituting eq. (IV.15) into (IV.14) we obtain the coupled waves equation

$$\frac{\partial}{\partial z}\bar{E}(z,\omega) = -j\frac{\omega\,\chi_{eff}^{(2)}(-\omega,\omega',\omega-\omega')}{2c\; n(\omega)}\bar{E}(z,\omega')\bar{E}(z,\omega-\omega')\, e^{j[k(\omega)-k(\omega')-k(\omega-\omega')]z} \qquad \text{(IV.16)}$$

where the effective second-order susceptibility $\chi_{eff}^{(2)}$ is given by

$$\chi_{eff}^{(2)}(-\omega,\omega',\omega-\omega') = C\sum_{\mathrm{i,j,k}} \chi_{ijk}(-\omega,\omega',\omega-\omega')\, e_i(\omega)e_j(\omega')e_k(\omega-\omega') \qquad \text{(IV.17)}$$

Equation (IV.16) describes the linear coupling between three waves propagating into a nonlinear medium of the second order (i.e. $\chi_{eff}^{(2)} \neq 0$). The frequencies of the three interacting waves satisfy the *sum frequency rule*, i.e. one of these frequencies equals the sum of the others.

Energy in a nonlinear medium (Manley-Rowe relations)

In this section, we derive the Manley-Rowe relations from Maxwell's equations. We begin by calculating the work W done by an electric field on the free charges in the unit volume

$$\frac{dW}{dt} = \vec{J}(\vec{r},t)\cdot\vec{E}(\vec{r},t). \tag{IV.18}$$

Using the fourth equation of the set of (IV.1) and the vector identity

$$\vec{\nabla}\cdot(\vec{E}\times\vec{H}) = \vec{H}\cdot(\vec{\nabla}\times\vec{E}) - \vec{E}\cdot(\vec{\nabla}\times\vec{H}) \tag{IV.19}$$

and finally substituting $\vec{\nabla}\times\vec{E}$ by the second Maxwell's equation, we obtain

$$\vec{J}\cdot\vec{E} = -\vec{\nabla}\cdot\left(\vec{E}\times\vec{H}\right) - \left[\vec{E}\cdot\frac{\partial\vec{D}}{\partial t} + \vec{H}\cdot\frac{\partial\vec{B}}{\partial t}\right]. \tag{IV.20}$$

Replacing the fields $\vec{D}$ and $\vec{B}$ by their expression as a function of $\vec{E}$ and $\vec{H}$ yields

$$\vec{J}\cdot\vec{E} = -\vec{\nabla}\cdot(\vec{E}\times\vec{H}) - \frac{1}{2}\frac{\partial}{\partial t}\left(\varepsilon_0\left|\vec{E}\right|^2 + \mu_0\left|\vec{H}\right|^2\right) - \vec{E}\cdot\frac{\partial\vec{P}}{\partial t} \tag{IV.21}$$

Placing the term containing the vector $\vec{S}_p = \vec{E}\times\vec{H}$, which is the Poynting* vector, in the left hand side of equation (IV.21) we have:

$$-\vec{\nabla}\cdot\vec{S}_p = \frac{1}{2}\frac{\partial}{\partial t}\left(\varepsilon_0\left|\vec{E}\right|^2 + \mu_0\left|\vec{H}\right|^2\right) + \vec{E}\cdot\frac{\partial\vec{P}}{\partial t} + \vec{J}\cdot\vec{E} \tag{IV.22}$$

We integrate the last equation over an arbitrary volume V and use the divergence theorem. The result is

$$-\oiint_S \vec{S}_p\cdot d\vec{S} = \frac{\partial}{\partial t}\left[\iiint_V\left(\frac{\varepsilon_0}{2}\left|\vec{E}\right|^2 + \frac{\mu_0}{2}\left|\vec{H}\right|^2\right)dV\right] + \iiint_V \vec{J}\cdot\vec{E}\,dV + \iiint_V \vec{E}\cdot\frac{\partial\vec{P}}{\partial t}dV. \tag{IV.23}$$

According to the conventional interpretation of the electromagnetic theory, the left hand side of (IV.23) gives the total power flowing into the

* POYNTING, John Henry, 1852-1914, English physicist.

volume bounded by the surface S. The first term on the right hand side is the rate of increase of the electromagnetic energy stored in the vacuum where

$$\mathrm{E}_{vac} = \int_V \left(\frac{\varepsilon_0}{2} \left|\vec{E}\right|^2 + \frac{\mu_0}{2} \left|\vec{H}\right|^2 \right) dV \,. \tag{IV.24}$$

The second term corresponds to the power lost by the field on the moving charges (ohmic loss). The third term $\vec{E} \cdot \partial \vec{P} / \partial t$ is of special interest because it represents the power per unit volume lost or gained by the field on the electric dipoles. The time-average dielectric losses or gains due to polarization are by definition

$$\langle \mathrm{P} \rangle = \left\langle \vec{E} \cdot \frac{\partial \vec{P}}{\partial t} \right\rangle_t \tag{IV.25}$$

For the derivation of the Manley-Rowe equations, we consider for simplicity only a process with second-order nonlinearity, with interacting waves at the frequencies $\omega_1, \omega_2, \omega_3$, for which $\omega_3 = \omega_1 + \omega_2$ holds. Then the polarizations are

$$\begin{aligned} \hat{P}_i(\omega_3) &= \varepsilon_0 \sum \chi_{ijk}(-\omega_3, \omega_1, \omega_2)\, \hat{E}_j(\omega_1) \hat{E}_k(\omega_2) \\ \hat{P}_i(\omega_1) &= \varepsilon_0 \sum \chi_{ijk}(-\omega_1, -\omega_2, \omega_3)\, \hat{E}_j^*(\omega_2) \hat{E}_k(\omega_3) \\ \hat{P}_i(\omega_2) &= \varepsilon_0 \sum \chi_{ijk}(-\omega_2, -\omega_1, \omega_3)\, \hat{E}_j^*(\omega_1) \hat{E}_k(\omega_3) \end{aligned} \tag{IV.26}$$

In a lossless nonlinear medium, the total average power vanishes for the three interacting waves, which yields

$$\langle \mathrm{P}(\omega_1) \rangle + \langle \mathrm{P}(\omega_2) \rangle + \langle \mathrm{P}(\omega_3) \rangle = 0 \,. \tag{IV.27}$$

Taking into account the properties of the second-order susceptibility, one can obtain the Manley-Rowe relations

$$\frac{\langle \mathrm{P}(\omega_1) \rangle}{\hbar \omega_1} = \frac{\langle \mathrm{P}(\omega_2) \rangle}{\hbar \omega_2} = -\frac{\langle \mathrm{P}(\omega_3) \rangle}{\hbar \omega_3} \,. \tag{IV.28}$$

These relations can be rewritten as $\Delta N_1 = \Delta N_2 = -\Delta N_3$ meaning that: *the number of photons generated (or annihilated) ΔN_3 in the nonlinear medium at frequency ω_3 equals the number of the coupled-photons pairs $\Delta N_{1,2}$ annihilated (or generated) at frequencies ω_1 and ω_2 per unit volume and per unit time*.

Description of the up- and down-conversion processes in a nonlinear medium (for degenerate frequencies)

The interaction between the fundamental (FW) and the second harmonic (SH) waves propagating through a nonlinear medium with $\chi_{eff}^{(2)} \neq 0$ can be described by the coupled-wave equations (IV.16).

- The propagating waves are plane waves under a continuous wave regime (CW). So the electric fields at frequencies ω and 2ω propagating along the z direction are given by

$$\begin{aligned} \vec{E}_{\omega}(z,t) &= \mathrm{Re}\left[\vec{e}_{\omega}\overline{E}_{\omega}(z)\, e^{j(\omega t - k_{\omega} z)} \right] \\ \vec{E}_{2\omega}(z,t) &= \mathrm{Re}\left[\vec{e}_{2\omega}\overline{E}_{2\omega}(z)\, e^{j(2\omega t - k_{2\omega} z)} \right], \end{aligned} \tag{IV.29}$$

  where ($\overline{E}_{\omega}$, $\vec{e}_{\omega}$) and ($\overline{E}_{2\omega}$, $\vec{e}_{2\omega}$) are the complex amplitude and the polarization unit vector for the FW and the SH electric fields.

- The slowly varying envelope approximation (SVEA).

- For collinear and type-I interactions in a nonlinear negative crystal. Consequently, the linear mismatch takes on the scalar form

$$\Delta k(\theta) = 2k_{\omega}^{o} - k_{2\omega}^{e}(\theta) = \frac{2\omega}{c}\left[n_{\omega}^{o} - n_{2\omega}^{e}(\theta) \right]. \tag{IV.30}$$

  In this case, the SH polarization is parallel to the extraordinary plane and its propagation vector makes an angle θ with the optical axis.

- For anisotropic crystals, the energy flow direction for the extraordinary wave may take an angle α with the z direction, which is called the *walk-off* angle. In the case of critical phase matching of type-I interaction, the FW and the SH waves make the following walk-off angles as shown on Figure IV-1:

$$\begin{aligned} \alpha_{\omega} &= 0 \\ \alpha_{2\omega} &= \mathrm{atan}\left\{ \frac{\left[(n_{2\omega}^{o})^2 - (n_{2\omega}^{e})^2 \right]\tan\theta}{(n_{2\omega}^{e})^2 + (n_{2\omega}^{o})^2 \tan^2\theta} \right\} \end{aligned} \tag{IV.31}$$

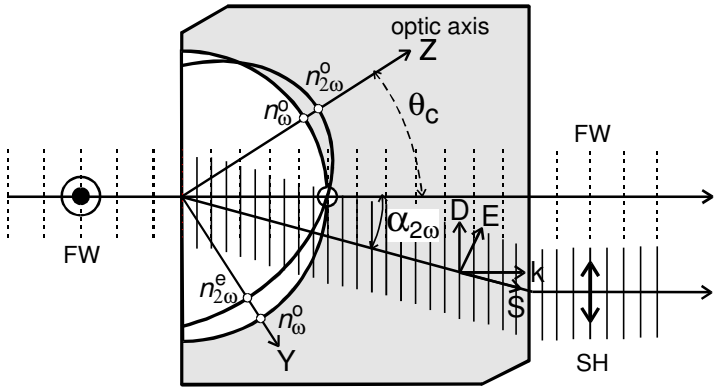

Figure IV-1: Critical type-I SH generation in BBO. The incident beam is normal to the surface with polarization normal to the principal plane. Inside the crystal the beam makes an angle θ_c with the optic axis. This corresponds to the intersection between the ellipse of the SH extraordinary index and the FW circle (ordinary index). The energy flow (Poynting vector S) of the SH field makes an angle $\alpha_{2\omega}$ with the wave propagation direction *k*.

- It is noteworthy that in the dielectric reference frame X, Y and Z, where Z is the optical axis, the assumption of a non-dispersive medium reduces the number of independent components of the quadratic susceptibility tensor χ_{ijk}, where $i,j,k \in \{X,Y,Z\}$, from 27 to 18 independent components. This permits the use of the plane representation $\chi_{i\ell}$, where $\ell \in \{XX,YY,ZZ,XY,XZ,YZ\}$. If we further apply the *Kleinman symmetry conditions*, which state that the χ components are independent of the frequency as well as of the permutation of indices, we are left with only 10 independent components.[23]

- The effective, nonlinear, second-order susceptibilities seen by the FW and the SH fields are $\vec{e}_{\omega} \cdot \vec{\vec{\chi}}^{(2)}(-\omega, 2\omega, -\omega) \cdot \vec{e}_{2\omega} \cdot \vec{e}_{\omega}$ and $\vec{e}_{2\omega} \cdot \vec{\vec{\chi}}^{(2)}(-2\omega, \omega, \omega) \cdot \vec{e}_{\omega} \cdot \vec{e}_{\omega}$ under the approximations of a non-dispersive and localized response of the material. For our equations the effective nonlinear coefficient is defined as:

$$\chi^{(2)}_{eff} = \vec{e}_{2\omega} \cdot \vec{\vec{\chi}}^{(2)}(2\omega, \omega, -\omega) \cdot \vec{e}_{\omega} \cdot \vec{e}_{\omega} = \tfrac{1}{2} \vec{e}_{\omega} \cdot \vec{\vec{\chi}}^{(2)}(-\omega, 2\omega, -\omega) \cdot \vec{e}_{2\omega} \cdot \vec{e}_{\omega}. \quad \text{(IV.32)}$$

Taking all the preceding considerations, the complex coupled-wave equations take the following form:

$$\begin{aligned}\frac{\partial \bar{E}_{\omega}}{\partial z} &= \frac{-j\omega\,\chi^{(2)}_{eff}}{c\,n^{o}_{\omega}\cos^{2}\alpha_{\omega}}\,\bar{E}_{2\omega}\bar{E}^{*}_{\omega}e^{-j\Delta kz}\\ \frac{\partial \bar{E}_{2\omega}}{\partial z} &= \frac{-j\omega\,\chi^{(2)}_{eff}}{c\,n^{e}_{2\omega}\cos^{2}\alpha_{2\omega}}\,\bar{E}^{2}_{\omega}\,e^{j\Delta kz}\end{aligned} \qquad \text{(IV.33)}$$

In order to solve these equations, one can use the following transformations:

$$\begin{aligned}\bar{E}_{\omega}(z) &= \rho_{\omega}(z)\;e^{j\,\Phi_{\omega}(z)}\\ \bar{E}_{2\omega}(z) &= \rho_{2\omega}(z)\;e^{j\,\Phi_{2\omega}(z)}\end{aligned} \qquad \text{(IV.34)}$$

where $[\rho_{\omega}(z),\ \Phi_{\omega}(z)]$ and $[\rho_{2\omega}(z),\ \Phi_{2\omega}(z)]$ are the real amplitudes and the *nonlinear phases* of the FW and the SH fields, respectively.

$$\begin{aligned}\frac{d\rho_{\omega}}{dz} &= -\frac{\omega\,\chi^{(2)}_{eff}}{c\,n^{o}_{\omega}\cos^{2}\alpha_{\omega}}\,\rho_{\omega}\rho_{2\omega}\sin\Delta\Theta\\ \frac{d\rho_{2\omega}}{dz} &= \frac{\omega\,\chi^{(2)}_{eff}}{c\,n^{e}_{2\omega}\cos^{2}\alpha_{2\omega}}\,\rho^{2}_{\omega}\sin\Delta\Theta\\ \frac{d\Delta\Theta}{dz} &= \Delta k + \operatorname{cotan}\Delta\Theta\frac{d}{dz}\ln(\rho^{2}_{\omega}\rho_{2\omega})\\ \text{with}\quad \Delta\Theta(z) &= \Delta k\;z + \Delta\Phi(z)\end{aligned} \qquad \text{(IV.35)}$$

In this case, the total phase mismatch $\Delta\Theta$ contains two parts. The first one is the linear phase mismatch $\Delta k\,z$ and the second one is the nonlinear one $\Delta\Phi(z)$, which is equal to $2\Phi_{\omega}(z) - \Phi_{2\omega}(z)$.

From the first two of these equations one can obtain the Manley-Rowe relation, which, in this case of two waves, is equivalent to the conservation of power flow in a lossless dielectric:

$$W(z) = \frac{1}{2Z_0}\left[n^{o}_{\omega}\cos^{2}\alpha_{\omega}\,\rho^{2}_{\omega}(z) + n^{e}_{2\omega}\cos^{2}\alpha_{2\omega}\,\rho^{2}_{2\omega}(z)\right] \equiv W(0), \qquad \text{(IV.36)}$$

where Z_0 is the impedance of the vacuum. It is very useful to analyze these equations with normalized and dimensionless variables by introducing the following linear transformations:

$$u(\zeta) = \sqrt{\frac{2n_\omega^o}{Z_0 W}} \cos\alpha_\omega \, \rho_\omega(z)$$

$$v(\zeta) = \sqrt{\frac{n_{2\omega}^e}{Z_0 W}} \cos\alpha_{2\omega} \, \rho_{2\omega}(z) \qquad \text{(IV.37)}$$

$$\zeta = \frac{\omega \chi_{eff}^{(2)}}{c n_\omega^o \cos^2\alpha_\omega \cos\alpha_{2\omega}} \sqrt{\frac{Z_0 W}{n_{2\omega}^e}} z$$

where $u(\zeta)$ and $v(\zeta)$ are normalized field amplitudes as a function of the dimensionless variable ζ. The transformed equations become:

$$\frac{du}{d\zeta} = -uv \sin\Delta\Theta$$

$$\frac{dv}{d\zeta} = u^2 \sin\Delta\Theta \qquad \text{(IV.38)}$$

$$\frac{d\Delta\Theta}{d\zeta} = \Delta s + \operatorname{cotan}\Delta\Theta \frac{d}{d\zeta} \ln(u^2 v) \qquad \text{with } \Delta s = \Delta k \frac{z}{\zeta}$$

The power conservation relation takes the simple form:

$$u^2 + v^2 = 1. \qquad \text{(IV.39)}$$

In the next treatments, we shall study these equations under some assumptions about the initial conditions.

Perfect phase matching inside a nonlinear crystal ($\Delta k = 0$)

When the fundamental and the second harmonic have equal phases, i.e, $\Delta k(\theta) = 0$ and $\Delta\Theta = \Delta\Phi$, for an appropriate propagation angle θ that can be calculated from the equation (IV.30), one can readily integrate the third equation of (IV.38) to obtain a second constant of integration

$$\Gamma(\zeta) = u^2(\zeta) v(\zeta) \cos\left[\Delta\Phi(\zeta)\right] \equiv \Gamma(0). \qquad \text{(IV.40)}$$

Taking the second equation of (IV.38) and replacing $\sin\Delta\Theta = \sin\Delta\Phi$ by its value obtained from equation (IV.40),

$$\sin\Delta\Phi = \pm\sqrt{1 - \frac{\Gamma^2}{u^4 v^2}}, \qquad \text{(IV.41)}$$

and using equation (IV.39) for eliminating $u^2 = 1 - v^2$, yield a differential equation for v^2 whose general solution can be written as the incomplete elliptical integral,

$$\zeta = \frac{m}{2}\int_{v^2(0)}^{v^2(\zeta)} \frac{d(v^2)}{\sqrt{v^2(1-v^2)^2 - \Gamma^2}} \quad \text{with} \quad m = \operatorname{sign}\left[\sin\Delta\Phi(0)\right]. \quad \text{(IV.42)}$$

In the general case when $\Gamma \neq 0$, this gives an oscillatory behavior for v^2 between the two lowest positive roots of the denominator of the integral (IV.42) v_a^2 and v_b^2 where $0 \le v_a^2 < v_b^2 < v_c^2 \le 1$, and the period of this function is given by

$$\Pi_\zeta = \int_{v_a^2}^{v_b^2} \frac{d(v^2)}{\sqrt{v^2(1-v^2)^2 - \Gamma^2}}. \quad \text{(IV.43)}$$

This oscillatory behavior points out the fact that there is some kind of competition between the FW and its SH depending on the initial conditions at the entrance of the nonlinear crystal. Moreover, when the FW is maximum, we have a minimum for SH and vice-versa, and the maximum of FW will be a minimum after half a period (½Π_ζ), which is valid also for the SH. In other words when the FW passes from a maximum to a minimum, the SH passes from minimum to its maximum value: this situation is called second-harmonic generation or *up-conversion process*. In the opposite situation, when the FW passes from a minimum to a maximum, the SH passes from a maximum to its minimum value, a *down-conversion process* takes place. In the latter situation, even a very small amount of the SH intensity is needed to initiate the process.

A typical solution of the coupled-wave equations under $\Gamma \neq 0$ and nonzero incident fields is shown graphically in Figure IV-2. In the region A, the energy goes from the FW to the SH wave as indicated by the vertical arrows, while the transfer takes place in the opposite direction in region B. The maximum of the conversion process happens when the nonlinear-phase mismatch crosses the inflexion points (i.e. $d^2\Delta\Phi/d\zeta^2 = 0$) indicated by the two vertical dashed lines.

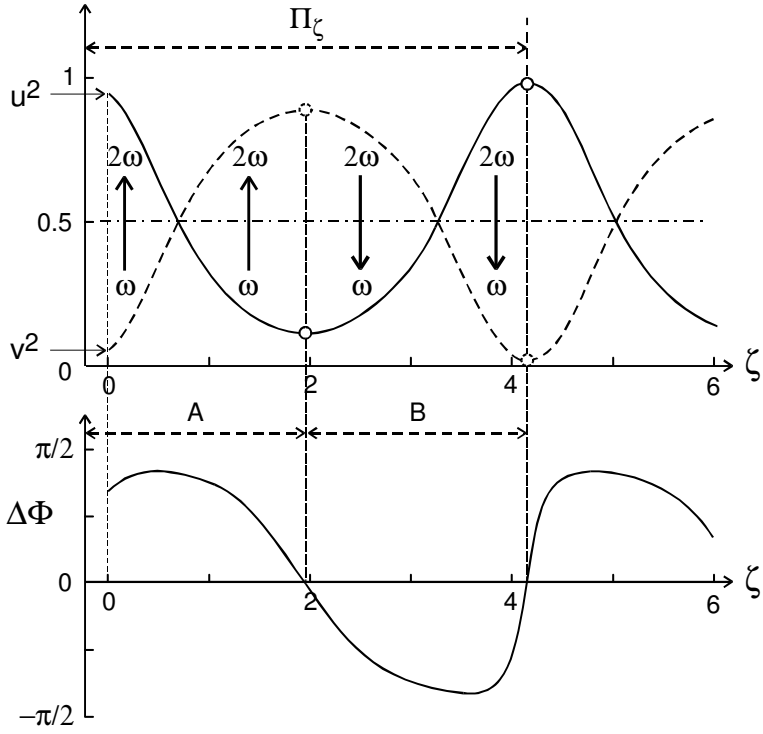

Figure IV-2: General solution of the normalized coupled-wave equations for arbitrary initial conditions. The upper curves show the evolution of the FW and SH powers along the propagation distance from the surface of the non linear crystal. The lower curve shows the nonlinear-phase variation. Region A (B) refers to the up- (down-) conversion process as indicated by the vertical arrows.

In the particular case when $\Gamma = 0$, the oscillatory behavior cancels, the period Π_ζ tends to infinity, and $\Delta\Phi$ is constant. Physically, this means that one can make the nonlinear crystal either an up-frequency converter when $m = +1$, or a down-frequency converter when $m = -1$, depending on the initial conditions. This case is important because the nonlinear phase will preserve its initial value over the length of the nonlinear crystal. The corresponding values of the nonlinear phases are $\pi/2$ for $m = +1$ and $-\pi/2$ for $m = -1$, respectively. Fortunately, in this case, the incomplete elliptical integral takes on a simple analytical form for the FW and SH amplitudes:

$$\begin{aligned} u(\zeta) &= \operatorname{sech}\left(\zeta + m\zeta_c\right) \\ v(\zeta) &= \tanh\left(\zeta + m\zeta_c\right) \\ \Delta\Phi(\zeta) &= \Delta\Phi(0) \qquad \text{with } \zeta_c = \operatorname{arctanh}\left[v(0)\right] \end{aligned} \quad . \qquad \text{(IV.44)}$$

THE SECOND-HARMONIC POWER CONVERSION EFFICIENCY FOR PERFECT PHASE MATCHING AND $\Gamma = 0$

As we mentioned above, a nonlinear crystal cut at the right phase-matching angle insures, when $m = +1$ the transfer of energy from the FW to SH. The power conversion efficiency η in SI units and for $oo \rightarrow e$ interaction takes the form

$$\eta(L) = \frac{v^2(L)}{u^2(0)} = \tanh^2\left(\frac{L}{L_{NL}}\right) \quad \text{and} \quad L_{NL} = \sqrt{\frac{(n_\omega^o)^3 \lambda^2}{8\pi^2 \chi_{eff}^2 I_\omega(0)}} \,. \qquad \text{(IV.45)}$$

Note that L_{NL} depends on the incident intensity $I_\omega(0)$. The conversion efficiency reaches 58% when $L = L_{NL}$ and a value higher than 99% can be obtained if the FW propagates through a nonlinear medium further than $3L_{NL}$ as shown on Figure IV-3. The curve (a) illustrates the expression (IV.45) in to the general case, when the beam is depleted. The curve (b) shows the case of the approximation of undepleted pump incident beam. The solution (a) is accurate within a 1% for $L = 0.12 L_{NL}$.

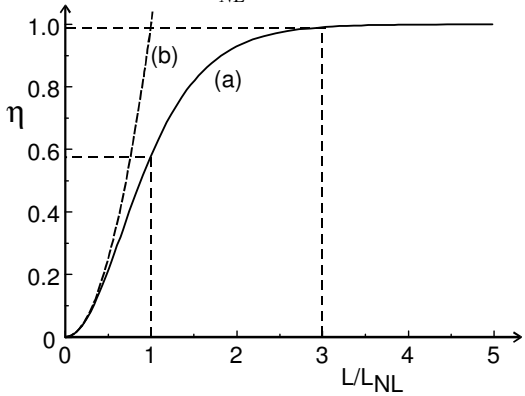

Figure IV-3: The second-harmonic power-conversion efficiency η as a function of the ratio L/L_{NL}. The curves (a) and (b) correspond to the depleted beam and undepleted beam conversion efficiencies under perfect phase matching and $\Gamma = 0$ conditions.

Arrangement of the phase mismatch in a FDNLM

As we mentioned before, the principle of pulse shortening by FDNLM is based on the double pass the YAG beam through the SH generation crystal. After the first pass, we should have the maximum of the SH power, i.e. the case of perfect phase matching $\Delta k = 0$. Thus, the total phase mismatch as defined in eq. (IV.35) takes the following form

$$\Delta\Theta(z) = \Delta k\, z + \Delta\Phi(z) = +\frac{\pi}{2}. \qquad \text{(IV.46)}$$

We emphasize that in this case ($\Gamma = 0$), the linear phase mismatch Δk is zero and the nonlinear phase mismatch $\Delta\Phi$ will get a constant value equal to $\pi/2$.

As the phase matching depends on the crystal orientation, the same behavior will be expected for the second pass inside the SHG crystal, except that the FW and SH waves should have a phase mismatch of about $-\pi/2$ in order to back convert the SH into FW (down-conversion process). Thus, the total phase mismatch is

$$\Delta\Theta(z) = \Delta k\, z + \Delta\Phi(z) = -\frac{\pi}{2}. \qquad \text{(IV.47)}$$

The change in the $\Delta\Theta$ value from $\pi/2$ to $-\pi/2$ for after the second pass can be obtained by free propagation in air.

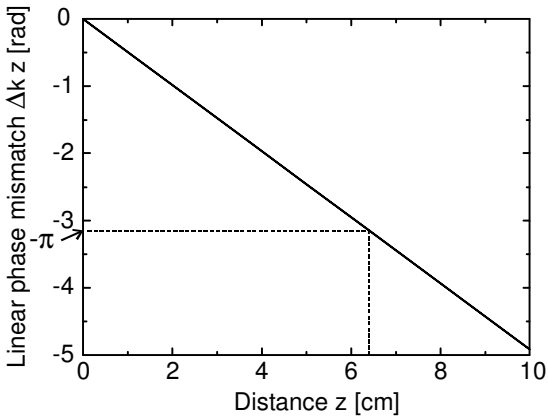

Figure IV-4: Linear phase mismatch Δk between the FW and SH of a YAG beam traveling in air.

Figure IV-4 shows the calculated linear mismatch between FW and the SH of the YAG laser based on the Ciddor model for the index of refraction of air,[24,25] that yields

$$\begin{aligned}\Delta\Theta(z) &= \Delta k\, z \\ &= \frac{4\pi}{1.064\,\mu m}\left[n_{air}(1.064\,\mu m) - n_{air}(0.532\,\mu m)\right] z\times 10^4 \\ &= \frac{4\pi}{1.064\,\mu m}\left[2.689\times 10^{-4} - 2.731\times 10^{-4}\right] z\times 10^4 \\ &= -0.492\, z\end{aligned}, \qquad \text{(IV.48)}$$

where the distance z is given in cm. It results that a dephasing of about $-\pi$ is obtained after traveling ~6.4 cm in air, which implies that the distance between the crystal and the dichroic mirror should be about 3.2 cm.

The variation of $\Delta\Theta$ for a double pass in the SHG crystal is shown in Figure IV-5. In the first pass we have $\Delta\Phi = \pi/2$ fixed inside the crystal by phase-matching condition. After the waves exit the crystal, The linear phase mismatch Δk will decrease linearly with distance z until a $-\pi/2$ value is achieved after travailing about 6.4 cm in air. The second pass through the crystal begins with $\Delta\Phi = -\pi/2$, which ensures an efficient energy conversion from SH to FW wave.

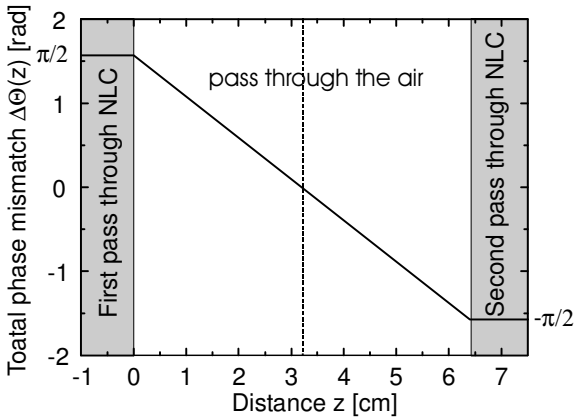

Figure IV-5: Variation of the total phase mismatch $\Delta\Theta$ in FDNLM configuration.

Conclusion

In this chapter, we solved the second-order coupled-wave equations using a classical electrodynamics description and its general solution behavior. In the case when the constant $\Gamma = 0$, we could demonstrate that the energy flows from FW to SH for m = 1 ($\Delta\Phi = \pi/2$) and from SH to FW for m= -1 ($\Delta\Phi = -\pi/2$). These results will now be used in the next chapter in order to investigate in detail, qualitatively and quantitatively, the operation of the FDNLM.

Chapter V Mode Locking by Frequency-Doubling Nonlinear Mirror

In this chapter, we shall describe some theoretical aspects of a passive mode-locking technique that uses a frequency-doubling nonlinear mirror (FDNLM). The choice of optimal parameters is discussed using a simple model. At the end of this chapter, we present our experimental results.

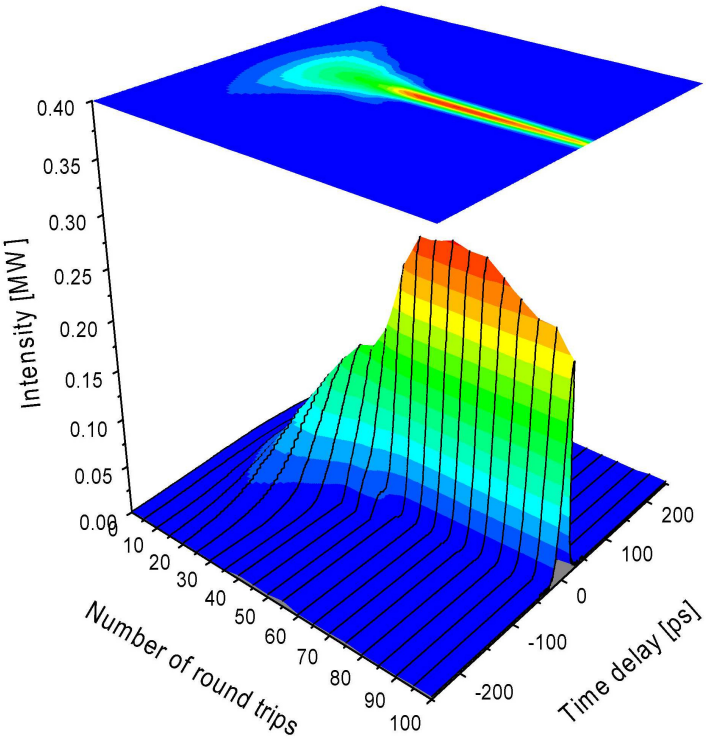

General description of the FDNLM

The general configuration of a nonlinear mirror consists of a nonlinear crystal and a dichroic mirror placed at a proper distance from the crystal. Since we choose a BBO crystal optimized for second harmonic generation (SHG), the setup is called frequency-doubling nonlinear mirror (FDNLM). This system is characterized by a variable reflection coefficient $R_N L$ with respect to the incident pulse intensity I_i. When the reflection coefficient and the gain increase with increasing intensity, the system acts as a positive-feedback element on the optical oscillator. The scheme of such a system is depicted in Figure V-1.

In the first pass of the fundamental wave (FW) laser pulse through the nonlinear SHG crystal, a pulse is generated at the second-harmonic (SH) frequency. The intensity of the SH pulse depends on the conversion coefficient η of the nonlinear crystal which, in turn, is proportional to the incident FW pulse intensity. The FW and SH are phase matched inside the crystal. At the surface of the dichroic mirror (DM), the FW pulse splits in two: a transmitted pulse (69%) and a reflected one (31%), whereas the SH pulse is totally reflected. The two reflected pulses (FW and SH) are then re-injected through the SHG crystal (second pass) with appropriate dephasing determined by the optical path and by the dispersion in air.

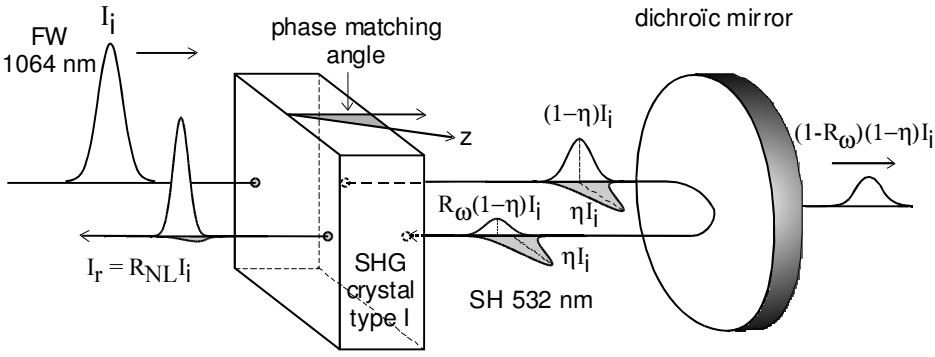

Figure V-1: Schematic view of the double pass into the nonlinear crystal. I_i is the incident intensity, η is the conversion coefficient to the second harmonic (SH is 532 nm for Nd:YAG laser), and R_ω is the reflection coefficient for the fundamental wavelength (FW 1064 nm for Nd:YAG laser).

Under these conditions, a parametric amplification takes place inside the nonlinear crystal, which increases the FW intensity by consuming the SH power. After these two passes of the pulse through the SHG crystal, the resulting reflection coefficient is very high for the high intensity part of the FW pulse and fairly low (~31%) for the small intensity part. Consequently, the pulse reflected backwards is significantly shorter in duration than the incident pulse. In other words, the higher the intensity, the higher the gain in the laser oscillator. This latter fact plays a major role for selecting the most intense pulse oscillating in the laser cavity, which is the mechanism of passive mode locking.

Passive mode locking of a pulsed Nd:YAG laser using of a frequency-doubling nonlinear mirror (FDNLM) was first demonstrated by Stankov in 1988.[4] In comparison to other means of passive mode locking, like the use of saturable dye absorber, this technology presents the following merits: photochemical stability, small response time, applicability to a wide spectral range, simplicity, self-starting mode locking.[5,6,7,8] Moreover, it enables passive, positive feedback as well as negative feedback[12] with the possibility of retrieving a significant amount from the fundamental in the second harmonic. The shortest pulse duration ever achieved with that technology applied to a pulsed YAG laser system, is the 25 ps recently reported by Chekhlov.[13]

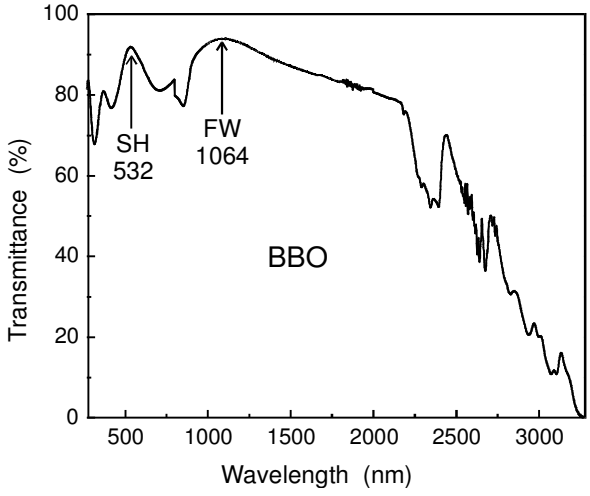

Figure V-2: Transmittance of a BBO crystal of 4 mm length with antireflection coatings for the FW (1064 nm) and its SH (532 nm).

In the next sections, we shall try to go deeply inside each step of the FDNLM mode-locking process in order to derive a simple model showing the choice of its physical parameters and predicting the limit of its performances.

Second-harmonic generation in a β-BBO crystal

The BBO (β-BaB_2O_4) is a negative uniaxial crystal belonging to the point group of *3m* symmetry. It has a good transmittance in the spectral range from 0.2 to 2.5 μm as shown in Figure V-2, where we can clearly see the effect of the coatings on the front and back surfaces of the crystal, which are aimed at minimizing the reflections of the 1064 and 532 nm wavelengths.

First, the BBO crystal should be cut at the phase-matching angle for type-I interaction as shown in Figure IV-1. Using the dispersion equations for the ordinary and the extraordinary indices, one can calculate the phase-matching angle from the expression:

$$\theta_{pm}^{I} = \arctan\left[\frac{n_{2\omega}^{e}}{n_{2\omega}^{o}}\sqrt{\frac{(n_{2\omega}^{o})^2-(n_{\omega}^{o})^2}{(n_{\omega}^{o})^2-(n_{2\omega}^{e})^2}}\right]. \qquad \text{(V.1)}$$

In the practical case when we have normal incidence, the cut angle θ_c is equal to the angle θ^{I}_{pm}, which takes the value of 22.8°.

As we mentioned before, the energy flow (Poynting vector $\boldsymbol{S}_{2\omega}$) of the SH field makes a small angle $\alpha_{2\omega}$ equal to 3.1° with the propagation direction $\boldsymbol{k}^{e}_{2\omega}$. Note that we overemphasize this angle on Figure IV-1, in order to show that the SH wavefronts propagate parallel to the FW wavefronts, which confirms the collinear propagation of the interacting waves $\boldsymbol{k}^{e}_{2\omega} // \boldsymbol{k}^{o}_{\omega}$.

The calculated conversion efficiency for different crystal lengths as a function of the incident beam intensity is shown on Figure V-3. We can see that the conversion efficiency increases with increasing crystal length and incident intensity, and that a high value, larger than 80%, can be achieved by using 3 or 4 mm thick crystals for an intensity higher than 10^9 W/cm^2. These high conversion efficiency values could be produced more easily with thicker crystals but we prefer thinner crystals for the following reasons:

- Less linear absorption and light diffusion in the crystal.
- Less group-velocity mismatch between FW and SH.

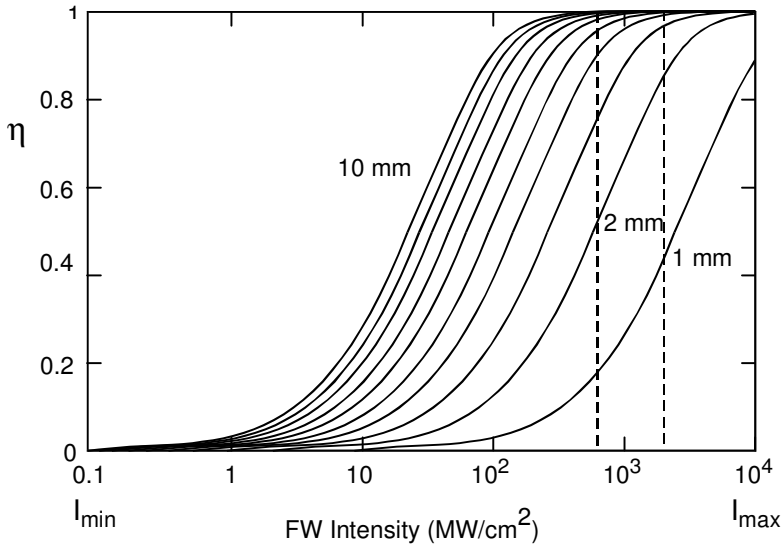

Figure V-3: Power conversion efficiency η of the BBO crystal as a function of the incident FW intensity in MW/cm^2. The different curves correspond to 1, 2, 3, 4, 5, 6, 7, 8, 9 and 10 mm crystal lengths, respectively from right to left.

- Better overlap of the interacting waves in spite of the presence of the walk-off angle. This is valid for diffraction-limited wavefronts, which is the case for the oscillating modes in the laser cavity.
- Larger acceptance angle when we have a tight focusing into the nonlinear crystal. This is very important for improving the phase-matching quality, which determines the overall conversion efficiency of the nonlinear process.
- Using thinner crystals permits to avoid the saturation of the generated SH. This phenomenon could produce a flat pulse-shape when we take into account the temporal and spatial shapes of the laser mode.

These remarks question the assumptions used for deriving the coupled-wave equation. This will drive us to focus on the phenomena that affect the nonlinear process, taking into account the real characteristics of the laser beams.

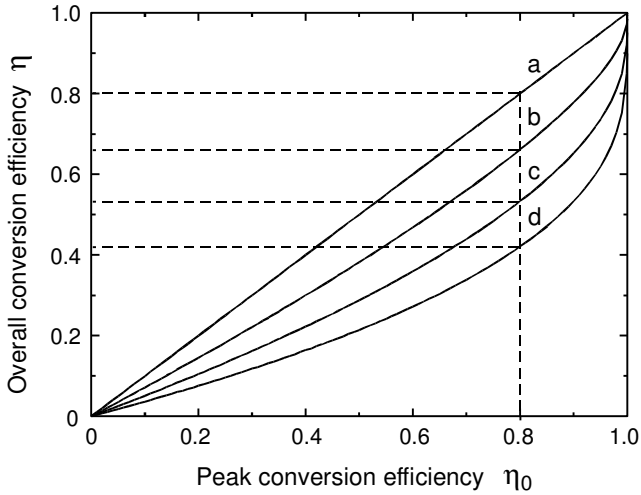

Figure V-4: Overall conversion efficiency as a function of the peak-conversion efficiency. The curves correspond to: (a) CW plane wave, (b) temporal Gaussian pulse, (c) spatial TEM_{00} mode and (d) pulsed TEM_{00} mode under plane wave assumption, respectively.

Limitations of high-efficiency second-harmonic generation

In the previous discussion we found (see eq IV-43 and Fig IV-3) that a conversion efficiency η as high as 99% can be predicted under plane wave and perfect phase-matching conditions. In the practical case, the latter assumptions cannot be completely fulfilled due to Gaussian beam propagation in the oscillator and imperfect phase matching. The Gaussian beam propagation implies that the wavefronts are generally curved except in the beam waist and at long distance. As our crystal is installed in the laser cavity with tight focusing, the plane wave approximation can be fulfilled if the thickness L of the nonlinear crystal is smaller than the beam waist. This brings one additional argument for choosing thinner crystals. At high intensity, the phase matching can be degraded due to phase and cross phase modulations of the FW pulse. These optical phenomena have been discussed in detail in the references.[26,27,28]

First, we emphasize the difference between *peak-conversion efficiency* η_0 as described by equation IV-45 for the case of a plane wave and *overall conversion efficiency* η in the more practical cases of a Gaussian temporal profile and of a Gaussian spatial distribution, which is called TEM_{00} mode.

	Gaussian pulse		TEM_{00} mode		Gaussian + TEM_{00} mode	
η_0	η_t	Reduction	η_s	Reduction	η_{ts}	Reduction
0.01	0.0071	0.71	0.0051	0.50	0.0036	0.35
0.10	0.072	0.72	0.051	0.51	0.037	0.37
0.25	0.183	0.73	0.133	0.53	0.096	0.39
0.50	0.38	0.76	0.29	0.58	0.21	0.43
0.80	0.66	0.83	0.53	0.67	0.42	0.53
0.95	0.85	0.90	0.74	0.78	0.62	0.65
0.99	0.93	0.94	0.85	0.86	0.75	0.76

Table V-1: Tabulated overall conversion efficiency versus peak-conversion efficiency for different pulse models.

The overall conversion efficiency (OCE) for a Gaussian pulse (temporal profile) can be obtained by the following integral

$$\eta_t(\eta_0) = \frac{\int_0^\infty \eta(t,\eta_0) I(t)\, dt}{\int_0^\infty I(t)\, dt}. \tag{V.2}$$

In the same manner, we can define the OCE for a TEM_{00} transversal mode as follows

$$\eta_s(\eta_0) = \frac{\int_0^\infty \eta(r,\eta_0) I(r)\, rdr}{\int_0^\infty I(r)\, rdr}. \tag{V.3}$$

Finally, the OCE for a pulsed TEM_{00} can be written as

$$\eta_{ts}(\eta_0) = \frac{\int_0^\infty \int_0^\infty \eta(r,t,\eta_0) I(t,r)\, rdrdt}{\int_0^\infty \int_0^\infty I(t,r)\, rdrdt}, \tag{V.4}$$

where the intensity $I(t,r)$ for the pulsed TEM_{00} mode with a pulsewidth τ and a beam waist w is given by

$$I(t,r) = I(t)I(r) = \exp\left[-4\ln 2(t/\tau)^2\right]\exp\left[-2(r/w)^2\right]. \tag{V.5}$$

One can note from the Figure V-4 that the overall efficiency is generally smaller than the peak-conversion efficiency, that the difference is larger for high peak-efficiency value, and that the difference increases when taking into account the temporal, spatial, and both spatial-temporal behaviors of the laser beam, respectively. Table V-1 gives the overall conversion efficiency for some typical peak-conversion values within the different models proposed.

Basic equations of the nonlinear reflection coefficient (Stankov model)

In this section, we describe the temporal behavior of the FDNLM for one reflection using an intensity-dependent reflection coefficient in order to investigate its optimal physical parameters. First, we consider that the temporal shape of the incident optical pulse is a Gaussian function with FWHM equal to unity, as follows:

$$I(t) = \exp(-4t^2 \ln 2). \tag{V.6}$$

The nonlinear reflection coefficient R_{NL} of the FDNLM is given by the relation (this expression is demonstrated in chapter XI):

$$R_{NL}(t,\eta_0,R_\omega) = B(t)\left\{1-\tanh^2\left[\sqrt{B(t)}\,\operatorname{atanh}\sqrt{\eta(t)} - \operatorname{atanh}\sqrt{\eta(t)/B(t)}\right]\right\}, \tag{V.7}$$

where $\eta(t)$ is the instantaneous conversion efficiency deduced from equation IV-45, by introducing a time varying intensity I(t):

$$\eta(t) = \tanh^2\left[\sqrt{I(t)}\,\operatorname{atanh}\sqrt{\eta_0}\right]. \tag{V.8}$$

η_0 is the peak conversion efficiency at $t = 0$ defined by equation IV-43. $B(t)$ is the fraction of the total intensity (FW + SH) reflected by the dichroic mirror and reentering the nonlinear crystal for the second pass

$$B(t) = \eta(t) + [1-\eta(t)]R_\omega. \tag{V.9}$$

R_ω is the reflection coefficient for the FW and corresponds to the value of the non linear reflection coefficient R_{NL} for small signal intensity [$I(t) \to 0 \Rightarrow \eta(t) \to 0$] .

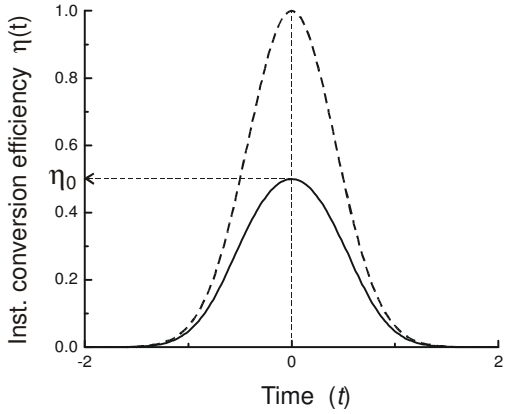

Figure V-5: Instantaneous conversion efficiency vs. time in the case of a Gaussian pulse represented by the dashed line (for $\eta_0 = 0.5$).

It is noteworthy that these equations have been derived for the case of interest, i.e, when the dichroic mirror is totally reflecting the SH and when a dephasing of $\Delta\phi = 2\pi p - \pi/2$ (p is an integer) is introduced between the FW and SH waves in the second pass into the nonlinear crystal. In this case the reflected pulse is given by:

$$I_r(t) = R_{NL}(t) I(t) . \qquad \text{(V.10)}$$

The previous equations show that the reflected pulse is completely determined if we know the peak conversion η_0 and the reflection coefficient R_ω for the fundamental wavelength. On the other hand, it remains some figures of merit to be defined in order to characterize the good functioning of this device.

At first, we can take the ratio between the reflected and the incident pulsewidths, which is called the pulse-shortening ratio (PSR). The calculation of the PSR is depicted on Figure V-6. We notice that the PSR decreases with η_0 and increases with R_ω. The PSR reaches its minimum for $\eta_0 = 0.77$ and $R_\omega = 0$. Therefore, we see from these curves that the best choice is to get the maximum of SH conversion into the nonlinear crystal and to have R_ω as low as possible. The latter result seems to be a good argument for the conversion coefficient η_0 but not convincing for R_ω because a very small value or zero means that the reflected power will also tend to zero as shown in Figure V-7.

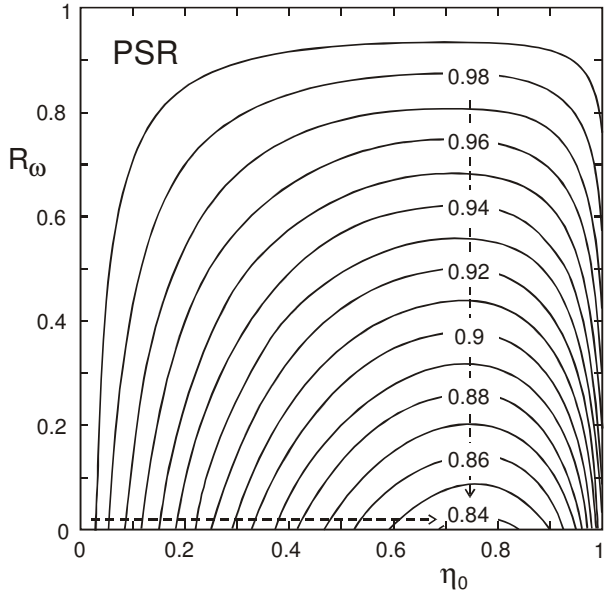

Figure V-6: Contour lines of the PSR as a function of peak-conversion coefficient η_0 (horizontal) and reflection coefficient R_ω(vertical). The arrows point to the values of η_0 and R_ω that yield the lowest PSR.

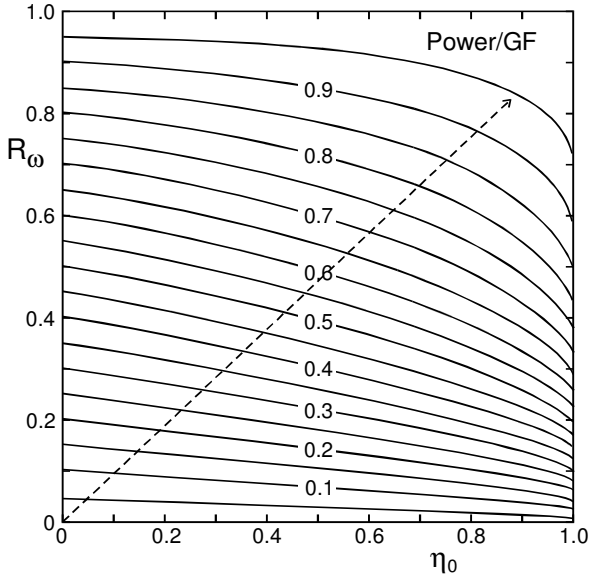

Figure V-7: The reflected power of an incident Gaussian pulse. The power is normalized to the incident pulse power (Gaussian Factor GF = $\frac{1}{2}\sqrt{\pi/\ln 2}$). Note that: the normalized reflected power tends to 1 at η_0= 1 whatever the R_ω value.

Figure V-7 shows that the reflected power increases both with increasing η_0 and with R_ω. The reflected power equals R_ω when $\eta_0 = 0$, which means that the device works without the crystal and the reflection in this case is due to the dichroic mirror for the FW.

For a fixed value of η_0 (respectively R_ω) the normalized power increases with R_ω (respectively η_0), till it reaches 1 (its maximum value) at R_ω =1 (respectively η_0 =1). Thus, Figure V-6 and Figure V-7 show that the best operation of the FDNLM is obtained for high conversion efficiency values; however, we cannot determine whether we should take R_ω=0 (for the best PSR), or R_ω=1 (for the best reflected power). This fact leads us to define the compression factor (CF) of the pulse, which increases when we have shorter pulsewidth and higher amplitude for the reflected Gaussian pulse:

$$CF = \frac{PSR_{\max} - PSR}{PSR_{\max} - PSR_{\min}} \times \frac{I_r(0) - I_{r\min}(0)}{I_{r\max}(0) - I_{r\min}(0)}, \qquad \text{(V.11)}$$

where the maximum and minimum values have been taken over the entire variation of η_0 and R_ω. Figure V-8 shows contour lines of the CF with respect to η_0 and R_ω. In our case, the CF takes value from 0 to $CF_{max} < 1$ depending on whether the PSR is close to its maximum and $I_r(0)$ to its minimum, or vice versa.

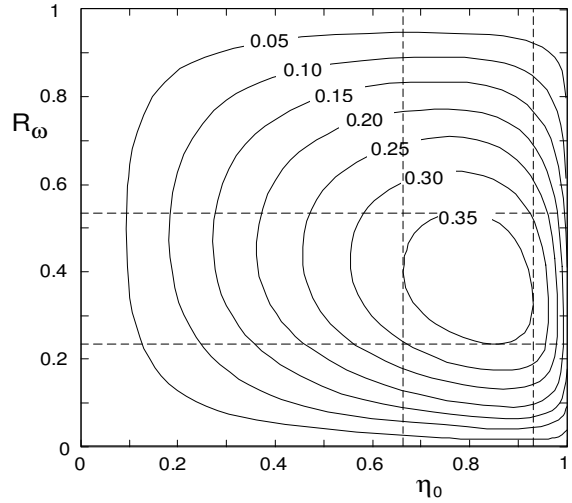

Figure V-8: Contour lines of the pulse compression factor CF described as a function of the peak-conversion coefficient η_0 and the small-signal reflection coefficient R_ω.

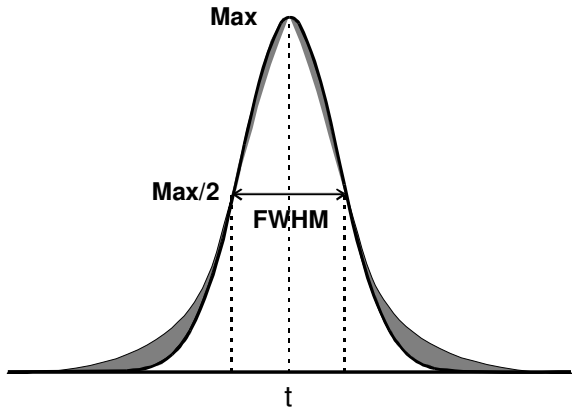

Figure V-9: The dark line is a Gaussian profile that matches the maximum and the FWHM of the deformed pulse. The gray surface area divided by the Gaussian area gives the Gaussian shape factor (GSF).

The CF reaches its maximum (CF_{max}= 0.35) on the region where η_0 is in the range from 0.66 to 0.92 and R_ω is in the range from 23% to 54%.

In the previous discussion, our choice for the basic parameters of the FDNLM device did not take into account the shape of the reflected pulse although it is an important factor for making a good oscillator, especially when the FDNLM is installed as the output coupler, since the reflected and transmitted pulses will be deformed by the nonlinear reflection coefficient of this device. For that purpose, we define a *Gaussian shape factor* (GSF) describing how the reflected pulse is distorted from the Gaussian shape by measuring the area confined between the reflected pulse and a Gaussian pulse which shares the same peak intensity and FWHM as shown in Figure V-9.

As depicted on Figure V-10, the GSF presents a small value on the region where the CF reaches its maximum value; for example, following the arrow on Figure V-10, the GSF is reduced by a factor 4 while the CF is increasing, as shown on Figure V-8. This fact is interesting because, intuitively, could have expected that a high compression would have resulted in a high deformation of the pulse, i.e. a higher GSF value.

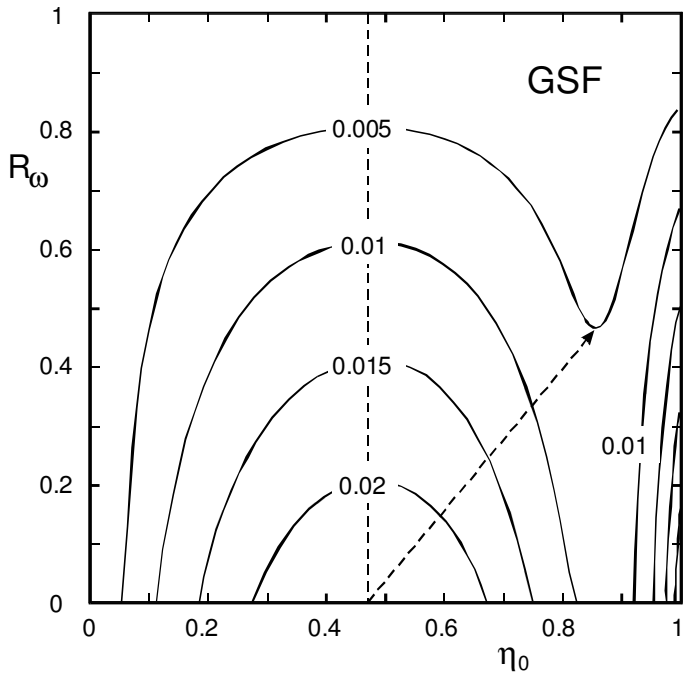

Figure V-10: Gaussian shape factor (GSF) as function of the peak-conversion coefficient η_0 (horizontal) and the reflection coefficient R_ω (vertical).

Thus, if we chose correctly R_ω and η_0, this device has the ability to compress the incident pulse without an additional deformation. This gives another advantage for using this device.

To include this fact in our calculation, we make the product of the CF with the relative GSF to give what is called the decision factor (DF), as follows:

$$DF = CF \times \frac{GSF_{\max} - GSF}{GSF_{\max} - GSF_{\min}}. \qquad \text{(V.12)}$$

The variation of this factor is shown on Figure V-11, where one can see that the best theoretical operation of this device is situated in the region A, where $\eta_0 \in$ [0.75, 0.85] and $R_\omega \in$ [0.25, 0.50]. Peak-conversion coefficient of 0.8 is a very high value and it can be achieved under special conditions with a TEM_{00} mode, as we shall see in a further paragraph.

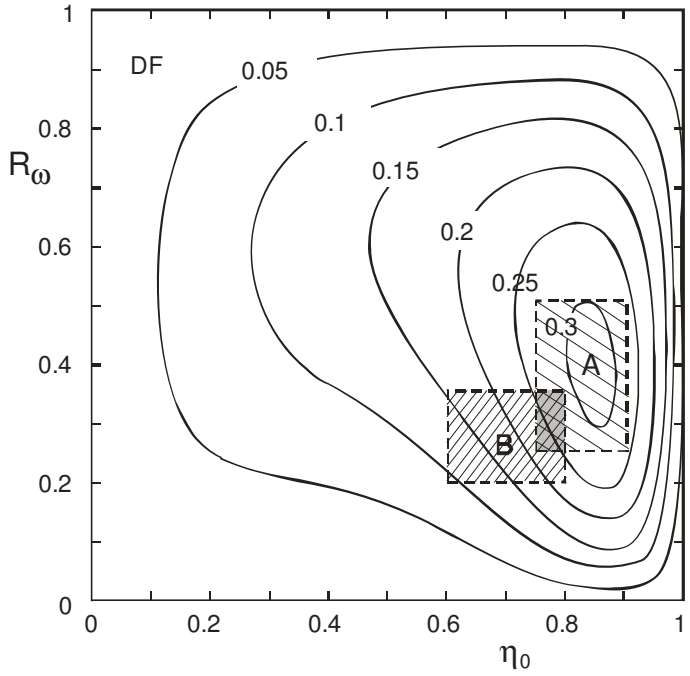

Figure V-11: The decision factor (DF) as function of the peak-conversion coefficient η_0 and the reflection coefficient R_ω.

In practical situations, the peak-conversion coefficient can have values between from 0.5 and 0.8 with tight focusing in the NLC. Thus, the practical operating domain lies in the B region of Figure V-11, where $R_\omega \in$ [0.2, 0.35].

Additionally, it is noteworthy that the response of this device is not the same for different pulse shapes that share the same peak intensity and FWHM. In Figure V-12, we represented four normalized functions: Rectangular (R), Gaussian (G), Lorentzian (L), and (AS), which is the square inverse hyperbolic sin function divided by *t*.

$$AS(t) = \text{arcsinhc}^2(t) = \left[\frac{arcsinh(t)}{t}\right]^2. \qquad \text{(V.13)}$$

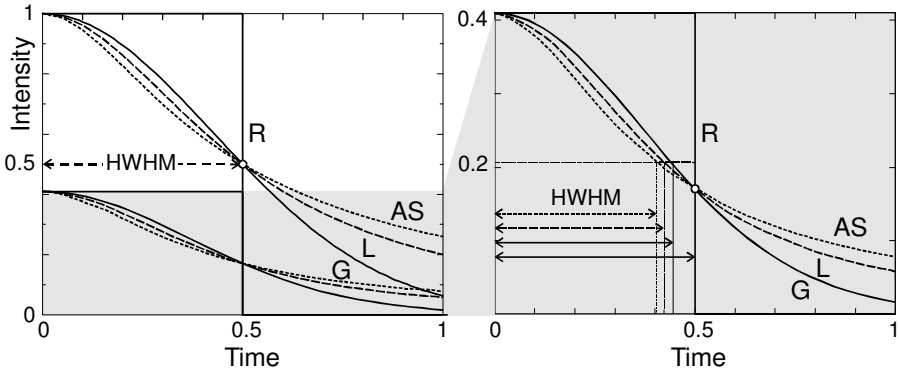

Figure V-12: Left panel: Normalized pulse shapes: (R) Rectangular, (G) Gaussian, (L) Lorentzian and, AS that stands for $\mathrm{arcsinhc}^2(t)$. Above: incident pulses; Below: reflected pulses. The right panel displays a magnification of the reflected pulses for $\eta_0 = 0.6$ and $R_\omega = 0.25$.

The reflected pulse shapes are shown on the right panel of Figure V-12. One can see that the AS pulse has the smallest FWHM and that the R pulse FWHM is unchanged, indicating that a rectangular pulse is uncompressible by this kind of device. Therefore, the FDLNM is a pulse-shape sensitive device. Thus the variation of the PSR shall be partly assigned to cumulative deformations of the pulse after multiple reflections by the FDNLM.

Table V-2 gives the calculated values of reflected peak intensity and PSR for $\eta_0 = 0.6$ and $R_\omega = 0.25$, which correspond to a relatively high deformation of the pulse (GSF ~2% see Figure V-10). In the last column, we give the smallest PSR that can be obtained by the FDNLM for the different pulse shapes. We notice a PSR variation of about 7% and up to 10% between the Gaussian and the AS shape, showing that this effect is not negligible at all.

Steady-state pulse duration (Barr Model)

The Barr Model[29] demonstrates that the steady-state pulsewidth is determined by a balance between pulse shortening by the nonlinear mirror (FDNLM) and pulse stretching through the gain medium. In addition, we show that a Fourier-transform limited pulse can be generated in principle.

Pulse Shape	$\eta_0 = 0.6$ $R_\omega = 0.25$		PSR_{min}
	Peak intensity	PSR = FWHM	
Rectangular	0.41	1	1
Gaussian	0.41	0.885	0.836
Lorentzian	0.41	0.851	0.791
arcsinhc	0.41	0.817	0.752

Table V-2: Calculated values of reflected peak intensity and PSR for $\eta_0 = 0.6$ and $R_\omega = 0.25$. The last column shows the theoretical limit of the PSR value that can be obtained by FDNLM for the different pulse shapes.

THEORY

The expression of the nonlinear reflection coefficient R_{NL} has been given by equation (V.7) as a function of the peak-conversion efficiency η_0 and of the fundamental intensity reflection coefficient R_ω. The normalized reflectivity R_{NL}/R_ω is plotted in Figure V-13 on a logarithmic scale where one observes a near exponential dependence on η, so that the following approximation can be made

$$R_{NL}(t,\eta_0,R_\omega) \simeq R_\omega e^{\sigma(R_\omega)\ \eta(t,\eta_0)}. \qquad \text{(V.14)}$$

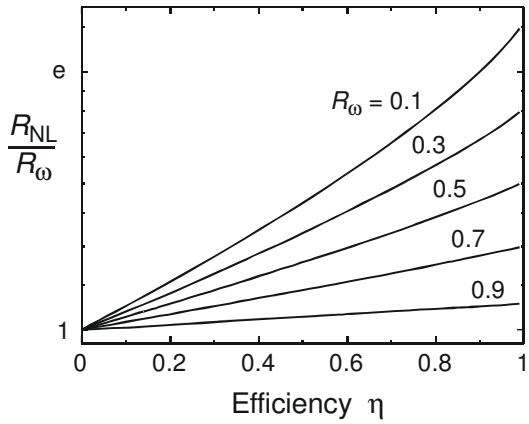

Figure V-13: Normalized nonlinear reflectivity as a function of the conversion efficiency plotted on a semi-logarithmic scale.

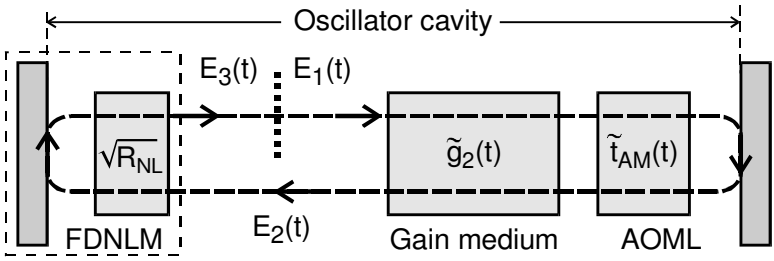

Figure V-14: Model of a cavity with active, passive mode locking. $\tilde{E}_1(t)$ is pulse profile of the starting field while $\tilde{E}_2(t)$ is the pulse after a double pass in the gain medium and the AM mode locker. Finally $\tilde{E}_3(t)$ is the pulse reflected by the FDNLM.

The parameter σ, whose values are given in Table V-3, is a function of R_ω. This approximation, which deviates to a maximum of 5% from the exact curve calculated by equation (V.7), is helpful to derive an analytical expression for the steady-state pulsewidth.

The cavity that will be analyzed is schematized in Figure V-14. The optical pulse travels clockwise inside the cavity. First, it passes through the AOML and, then, the gain medium and, finally, it will be reflected by the FDNLM. The passage of the optical pulse $E_1(t)$ through the gain medium and the AOML is given in the time domain by

$$\tilde{E}_2(t) = \tilde{t}_{AM}(t)\left[\tilde{g}_2(t) * \tilde{E}_1(t)\right]. \tag{V.15}$$

Here $\tilde{g}_2(t)$ is the inverse Fourier-transform frequency-dependent gain $\tilde{g}_2(\omega)$ for the double-pass and $\tilde{t}_{AM}(t)$ is the amplitude transmission coefficient for a double pass of in the modulator, as have been previously described by equations (III.17) and (III.25), respectively. The field reflected by the FDNLM is given by

$$\tilde{E}_3(t) = \sqrt{R_{NL}(t)}\tilde{E}_2(t). \tag{V.16}$$

The final expression for the pulse evolution after one single round trip in the cavity is

$$\tilde{E}_3(t) = \sqrt{R_{NL}(t)}\tilde{t}_{AM}(t)\left[\tilde{g}_2(t) \otimes \tilde{E}_1(t)\right]. \tag{V.17}$$

Under the steady-state condition, the round trip pulse will be identical to the initial one $\tilde{E}_1(t)$, which yields

$$\tilde{E}_3(t) \equiv \tilde{E}_1(t). \tag{V.18}$$

Notice that the inclusion of the FDNLM will generally deform the pulse profile but, as we can see from Figure V-10, under certain conditions, the pulse shape remains almost Gaussian. In this case, an analytical solution can be obtained for the steady-state pulse.

As we have seen in chapter III, the transmission function of the modulator $\tilde{t}_{AM}(t)$ and the gain $\tilde{g}_2(\omega)$ have Gaussian shapes, as given by the equation (III.26) and (III.17), respectively. The function $\tilde{g}_2(t)$ is calculated using inverse Fourier transform

$$\tilde{g}_2(t) = \int \tilde{g}_2(\omega) e^{j\omega t} d\omega = \sqrt{\frac{\pi}{\alpha}}\, e^{g_m} \exp\left[-(t-\beta)^2 / 4\alpha\right] e^{j\omega_a t} \quad . \tag{V.19}$$

where $\alpha = 4g_m / \Delta\omega_a^2$ and $\beta = 2g_m / \Delta\omega_a$

If we take an unchirped, Gaussian input pulse centered at the peak of the gain profile given by the expression (III.18) and a low conversion efficiency $\eta_0 < 0.2$, the application of the steady-state condition will give the complex Gaussian parameter

$$\gamma_\eta = \frac{\sigma\eta_0}{4\alpha(1+\sigma\eta_0)} \tag{V.20}$$

and the FWHM of the intensity profile can be written as follows

$$\boxed{\tau_\eta = \frac{2\sqrt{2\ln 2}}{\pi} \sqrt{\frac{g_m(1+\sigma\eta_0)}{\sigma\eta_0}} \frac{1}{f_a}}. \tag{V.21}$$

Values of the steady-state pulse lengths were calculated using the expression (V.21) and an iterative numerical method based on equation (V.16) ($f_a = \Delta\omega_a/2\pi$ =120 GHz for Nd:YAG). One can multiply the expression (V.21) by a correction factor F in order to compensate for the difference between the exact and approximate solutions. The value of this factor is in the range from 1.3 to 1.5 (see Table V-3 that is reproduced from Ref. 29, except for the last line calculated for our FDNLM configuration).

R_ω	σ	η_0	e^{2g_m}	Pulse duration			F
				Active ML [ps]	Active-passive approx [ps]	Active-passive exact [ps]	
0.80	0.20	0.10	1.22	72.5	13.8	21.3	1.5
0.30	0.85	0.10	3.06	111.3	16.7	25.8	1.5
0.20	1.00	0.10	4.52	119.9	18.0	27.2	1.5
0.20	1.00	0.20	4.09	117.8	12.8	18.4	1.4
0.20	1.00	0.30	3.70	115.7	10.5	14.7	1.4
0.20	1.00	0.50	3.03	111.0	8.1	10.6	1.3
0.20	1.00	0.80	3.03	111.0	7	7×1.3 = 9	1.3

Table V-3: Pulse duration of active, passive mode-locked laser with FDNLM under the steady-state condition (reproduced from Ref. 29). The last line corresponds to the configuration used in this work.

Experimental setup and results

The laser configuration is depicted in Figure V-15. The 115-mm length and 7-mm diameter Nd:YAG crystal rod is pumped by two flashlamps. The electric pump energy and repetition rate are about 20 J and 20 Hz, respectively. Two antireflection-coated lenses with focal lengths of 100 mm and – 40 mm form the telescope (T). A diaphragm (D) restricts the operation to one single transversal mode. The acousto-optic modelocker AOML (Intra action ML-50B, faces cut for Brewster angle) is located close to the mirror (M). The cavity length of about 1.5 m is matched to the AOML modulation frequency of 100 MHz. The laser cavity is closed from the AOML side by a high reflectivity mirror (M) with 10 m radius of curvature. On the other side, the FDNLM consists of a 7-mm long BBO crystal, cut for oo-e type second-harmonic generation ($\theta = 22.8°$) and a dichroic mirror with reflectivity above 99 % at 532 nm and equal to 31% at 1064 nm.

The nonlinear crystal mounting allows angle tuning and translation along the laser cavity axis. The pulse train envelopes are monitored using a p-i-n photodiode (rise time less than 1 ns) in combination with a digital oscilloscope. A standard background-free (noncolinear) SHG autocorrelator is used to measure the pulse duration.

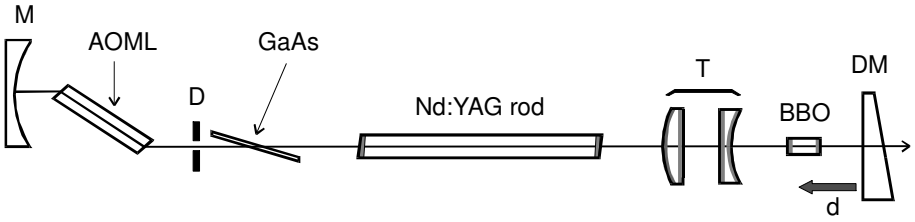

Figure V-15: Experimental setup: AOML, acousto-optic modelocker; M, high reflectivity curved mirror (R = -10 m); DM, dichroic mirror; L_1, L_2 telescope lenses (f_1 = 100 and f_2= -40 mm); D, diaphragms. The gray edges represent the antireflection coatings for 1064 and 532 nm.

In the following sections, we shall present two sets of experimental results. The first one concentrates on the study of the temporal pulse evolution. It has been obtained with the YAG rod in the middle of the cavity and without optimizing the position of the different optical elements, which will be taken into consideration in the second set of experiments.

FIRST EXPERIMENTAL OBSERVATIONS[30]

When the BBO crystal is tuned to the phase-matching angle and translated at 30 mm from the dichroic mirror, a noticeable increase of the SHG intensity reveals the efficient mode locking of the YAG oscillator. The average output power is 12 mW (pulse-train energy = 0.6 mJ) for an electric pump energy of 16.8 J. The envelope of the 1 µs long pulse trains is presented in Figure V-16-a. Because of its 100MHz bandwidth, the oscilloscope amplifier acts as an integrator for the fast diode signal; therefore, the trace of Figure V-16-a shows the time evolution of the optical pulse coupled out of the laser cavity. The starting part of the envelope (0-500 ns) is characterized by a rapid variation of the pulse energy while a second portion (600-950 ns) is characterized by quasi-constant pulse energy. We estimate pulse energy of 7 µJ, 400 ns after the beginning of the train and 4 µJ, after 800 ns. The pulse duration measurements are averaged over a 50 ns temporal window spanning five laser pulses. The width of the autocorrelation traces reaches its shortest value of 17 ps (FWHM) at the end of the train envelope (temporal window between 950 and 1000 ns). A satisfactory fit is achieved assuming a Gaussian profile for the fundamental pulse, enabling to infer a pulse duration FWHM of 12 ps (Figure V-17).

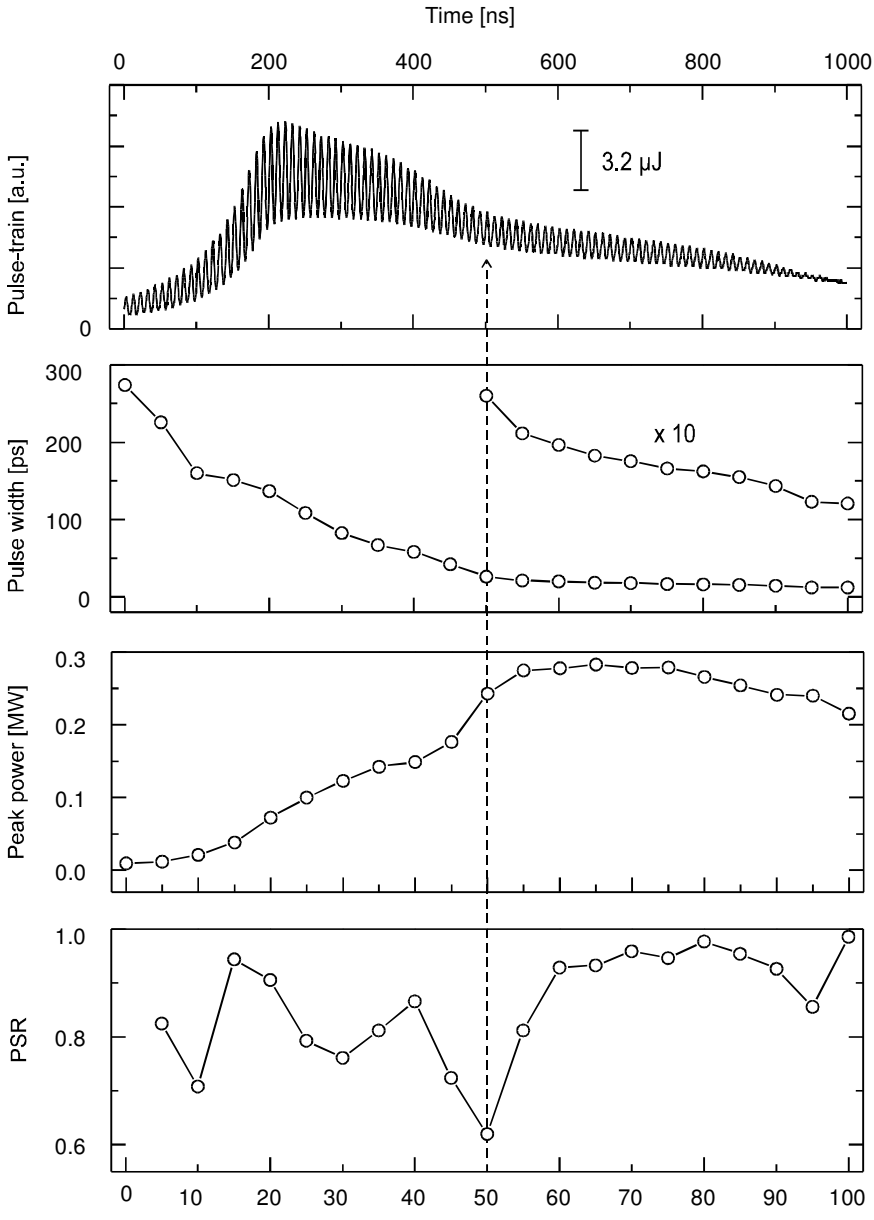

Figure V-16: (a) Pulse-train envelope as measured by a 100-MHz bandwidth oscilloscope. (b) Fundamental pulsewidth determined by least square fit the autocorrelation traces with a Gaussian profile. (c) Calculated peak power expressed in MW.
(d) Pulse-shortening factor as a function of the round-trip number.

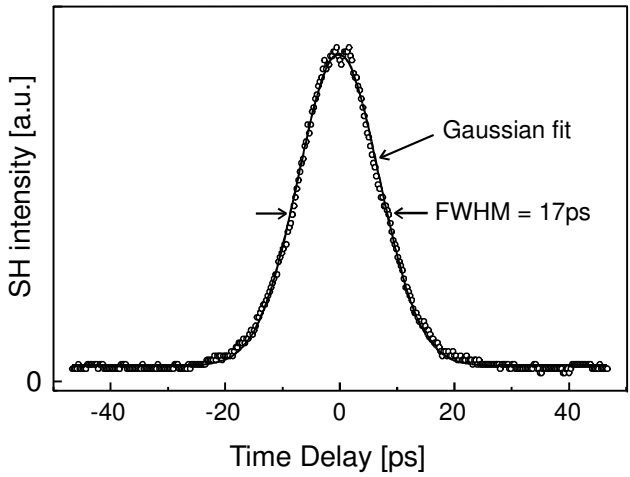

Figure V-17: Autocorrelation trace of the 1064-nm pulses measured at the end of the pulse train. Opened circles: experimental data point, continuous line: least square fit to the autocorrelation of fundamental Gaussian pulse duration of 12 ps.

The complete temporal evolution of the fundamental pulsewidth and the corresponding peak power are presented in Figure V-16-b and -c respectively. The peak power values are deduced from the pulse energies, as measured by the pulse train envelope (Figure V-16-a), and the fundamental pulsewidth. We note that the fundamental pulsewidth becomes as short as 26 ps after approximately 50 round trips. This shortening is accompanied by a significant increase of the peak power. A similar behavior of the FDNLM has been predicted by a theoretical analysis.[9] The peak power stabilizes between the 50^{th} and the 90^{th} round trip. This must be related to the two-photon absorption in the GaAs platelet, which acts as an intracavity intensity limiter.

We estimate that the intracavity peak intensity reaches a value of the order of 55 MW/cm^2, which is in agreement with the onset of two-photon absorption in such a semi-conductor.[31] From the 50^{th} to the 90^{th} round-trip, the fundamental pulse duration slowly decreases from 25 to 17 ps. At the end of the pulse train (i.e. after 90 round trips), a pulse duration as short as 12 ps is produced while the peak power slightly decreases due to the depletion of the energy stored in the Nd:YAG rod.

By taking the derivative of the pulse duration with respect to the number of round trips, we can derive the evolution of the pulse-shortening ratio (PSR). Figure 2-d reveals an average value of 0.81 from the first to the 45th round trip down to 0.62 between the 45th and the 50th round trip. The latter value is remarkably smaller than ~1/√2, which is the smallest A PSR, predicted by the numerical modeling of the FDNLM presented by Stankov.[10] PSR shorter than 1/√2 has only been predicted in the modeling of Buchvarov *et al,*[11] which takes the possible occurrence of a self-phase modulation in the oscillator into account. The PSR increases however to 0.93 between the 50th to the 90th round trip. This may be related to the pulse stretching effect produced by the saturated GaAs platelet, which, in this case, acts as a negative feedback element in the laser oscillator. Finally, significant pulse shortening is still achieved after the 90th round trip when the YAG rod energy is depleted. This last observation along with the fact that the maximum efficiency of the FDNLM is obtained before the peak power reaches saturation, points to the possibility of improving further the performances of the oscillator by modifying the balance of the fluence on the FDNLM and on the GaAs platelet. This can be achieved, for example, by modifying the telescope power.

INTERPRETATION OF THE PSR MEASUREMENTS

As we mentioned before, the PSR is the ratio between two successive pulsewidths. In our experimental setup, due to technical limitation, the pulse duration is measured over five pulses; therefore, the PSR calculated by taking the ratio between two successive measurements also integrates five pulses. The measured PSR is thus a little different from the real one. In order to correct the measured values, we assume that the intensity trace is a superposition of five Gaussians with PSR. The total intensity for a superposition of N Gaussian pulses is:

$$I_{app}(t) = \sum_{n=1}^{N} \exp\left[-4\ln 2 \left(\frac{t}{PSR^{n-1}\tau_1} \right)^2 \right], \qquad \text{(V.22)}$$

where τ_1 is the pulsewidth of the first pulse. The apparent PSR between the first and the N^{th} pulsewidth is given by the approximate expression

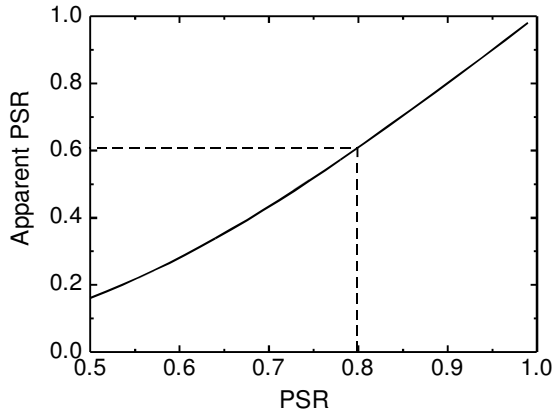

Figure V-18: Apparent PSR as a function of the real PSR plotted from Eq.(V.23).

$$PSR_{app} \cong N\frac{1-PSR}{1-PSR^N}PSR^{N-1} \qquad \text{(V.23)}$$

The PSR_{app} as a function of PSR is plotted for $N = 5$ in Figure V-18. Figure V-19 shows the measured PSR (apparent: open circles) and the corrected one (solid circles) by applying the previous correction. It results that the corrected PSR has values lying between 0.8 and 1, and that minimum value is not in contradiction with the presented theory (Stankov model). It is noteworthy that the general behavior of PSR is conserved.

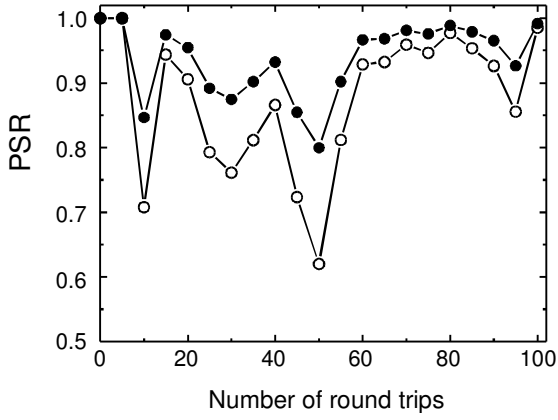

Figure V-19: Measured PSR (open circles) and the corrected one (solid circles).

SECOND EXPERIMENTAL RESULTS[32]

The performances of the set-up had to be improved for allowing its practical use for pumping OPO systems. We adopt the previous setup schematized in Figure V-15, with a few changes: we use a smaller diameter Nd:YAG rod (6 mm), a more powerful intracavity AOML in order to improve the stability of the oscillator output and we rearrange the positions of the optical elements as shown in Figure V-20. The optimum performance of the oscillator is achieved by correctly balancing the antagonist actions of the amplifier, TPA and FDNLM. The onset of two-photon absorption in GaAs starts at a fluence of 55 MW/cm^2 while the maximum energy extraction is achieved by filling the Nd:YAG rod. These conditions are fulfilled by inserting the lenses L_1 and L_2 with focal lengths of 100 and –40 mm, respectively, in order to obtain a two-waist transversal mode in the laser cavity, as shown in Figure V-20. The laser head is placed as close as possible to L_1 in order to provide a mode occupying the maximum volume in the Nd:YAG rod.

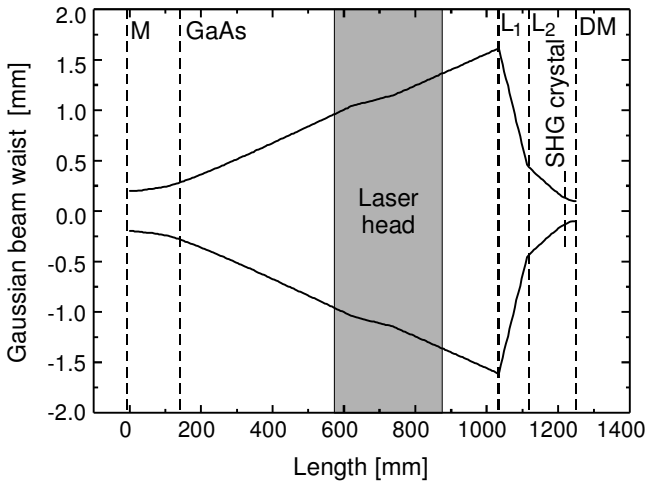

Figure V-20: Simulation of the laser cavity using paraxial Gaussian beam propagation. This calculation takes into account the optical-element positions, the refractive index, and the thermal lensing into the laser rod (about 6 m). The beam profile shows a two-waist mode, which provides the necessary beam fluence on the SHG crystal and on the GaAs platelet. The acronyms are described in text.

Among the different crystal lengths ranging from 1 to 7 mm, and the different reflectivity of the output coupler, we observe the best performances of the oscillator when using a BBO crystal thickness of 3 mm and choosing a dichroic mirror with the following characteristics: $R_{\omega} \sim 25\%$ at 1064 nm and $R_{2\omega} > 99\%$ at 532 nm.

Figure V-21 shows the influence of the crystal length on the pulsewidth and mode-locking stability. We did not notice a passive mode locking with a crystal of 1.8 mm. Optimum mode locking and pulsewidth were observed for a crystal of about 3 mm. Thicker crystals have shown a stable mode locking and a larger pulsewidth, up to 26 ps for a 5 mm thick crystal.

In addition, we show the effect of the crystal-DM separation on the mode locking on Figure V-22. We noticed a good mode locking in the range from 22 to 44 mm and an optimum pulsewidth around a distance of 40 mm from the DM. An unstable operation was observed outside that range.

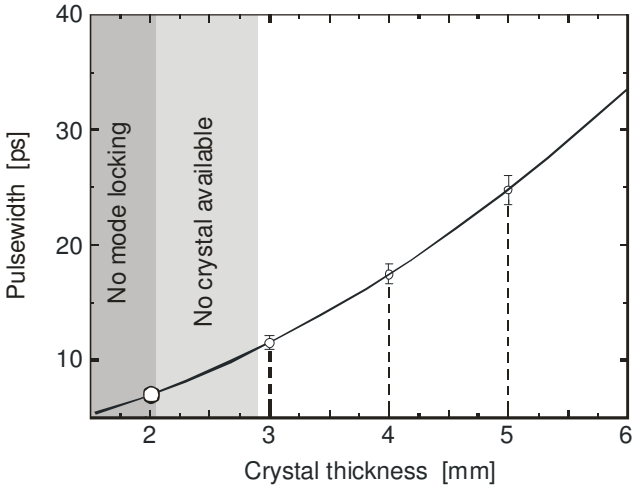

Figure V-21: Pulsewidths measured for various crystal thicknesses. The hatched region shows no mode locking (we used a 1.8-mm crystal).

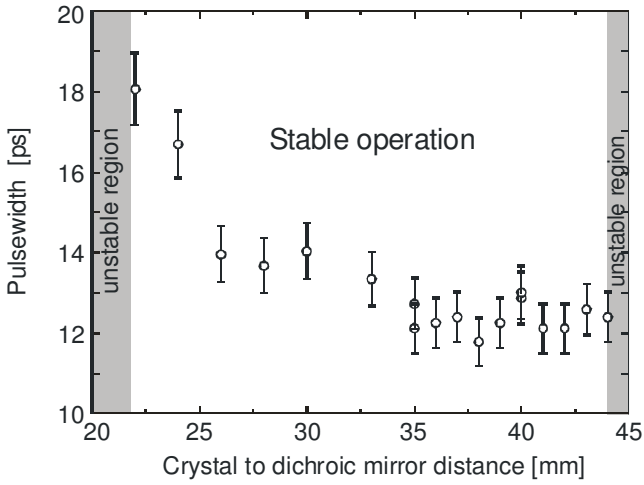

Figure V-22: Operation of the FDNLM for different distances between the crystal and the dichroic mirror. The dashed regions designate an unstable operation.

Taking all these factors into consideration, a stable laser operation is observed at about 10 J of electric pump energy of Nd:YAG head. A pulse train of about 160 pulses is generated at 25 Hz. The envelope of the bunch, as measured by a fast photodiode and recorded using a 60-MHz bandwidth oscilloscope, is shown in Figure V-23.

The pulse-train envelope can be decomposed in three parts. The first one (part i on Figure V-23-a) is characterized by fast variation of the pulse energy as well as by a pulse shortening from a few hundred ps, as imposed by the active mode locker (AOML), to a few tens of ps as a result of the action of the FDNLM. The second part (part ii) is characterized by a stable pulse energy and a duration of 12.5 ps. This stability is a result of the antagonist actions of the nonlinear absorption in the GaAs platelet, which sets a limit to the pulse peak power, and the FDNLM that tends to shorten the pulse length. Fine-tuning of the lens (L_2) position in the cavity enables to balance properly the action of these two elements for optimizing the performances. The depletion of the energy stored in the YAG rod entails the decrease of pulse energy, as shown in part iii on Figure V-23-a.

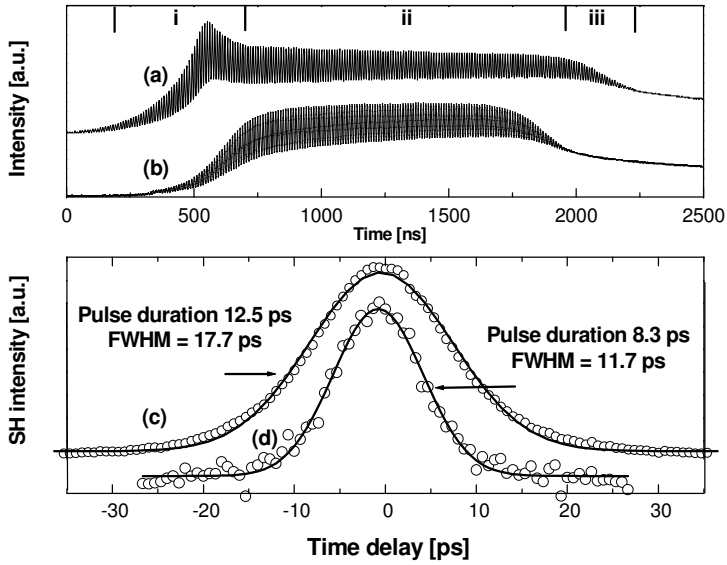

Figure V-23: Performances of the Nd:YAG laser pump beam. Curves a and b: Pulse-train envelope before and after the extracavity acousto-optic modulator (AOM). Curves c and d: background-free 2nd order autocorrelation trace of the 1064 nm pulses after the AOM, measured at the middle and at the end of the pulse train (curve a), respectively: Open circles: experimental data points. Solid line: Least square fit to the autocorrelation of a Gaussian fundamental pulse.

In this latter regime, the TPA action stops, and a pulse duration as short as eight ps is measured at the end of the pulse train (Figure V-23-d). This demonstrates the fact that a Fourier-transform-limited pulse of the Nd:YAG material gain bandwidth can be obtained with such an oscillator. For synchronous pumping of OPO, the first part of the train is cut away using an extracavity photo-acoustic modulator (AOM). The resulting train envelope, shown in Figure V-23-b, corresponds to about 100 pulses as short as 12.5 picoseconds with 10 μJ per pulse. This represents a drastic improvement in comparison to the train of about 20 pulses, with average energy of ~1 μJ, demonstrated in our previous work.

The latest experimental results show that pulsewidths down to eight ps could be obtained over the entire pulse train as shown in Figure V-24.

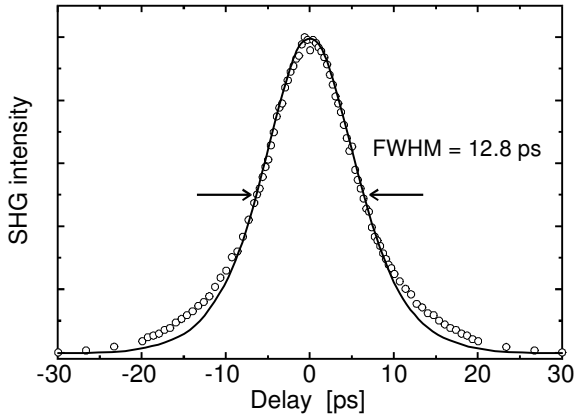

Figure V-24: Background-free second-harmonic autocorrelation measurement over the entire pulse train. The fit to a hyperbolic-secant curve* (continuous line) gives a FWHM equal to 12.8 ps, corresponding to fundamental pulse duration of 8.3 ps.

The fit to a hyperbolic-secant curve (the continuous line) gives a FWHM equal to 12.8 ps, corresponding to fundamental pulse duration of 8.3 ps. This performance has been obtained with a very careful adjustment of the FDNLM parameters (e.g. the telescope distance, the air space between the crystal and the dichroic mirror, and the diameter of the intracavity aperture).

Conclusion

In this chapter, we started by presenting the basic theory of the passive mode locking using a FDNLM. We worked out in detail several figures of merit in order to optimize the reflection coefficient of the dichroic mirror and the thickness of the SHG crystal. On this basis, we constructed a setup that demonstrated the generation of optical pulses as short as 12 ps, in keeping with the predictions of the Barr model. In a second step, we worked on the configuration of all the optical elements of the cavity and found out that the position of the laser head was critical for obtaining the best performances, i.e. a train of more than 100 homogeneous optical pulses, with energy of 10 μJ and duration of 12 ps. An exceptional duration of eight ps has been demonstrated over the whole pulse train. Further improvement can be

* In chapter VI, we show a better fit of the autocorrelation curves using a group of Gaussian pulses.

expected with shorter crystals (between 2.5 and 3 mm) and with a curved DM to tightly focus the beam at the crystal position.

Chapter VI Optical Parametric Process for Generating Near- and Mid-Infrared Optical Pulses

In this chapter, we shall describe the experimental setup of a mid-infrared optical parametric oscillator based on $LiNbO_3$ and $AgGaS_2$ crystals, which provides tunability from 2.5 to 4 μm and from 5 to 10 μm, respectively.

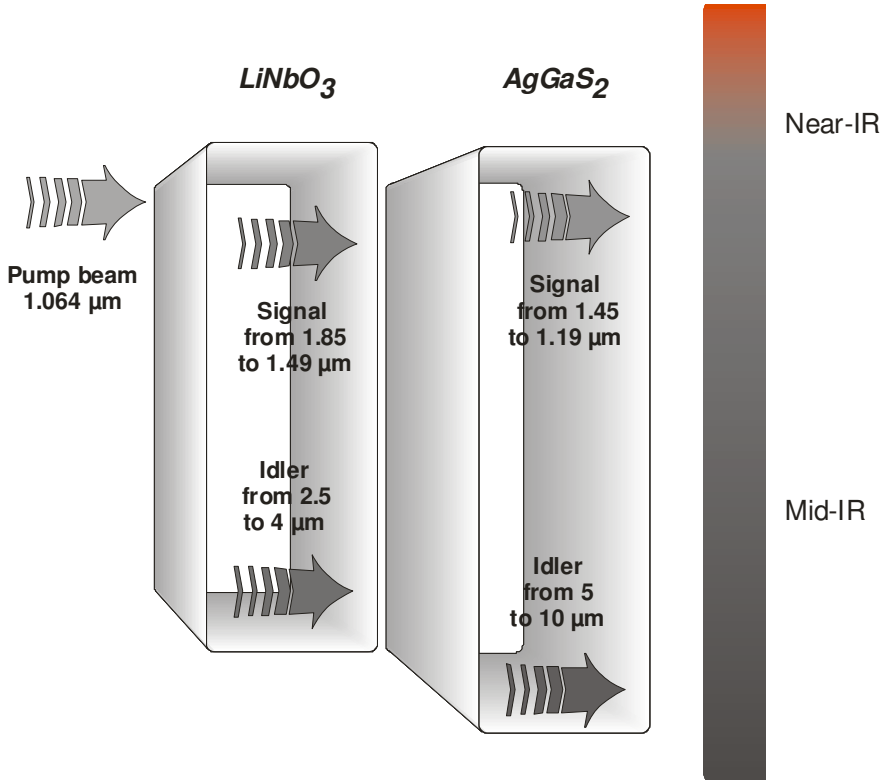

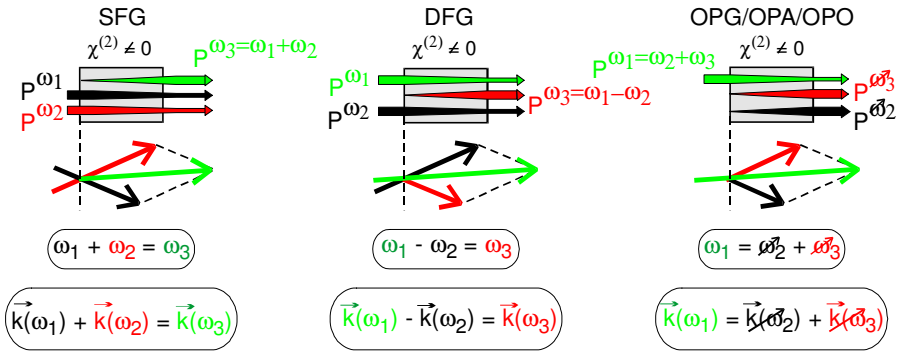

Figure VI-1: Three-wave interactions and the corresponding phase-matching conditions into the nonlinear medium with non-vanishing second-order susceptibility.

The second-order nonlinear processes occurring inside transparent crystals for the interacting waves represent powerful tools for generating, amplifying, and mixing frequencies in the optical spectrum range, which lies from the far infrared to the ultraviolet. The general optical scheme of three-wave interactions into the second-order nonlinear crystal is illustrated on Figure VI-1.

We can classify the principal interactions between three optical waves in the nonlinear medium into three classes:

1. The *sum-frequency generation* (SFG) of the incident waves. Such a process that permits to get, at the output, a frequency higher than the input frequency, is also called up-conversion process.
2. The *difference-frequency generation* (DFG) of the incident waves. As the output frequency is lower than the input frequencies, the process is called a down-conversion process.
3. The third interaction results from the first one with the exception that the generated optical fields grow from the optical quantum noise and are amplified in the presence of the same SFG phase matching between the interacting waves. In other words, we have only one incident beam and the two other beams are generated with frequencies determined by the phase-matching condition in the nonlinear crystal. In practice, we call the incident beam the pump beam and the generated beams the signal beam (for the higher frequency) and the idler beam (for the lower frequency).

This optical process is called an optical parametric process, which in turn takes three different names like generation, amplification, and oscillation in order to distinguish the physical situations as follows: *Optical parametric generator* (OPG) when the signal and the idler beams are generated in the nonlinear crystal, *optical parametric amplifier* (OPA) when they are present on the input side of the crystal. Finally optical parametric oscillator (OPO) when, at least, one of them is oscillating. In this latter case, the OPO is called singly resonant, doubly resonant or triply resonant OPO to identify the number of oscillating waves one, two or the three of them (signal, idler and pump waves), respectively. These parametric processes are very important tools for tuning the optical frequency of a laser beam. As the parametric process splits an incident photon into two photons with lower energies, we can say that the parametric process is a down-conversion process. This point is very important because by using the Nd:YAG wavelength (1064 nm), one can generate any longer wavelength, which means any wavelength in the mid- and far infrared, using the appropriate optical materials (see the front page figure of this chapter).

Physical properties of lithium niobate ($LiNbO_3$)

The lithium niobate ($LiNbO_3$) crystal has good optical properties that make it the most reliable crystal for tuning the Nd:YAG wavelength in the near-infrared spectral region in one single conversion stage. This material is nonhygroscopic and hard, is a uniaxial crystal, belongs to the 3*m* trigonal point group, and has a large nonlinear coefficient relative to KDP. Its optical properties are shown in Table VI-1. The crystals of $LiNbO_3$ are transparent in the region from 0.42 to 4.2 μm. Phase matching can be achieved at 90° from the optical axis by rotating the crystal or by varying its temperature because its birefringence is temperature sensitive.

TRANSMITTANCE

The $LiNbO_3$ crystal shows good transmittance in the range from 0.47 up to 5.5 μm.[33] The transmission spectrum is plotted from 120 to 3300 nm in Figure VI-2. A high absorption is present at 2827 nm, due to the presence of OH in the crystal.

$LiNbO_3$		
Transparency range [μm]	0.4 – 5.5	
Type	Negative uniaxial	
Point group	3*m*	
Sellmeier coefficients*	n_o	n_e
A	4.91300	4.57906
B	0.118717	0.099318
C	0.045932	0.042286
D	0	0
E	0	0
J	0.0278	0.0224
Pump beam power [mW]	350-400 at 12 ps with 2 mm diameter	
Interaction type	e → o + o	
Effective nonlinear coefficient d_{eff}	$d_{13}\sin\theta - d_{22}\cos\theta\sin 3\varphi$	
Nonlinear coefficients [pm/V]	d_{22} = 2.46 ± 0.23 d_{31} = -4.64 ± 0.66 at 1055 nm	

Table VI-1: Optical properties of $LiNbO_3$.

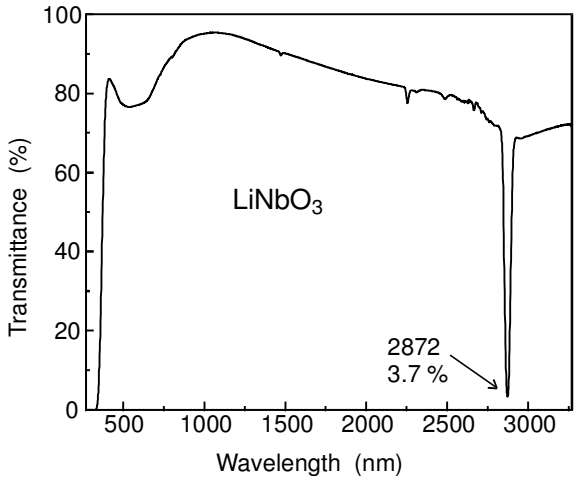

Figure VI-2: Transmittance curve of $LiNbO_3$ of 20-mm thickness. This curve shows a good transmittance from 420 to more than 3300 nm. At 2872 nm, the crystal shows a strong absorption.

* The Sellmeier dispersion relation is given by $n^2(\lambda) = A + B\lambda^2/(\lambda^2 - C) + D\lambda^2/(\lambda^2 - E) - J\lambda^2$.

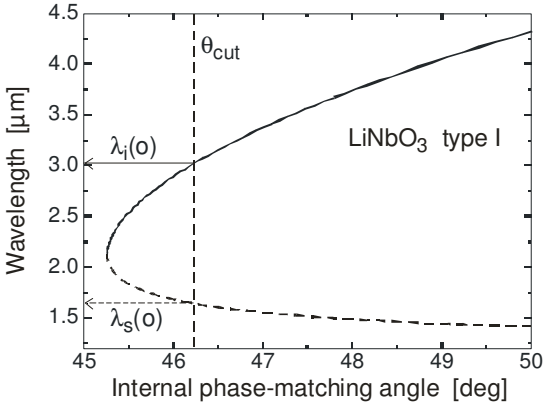

Figure VI-3: Tuning curve of type-I $LiNbO_3$ pumped by the Nd:YAG wavelength at 1.064 µm. The idler and the signal beams are represented by the solid and dashed lines, respectively.

PHASE-MATCHING ANGLES

The internal phase-matching angle is shown in Figure VI-3. These curves were obtained for the Nd:YAG wavelength as the pump beam. The solid curve shows the idler wavelength varying from 2.128 up to 4.3 µm when the signal wavelength (dashed curve) varies from 2.128 to 1.4 µm. In this case, the phase-matching angle varies from 45.25° to 50°. The idler and signal beams have ordinary polarization when the pump beam takes the extraordinary polarization. The cut of the crystal at 46° gives large tunability around 3-µm wavelength as shown on Figure VI-3.

Physical properties of silver-thiogallate crystal ($AgGaS_2$)

This crystal has good optical proprieties to be pumped by a Nd:YAG system and gives tunability up to 10 µm in one single conversion stage. It is a uniaxial crystal, belonging to the $\bar{4}2m$ point group. The crystals of $AgGaS_2$ are transparent in the region from 0.47 to 13 µm.

TRANSMITTANCE

The transmittance curve is shown in Figure VI-4 in the region from 0.5 to 3.3 µm, which covers the pump beam and the signal variation domain. A transmittance of about 90 % is obtained for the pump beam with an average of 60 % over the wavelength domain of the signal.

$AgGaS_2$		
Transparency range [μm]	0.47 – 13	
Type	Negative uniaxial	
Point group	$\bar{4}2m$	
Sellmeier coefficients	n_o	n_e
A	3.3970	3.5873
B	2.3982	1.9533
C	0.09311	0.11066
D	2.1640	2.3391
E	950.0	1030.7
J	0	0
Pump beam power [mW]	200-250 mW at 12ps with 2 mm diameter	
Interaction Type	e → o + o	
Effective nonlinear coefficient d_{eff}	$d_{36} \sin\theta \sin 2\varphi$	
Nonlinear coefficients [pm/V]	d_{36} = 11.1 ± 1.7 at 10.6 μm	

Table VI-2: Optical properties of $AgGaS_2$.

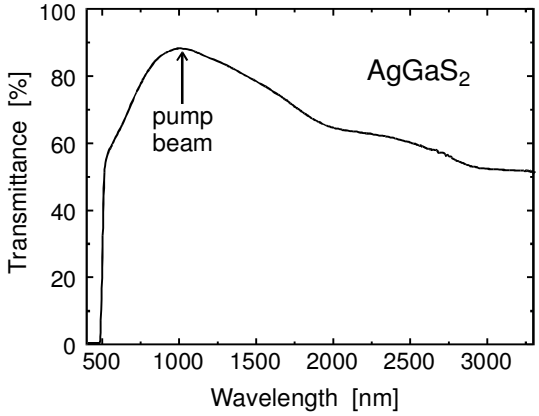

Figure VI-4: Transmittance curve of $AgGaS_2$ of 10 mm length.

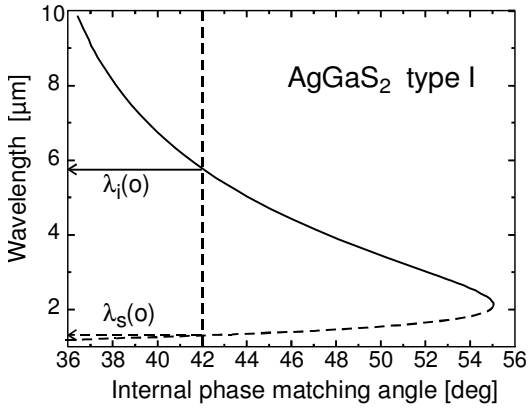

Figure VI-5: Tuning curve of type-I $AgGaS_2$ pumped by Nd:YAG wavelength 1.064 μm. The idler and the signal beams are represented by the solid and dashed lines, respectively.

PHASE-MATCHING ANGLE

The tuning curves are shown in Figure VI-5. These curves are calculated for a pump beam of 1.064 μm wavelength. The solid curve shows the idler wavelength varying from 2.128 up to 10.46 μm when the signal wavelength (dashed curve) varies from 2.128 to 1.18 μm. In this case, the phase-matching angle varies from 36° to 55°. The idler and signal beams have ordinary polarization when the pump beam takes the extraordinary polarization. The cut of the crystal at 42° gives large tunability around 5-μm wavelength as shown on Figure VI-5.

OPO based on $LiNbO_3$

The experimental setup of this OPO is illustrated on Figure VI-6.[32,34] The oscillator is followed by an optical isolator (OI) and a double-pass amplification stage in a Nd:YAG rod (9-mm diam. 115-mm long) pumped by flashlamp at 45 J. At 25Hz repetition rate, the output power at 1064 nm is ~1.2 W, corresponding to energy of 43 mJ per bunch and 430 μJ per pulse. About 30 % of the available output power is used for pumping the mid-infrared OPO. The remaining power (60 %) is dedicated to pump a visible OPO that will be described in the next chapter.

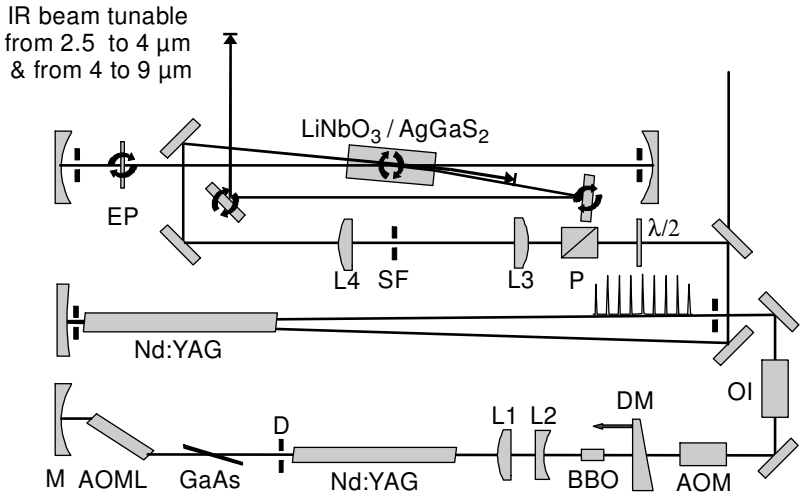

Figure VI-6: Scheme of a mid-infrared OPO based on $LiNbO_3$ or $AgGaS_2$. The crystals are pumped by a train of pulses generated and amplified by a Nd:YAG system.

The optical parametric oscillator is schematized in Figure VI-6. The combination of a half-wave plate ($\lambda/2$) and a Glan-Thompson polarizer (P) is used to adjust the pump-beam power. A telescope (L_3-L_4) adapts the beam spot diameter to about 2 mm (1/*e* intensity). One of the two nonlinear crystals, LiNbO3 ($8\times8\times20$ mm^3, cut for type-I difference-frequency generation, $\theta = 46.4°$) or $AgGaS_2$ ($10\times10\times10$ mm^3, cut for type-I difference-frequency generation, $\theta = 45°$) is then selected by using a translation stage. The crystals cover the spectral range from 2.6 µm to 4 µm and from 4 to 9 µm, respectively. The pumping of the nonlinear crystal is slightly noncolinear (the pump beam makes an angle of about 2° with the OPO cavity axis) meaning that the signal beam (1.2 to 1.85 µm) oscillates in the cavity while the idler beam (2.6 to 9 µm) is emitted out of the OPO cavity axis. The optical length of the cavity has to be adjusted to that of the Nd:YAG oscillator (1.5 m) to obtain synchronous pumping. The bandwidth of the gain in the non-linear crystals varies from 50 cm^{-1} to 10 cm^{-1}, depending on the crystal and wavelength. Therefore, an etalon plate (free spectral range of 30 cm^{-1} with a finesse of 15) is inserted in the OPO cavity to narrow the bandwidth of the signal beam. Multiple passes through the etalon result in a much smaller bandwidth for the signal beam.

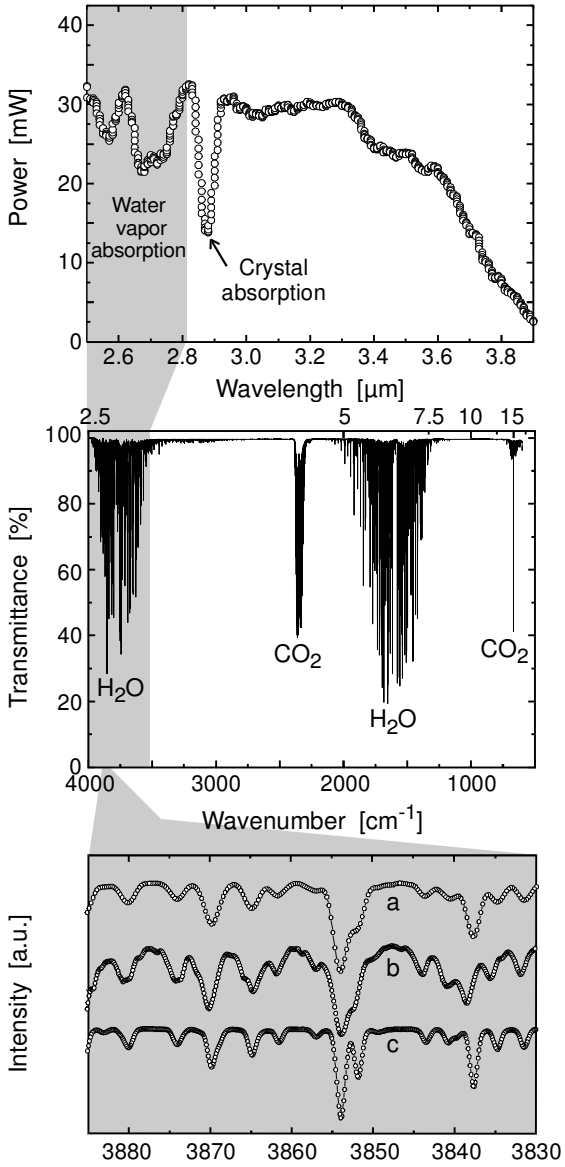

Figure VI-7: Upper panel: Idler power of $LiNbO_3$. Central panel: Air transmittance recorded in the mid-infrared spectral regions. Lower panel: The spectral resolution of the laser system is demonstrated by comparing the water vapor absorption spectra measured by FT-IR with 2 cm^{-1} (curve a) and 1 cm^{-1} (curve c) resolutions, with the power spectrum of the laser system after a 2-m path in air (curve b).

The bandwidth of the idler beam is slightly smaller than 2 cm^{-1}, independently of the wavelength from 2.6 to 9 μm, as demonstrated by the water-vapor absorption spectrum shown in Figure VI-7 (lower panel).

The pump power impinging the $LiNbO_3$ OPO is ~320 mW. The conversion efficiency at 3.4 μm is about 35%, corresponding to an output power of 38 mW. The pump power is reduced to 280 mW when pumping the $AgGaS_2$ crystal. The conversion efficiency at 5 μm is about 30 %, corresponding to an output power of 17 mW. Higher output powers could in principle be achieved by increasing the fraction of the pump power directed to mid-IR OPO. Finally, two rotating mirrors keep the pointing of the idler beam independent of wavelength despite the noncollinear pumping configuration. The rotations of the crystal, of the etalon, and of the two mirrors are computer controlled, as we shall see in chapter VIII.

The power spectrum is shown in Figure VI-7 (upper panel). The spectral region from 2.5 to 3 μm shows absorption bands due to the water vapor from the air. The transmittance through the air is recorded in Figure VI-7 (central panel). The crystal absorption introduces a power hole at 2.87 μm as can be expected from the transmittance (see Figure VI-2). We measured the power conversion efficiency in the crystal, by dividing the depleted power (i.e. the complementary part of the transmitted power after the crystal) by the total incident power (~ 355 mW). The power conversion efficiency reaches 45% around 3 μm as measured in Figure VI-8. The power conversion efficiency for the idler beam takes a value of about 20 % at 3 μm.

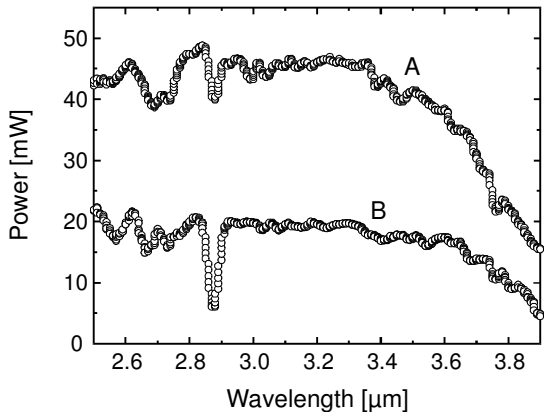

Figure VI-8: Power conversion efficiency of $LiNbO_3$ OPO for the depleted power (A) and for the generated Idler beam (B).

OPO based on $AgGaS_2$

We adopt the previous setup for $AgGaS_2$ OPO, as shown in Figure VI-6. The pump power is reduced to 280 mW. The conversion efficiency varies between 15 up to 30% corresponding to an output power range of 10 to 5 mW. Higher output powers could in principle be achieved by increasing the fraction of pump power directed to mid-IR OPO. We notice from Figure VI-9 that the power fluctuates a lot in this region due to the absorption in the air (see central panel in Figure VI-7), which makes it a major problem for generating these wavelengths.

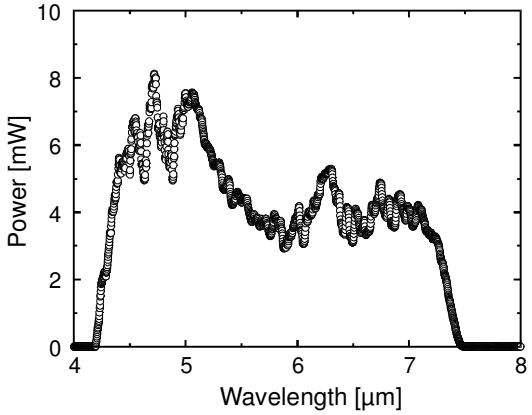

Figure VI-9: Power spectrum of the $AgGaS_2$ OPO.

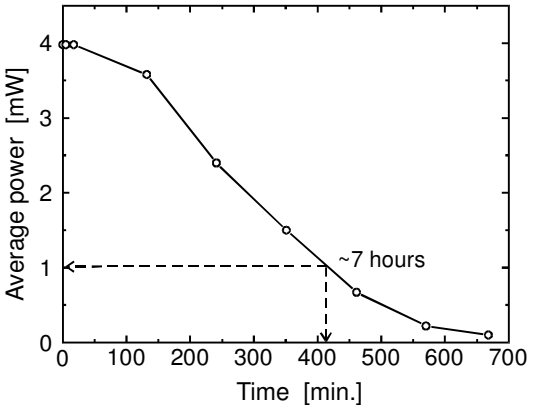

Figure VI-10: Average power of the $AgGaS_2$ OPO versus time. The average power is taken over the whole spectral range of the crystal for each point of measurement.

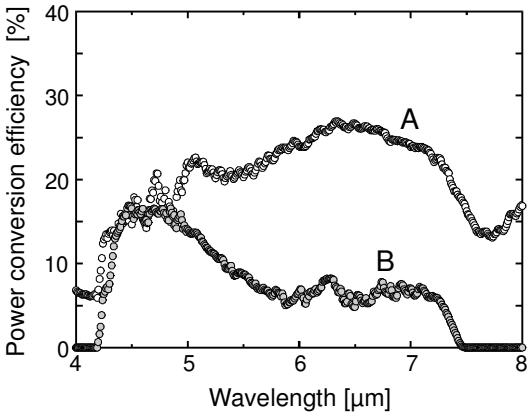

Figure VI-11: Power conversion efficiency of $AgGaS_2$ OPO for the depleted power (A) and for the generated Idler beam (B).

The $AgGaS_2$ has a very limited lifetime of the order of few hours of continuous use, as shown in Figure VI-10. The spectral resolution is ensured by the insertion of an appropriate etalon plate, like for $LiNbO_3$. Measuring the pump depletion after the crystal permits to deduce the total conversion efficiency for this process, which varies between 15 and 30 %. At the same time, the conversion efficiency of the used beam (idler) can be simply estimated at 10 to 15% by measuring the output power (Figure VI-11). These measurements are not the best performances obtained from this setup but we show them because we made a complete set of measurements at that time.

Conclusion

We realized two optical parametric oscillators by synchronously pumping of $LiNbO_3$ and $AgGaS_2$ crystals. We have demonstrated the tunability of the laser system from 2.5 to 10 µm with 2 cm^{-1} spectral resolution and 30 mW power.

In the next chapter, we shall describe a setup that extends the spectral range up to 20 µm.

Chapter VII Difference-Frequency Process for Generating Mid-Infrared Optical Pulses

In this chapter, we shall present a difference-frequency generation stage (DFG) based on a CdSe semiconductor crystal in combination with a KTP-OPO system, that enables tunability from 10 up to 20 µm.

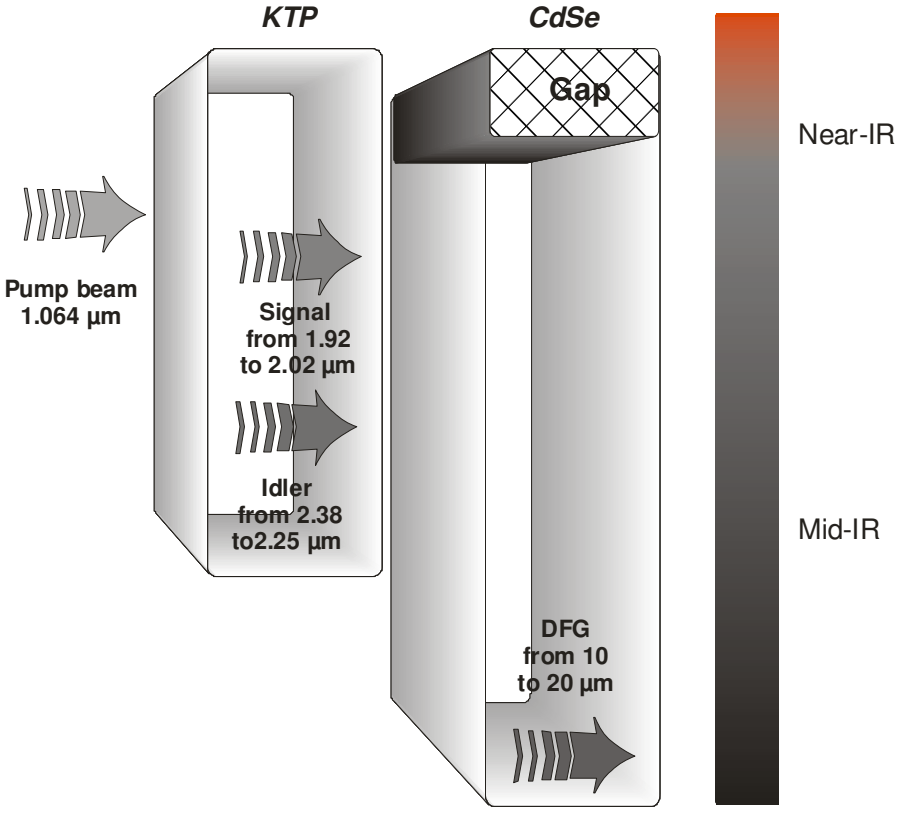

Physical properties of potassium titanyl phosphate crystal (KTP)

The $KTiOPO_4$ crystal (KTP) is a very attractive material for various sum- frequency and difference-frequency, and optical parametric applications over its entire transparency range from 0.35 to 3.2 μm. Figure VII-1 shows the overall transmittance of a KTP crystal of 15-mm length having an antireflection coating at a wavelength of 2.1 μm. It has large nonlinear coefficients, and the adequate birefringence in the YZ and the XZ planes allows phase matching for the more effective type-II process over a large wavelength range. The cut in the XZ plane is more advantageous due to the higher effective nonlinear coefficient presented by the equations

$$\begin{aligned} d_{ooe} &= d_{32}\sin\theta \quad \text{in XZ plane} \\ d_{ooe} &= d_{31}\sin\theta \quad \text{in YZ plane} \end{aligned} \tag{VII.1}$$

where d_{31} = 1.4 pm/V and d_{32} = 2.65 pm/V (see ref. 33). These equations are plotted in Figure VII-2. A factor of 4 is obtained between the XZ and YZ cuts. Because it has wide acceptance angles, relatively good thermal properties, and a high damage threshold, KTP is the best nonlinear material for Nd lasers. The major drawback is the difficulty of growing large crystals.

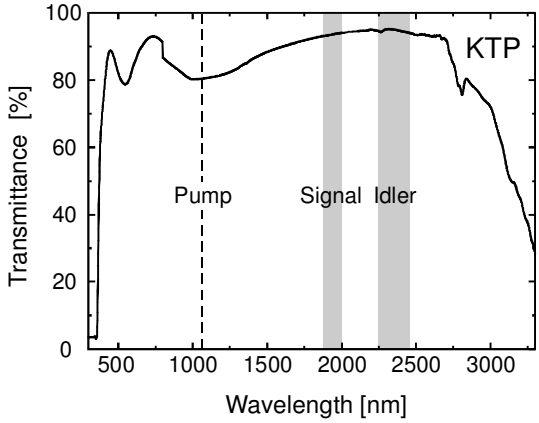

Figure VII-1: The transmittance of KTP crystal of 15-mm thickness. The crystal is antireflection coated at 2.1 μm wavelength.

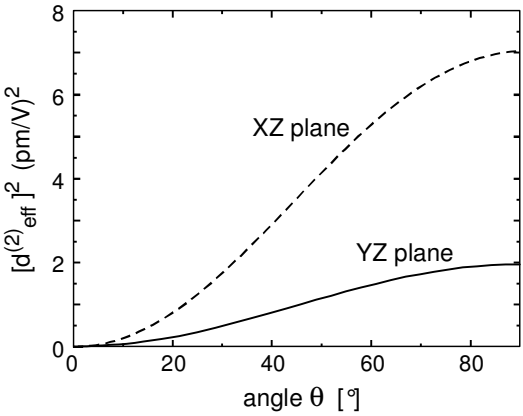

Figure VII-2: Variation of the square of the effective nonlinear coefficient in both YZ and XZ planes for a KTP crystal.

KTP (XZ plane)			
Transparency range [μm]	0.35 – 4.5		
Type	Positive biaxial		
Point group	*mm*2		
Sellmeier coefficients	$\boldsymbol{n_x}$	$\boldsymbol{n_y}$	$\boldsymbol{n_z}$
A	3.0065	3.0333	3.3134
B	0.03901	0.04154	0.05694
C	0.04251	0.04547	0.05658
D	0	0	0
E	0	0	0
J	0.01327	0.01408	0.01682
Pump beam power [mW]	700		
Interaction Type	o → o + e		
Effective nonlinear coefficient d_{eff}	$d_{32} \sin\theta$		
Nonlinear coefficients [pm/V]	d_{32} = 2.65 at 1064 nm		

Table VII-1: Optical properties of a KTP crystal with the optical axis is in the XZ plane.

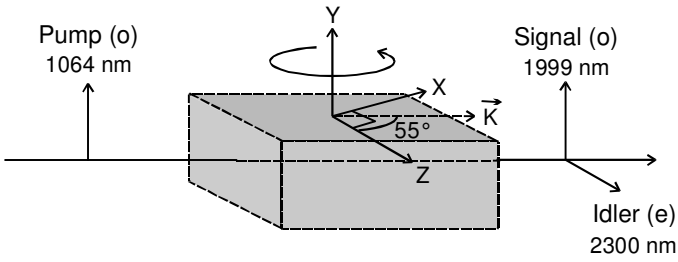

Figure VII-3: Orientation of KTP crystal in order to have type-II interaction.

KTP decomposes on melting (~1500°C). Hence, normal melt processes cannot be used to grow this material. However, single crystals of KTP can be grown by both hydrothermal and flux techniques. Currently crystals up to 1 cm^3 are commercially available. KTP crystallizes in the orthorhombic point group. In our setup, we used a KTP crystal cut as depicted on Figure VII-3.

PHASE-MATCHING ANGLES

The calculated phase-matching angles are shown in Figure VII-4. Tuning the crystal near the point of degeneracy (2128 nm, 51.2°) will produce signal and idler with wavelengths close to each other in such a manner that the DFG wavelength lies between 10 and 22 μm, as shown by the dashed curve.

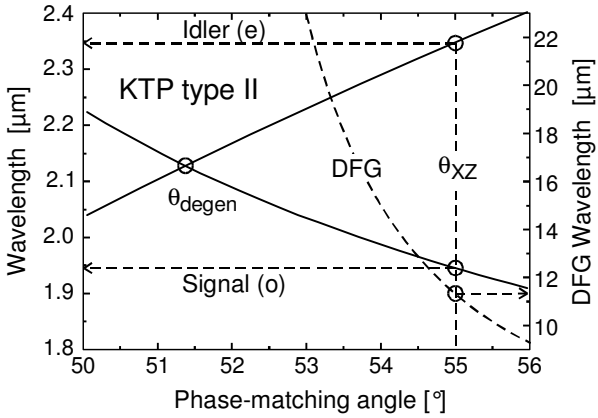

Figure VII-4: Phase-matching curves of type-II KTP crystal. The continuous curves indicate the tuning angle in the XZ plane. The dotted curve represents the DFG wavelength of the mixed signal and idler wavelengths.

In our case, the proposed cut angle is about 55°, which gives signal, idler, and DFG wavelengths of 1.94, 2.34 and 11.35 μm, respectively.

Cadmium selenide crystal (CdSe)

CdSe is a semiconductor crystal with an energy gap of 1.75 eV, which makes absorption for wavelengths shorter than 0.71 μm. The linear absorption in the gap energy spectral domain is shown in Figure VII-5. For high pump intensities, two-photon absorption (TPA) is observed for wavelengths shorter than 1.4 μm.[35,36] Absorption for a wavelength around 2 μm is observed in the case of tight focusing into the crystal. In our opinion, this is due to the presence of impurities in the energy gap as shown in Figure VII-5. The latter argument pushes us to avoid focusing into the crystal and to use a large beam diameter.

CdSe		
Transparency range [μm]	0.75 – 25	
Type	Positive uniaxial	
Energy Gap	1.75 eV	
Point group	6*mm*	
Sellmeier coefficients	n_o at 20°C	n_e at 20°C
A	4.2243	4.2009
B	1.7680	1.8875
C	0.2270	0.2171
D	3.1200	3.6461
E	3380	3629
J	0	0
Pump beam power [mW]	80 (signal + idler)	
Interaction type	o – e → o	
Effective nonlinear coefficient d_{eff}	$d_{31}\sin\theta$	
Nonlinear coefficients [pm/V]	d_{31} = -18 at 10.6 μm	

Table VII-2: Optical properties of the CdSe crystal.

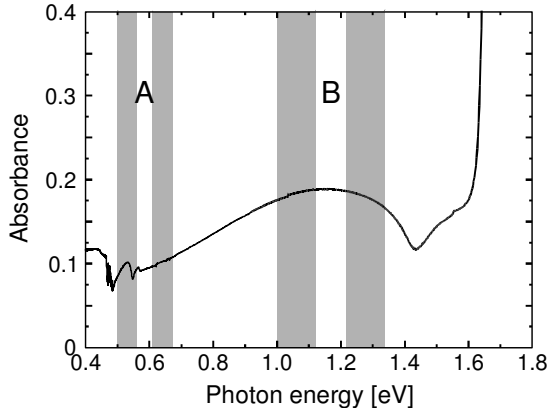

Figure VII-5: Absorbance of a 10 mm thick CdSe crystal, for photon energies lower than the energy gap. The band A represents the linear absorption for idler and signal photons while the possible TPA absorption is represented by the energy band B.

PHASE-MATCHING ANGLES

Figure VII-6 presents the internal phase-matching angle for type-II wave mixing inside CdSe. The phase-matching angle varies from 64° to 80°, which gives tuning from 10 to 22 μm. A cut angle around 70° can make tuning easy. As shown in Figure VII-6, a cut angle of about 76° gives better operation of this crystal around 10 μm, which is of some importance for spectroscopic applications.

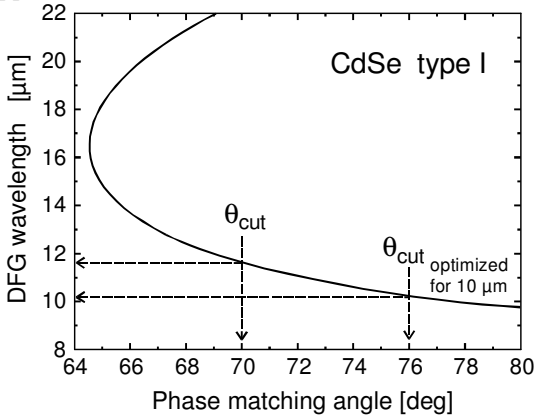

Figure VII-6: Phase-matching angle for DFG mixing inside CdSe of type II. The crystal is cut at 70°. A 76° cut is proposed to optimize operation around 10 μm.

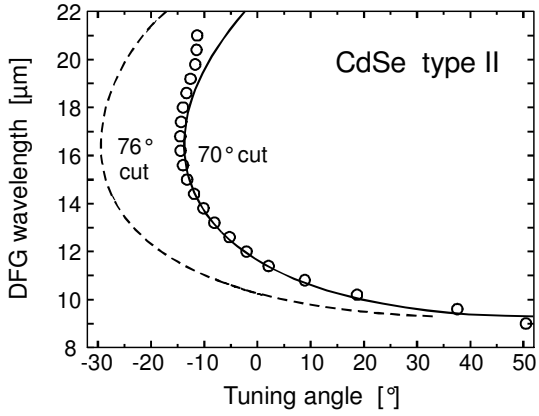

Figure VII-7: Tuning angle of the CdSe crystal. The solid curve shows the rotation angle with respect to the normal of the front surface. The dashed curve represents the calculated tuning angle if the crystal is cut at 76°.

The corresponding external phase-matching angle is plotted in Figure VII-7. The experimental data (open circles) show good agreement between the measured CdSe phase-matching curve and the calculations (solid line) using the Sellmeier coefficients of Table VII-2. The theoretical assumption of beam colinearity accounts for the departure of the calculation from the experiment.

DFG experimental setup[37]

The extension of the laser beam to longest wavelengths (from 10 to 21 µm) is difficult with one single conversion stage. A good alternative is to use difference-frequency generation into a nonlinear crystal with the adequate transmittance and phase-matching condition for this wavelength range. Nonlinear optical materials like semiconductor crystals (CdSe, $AgGaSe_2$ and GaSe) are known candidates for that purpose.[38,39,40,41]

The drawback of this kind of semiconductor crystals is the nonlinear absorption in the bulk of the crystal that limits the incident intensity and limits the conversion efficiency. In our setup, as shown in Figure VII-8, we selected a CdSe crystal because of its demonstrated ability to reach the longest wavelength of 22 µm.[38] The tandem KTP/CdSe OPO, depicted in Figure VII-8 relies on the two-step conversion process proposed in Ref. 38.

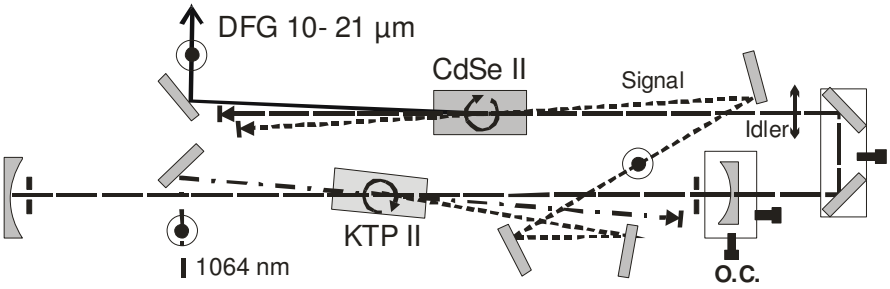

Figure VII-8: KTP OPO followed by a DFG stage in CdSe. Dashed, dotted line: pump beam at 1064 nm (vertical polarization), dashed line: KTP-OPO idler beam (2.23 to 2.46 µm), dotted line: KTP-OPO signal beam (1.87 to 2.03 µm), continuous line: DFG beam (10 to 21 µm).

The first stage consists of a synchronously pumped OPO built around a KTP crystal cut for type-II phase matching and optimized for the SFG process: 1064nm → 1987 nm + 2290 nm $o \rightarrow o + e$). The crystal cut angle (θ = 55°, ϕ = 0°, surface normal in the XZ-plane) differs from the one used in ref. 38 (θ= 47°, ϕ = 90, surface normal in the YZ-plane). The cut angle chosen in this work presents the advantages of a larger nonlinear effective coefficient (see Figure VII-2) and of the parallelism between the KTP and CdSe crystal rotation axes. The crystal rotation axes are set vertical to keep all the beam wavevectors in one plane parallel to the optical table, as shown in Figure VII-8.

The KTP crystal (5×5×15 mm^3) is placed in an OPO cavity formed by a gold mirror and an output coupler dielectric mirror with radius of curvature of R = -5 m acting as the output coupler reflection near 2.3 µm is about 70 percent enabling the oscillation of the idler beam (λ =2.23 to 2.45 µm) when the cavity length (approximately 1.5 m) matches properly the repetition rate (100 MHz) of the pulses. The slightly noncolinear pumping configuration allows for emission of the signal beam (λ =1.87 to 2.03 µm) out of the OPO cavity axis. For a pump beam diameter of ~1.6 mm (peak irradiance = 1.5 GW/cm^2) in the KTP crystal, we measured an idler beam power of about 90 mW corresponding to a conversion efficiency of ~ 20 %. The type-II phase matching of KTP ensures a limited bandwidth of 1.6 cm^{-1} for the generated idler and signal beams.

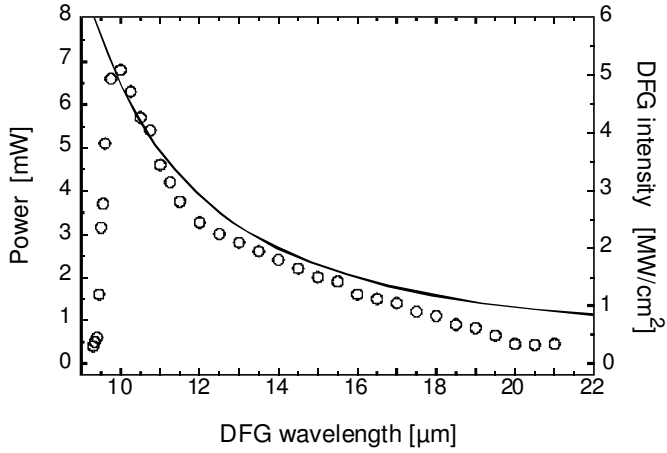

Figure VII-9: The output power described versus wavelength. The circles and the solid lines represent the experimental data and the corresponding theoretical values, respectively. The estimated peak intensity is shown on the right side scale.

The OPO signal and idler beams from the KTP crystal overlap in space and in time in the CdSe crystal (cut for type-II phase matching, θ = 70°, 10W×5H×15L mm^3).

The peak irradiances of the signal and the idler beams on the CdSe are approx. 150 MW/cm^2 and 75 MW/cm^2, respectively. They are close to the values determined in Ref. 38. Indeed, 50% depletion of the signal beam (λ =1.94 μm) is observed upon optimization of the DFG stage at 11 μm, indicating the adequacy of the irradiance obtained without inserting any telescope between the two conversion steps. The power spectrum of the DFG stage output is presented in Figure VII-9. The power at 15 μm approaches 2 mW, making this laser system adequate for SFG spectroscopy. The DFG output power is compared to the theoretical evaluation of the DFG process efficiency given by:[41]

$$I_{DFG} = I_i \frac{\lambda_i}{\lambda_{DFG}} \sinh^2(C\,L) \quad \text{with} \quad C^2 = \frac{74.36\, {d_{eff}}^2(\theta)\, I_s}{\lambda_{DFG}\ \lambda_i\ n_{DFG}\ n_i\ n_s}, \tag{VII.2}$$

where the subscripts *s*, *i,* and DFG refer to the signal, idler and DFG beams, respectively. *I*, λ, and *n* are the beam intensity, wavelength and corresponding refractive index, respectively. *L* is the crystal length.

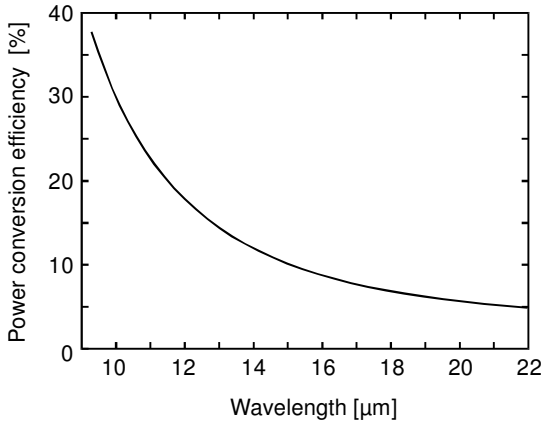

Figure VII-10: Power conversion efficiency of DFG stage using a CdSe crystal.

Figure VII-9 compares the conversion efficiency predicted by assuming a beam diameter of 2.5 mm, and taking account of the angular dependence of the effective nonlinear coefficient (e.g. d_{eff} = 18 sinθ pm/V) and of the 17% reflection loss at the crystal surfaces for the DFG beam. Departure of the experimental power curve from theory at wavelengths below 9.5 μm results from the excessive tilt angle of CdSe. The good correspondence between the experimental data and the theoretical predictions enables the association of the decrease in conversion efficiency at the longest wavelengths to the decrease of the DFG frequency. This indicates that the output power can possibly be enhanced in that spectral range if the beam diameter in CdSe is reduced. Figure VII-7 also shows that the tunability around 10 μm can be extended to 9 μm if the cut angle of the CdSe crystal is adjusted to about 76°, without jeopardizing the operation of the OPO near 20 μm.

Conclusion

We described a DFG setup based on a KTP optical parametric oscillator and a CdSe crystal. This tandem enables to perform laser operation over the spectral range from 10 to 20 μm, with a resolution of about two cm^{-1} and a delivering a few milliwatts, which is suitable for spectroscopic applications, as it will be shown in chapter IX.

Chapter VIII Optical Parametric Process for Generating Visible Optical Pulses

Tuning the Nd:YAG output laser beam in the visible spectral range is impossible by using only one nonlinear conversion stage: two or more stages are needed. In our experimental setup, we adopt three conversion steps, as shown schematically in the front-page figure of this chapter. In order to get a laser beam tunable from 420 to 720 nm, which covers the entire visible spectrum range, two conversion steps are needed to obtain the third harmonic of the Nd:YAG wavelength i.e. 355 nm in the ultraviolet domain. The latter beam is used to pump an OPO adapted to generate an optical beam in the visible spectrum range.

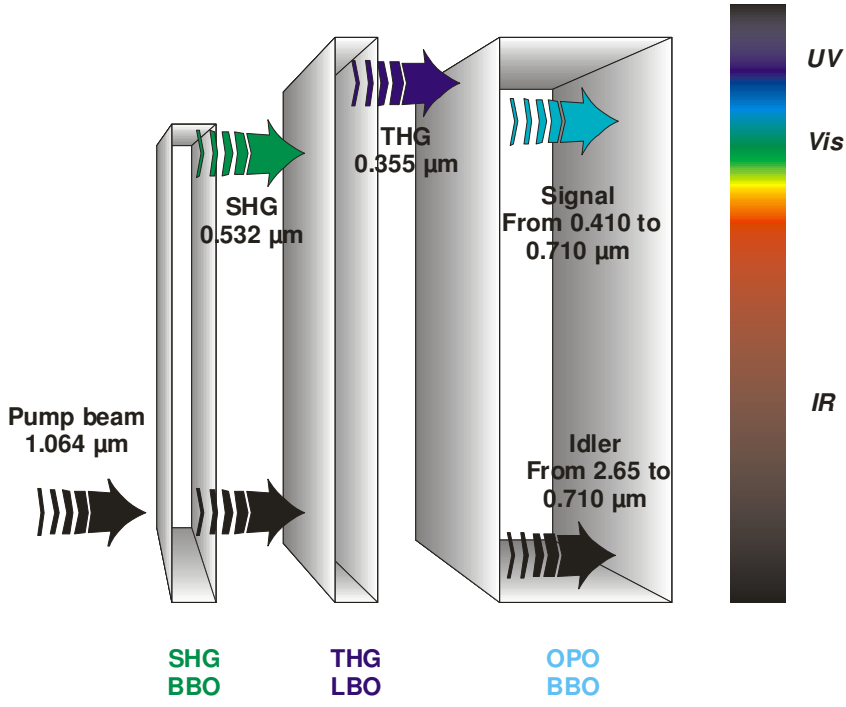

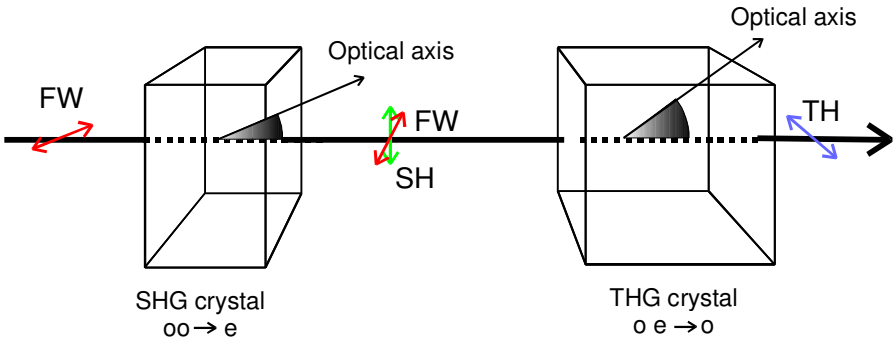

Figure VIII-1: Third-harmonic generation in two conversion steps.

Generation of the third harmonic of the Nd:YAG wavelength

The generation of the second and third harmonics of the Nd:YAG laser is a well-known method for obtaining visible light. Many configurations can be used. We limit the discussion to our setup, which consists of a BBO crystal of type I to generate the second harmonic and a LBO crystal of type II to produce the third harmonic, as shown on Figure VIII-1.

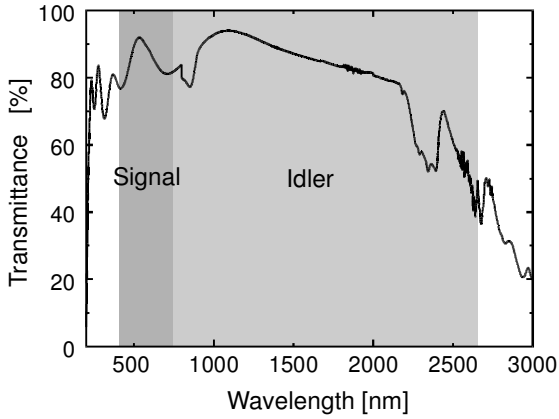

Figure VIII-2: Transmittance of 4-mm thick BBO crystal. The antireflection coatings for 532 and 1064 nm alter the transmittance in the visible spectral region.

BETA-BARIUM BORATE CRYSTAL (BBO)

Some characteristics of β-BBO were described in chapter V where this nonlinear crystal was used in a FDNLM setup for achieving passive mode locking of the Nd:YAG laser. We shall focus here on its tuning ability for frequency conversion in a spectral range extending from the ultraviolet to the mid-infrared (see Figure VIII-2). This material has a moderately large nonlinear coefficient, a large temperature tolerance, a low absorption and a very high damage threshold as noted in Table VIII-1. The principal shortcoming of BBO is a low angular tolerance, which is about 0.5 mr a cm. The BBO crystal is of particular interest for frequency doubling into the blue region because its transmission band extends to 200 nm in the UV, so that single or multiphoton absorption is not a problem with this material.

β-BBO		
Transparency range [μm]	0.189 – 3.5	
Type	Negative uniaxial	
Point group	$3m$	
Phase-matching angle of type I for SHG	$\theta = 22.8°$	
Sellmeier coefficients	n_o	n_e
A	2.7359	2.3753
B	0.01878	0.01224
C	0.01822	0.01667
D	0	0
E	0	0
J	0.01354	0.01516
UV Pump beam power [mW]	140 mW with 2 mm diameter	
Interaction type for OPO	$e \rightarrow e + o$	
Effective nonlinear coefficient χ_{eff}	$\chi_{13} \sin\theta - \chi_{22} \cos\theta \sin 3\phi$	
Nonlinear coefficients [pm/V]	$\chi_{22} = \pm 2 \times 2.3$ $\chi_{31} = \pm 2 \times 0.16$ at 1064 nm	

Table VIII-1: Optical properties of β-BBO.

PHASE-MATCHING ANGLE FOR VISIBLE OPO

Many works have shown the efficient tunability of BBO of type-I or type-II over the visible spectral region. In our setup we used the BBO of type-II interaction pumped by the third harmonic of Nd:YAG, which is at 355 nm. Figure VIII-3 presents the phase-matching angle for the signal wave, varying from 410 up to 740 nm (solid curve) and the idler wave, varying from 2.65 down to 0.682 μm and passing through 710 nm point, which corresponds to the degeneracy wavelength. The latter spectral variations are obtained for phase-matching angles varying from 25° to 50°. In this case, it is convenient to cut the crystal at an angle of 37°, which lies between the optical axis and the normal to the crystal surface. From Figure VIII-3, one can deduce that at normal incidence the signal wavelength is 514 nm and that the idler will take the complementary wavelength at 1.15 μm, as shown by the horizontal dotted lines.

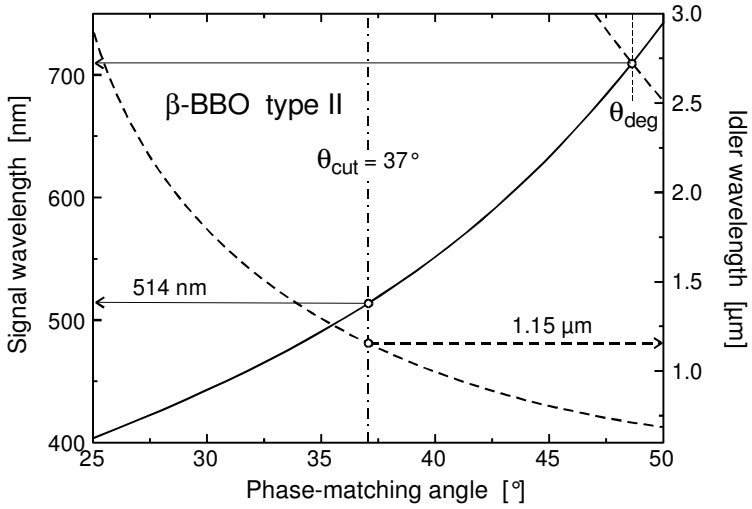

Figure VIII-3: Tuning curves of type-II BBO crystal. The solid curve represents the signal wavelength that varies in the visible spectrum region (left hand scale) and crosses the idler wavelength (dashed curve in the upper right corner) at the degeneracy point. The dashed curve below shows the idler wavelength in the infrared region (right-hand scale).

LITHIUM TRIBORATE (LBO)

LBO is also a newly developed nonlinear optical crystal characterized by a good UV transparency, a relatively high optical-damage threshold, and a moderate nonlinear optical coefficient. These properties, along with its mechanical hardness, chemical stability, and nonhygroscopicity, make LBO an attractive material for high-order harmonic generation. Because the birefringence in LBO is smaller than that in BBO, it tends to limit the phase-matching spectral range. However, it also leads to the possibility of noncritical phase-matching and larger acceptance angle for frequency-conversion applications in the visible and near-IR.

LBO (YZ plane, $\phi = 90°$)	
Transparency range [μm]	0.155 – 3.2
Type	Negative biaxial
Point group	*mm*2
Interaction type	***o*** (1064) + ***e*** (532) → ***o*** (355)
Phase-matching angle for THG	$\theta = 42.7°$
Effective nonlinear coefficient χ_{eff}	$\chi_{31}\cos\theta$
Nonlinear coefficients [pm/V]	χ_{31} = 2×0.67 pm/V at 1064 nm

Table VIII-2: Optical properties of a LBO crystal when the optical axis is in the YZ plane.

THG experimental results[42]

We investigate the maximum of the TH power in two ways: the first one is based on looking for the TH power when we have the maximum of SH power after the BBO crystal (Table VIII-3). The second method is to look for the maximum of TH power by changing the SH power around its maximum as shown in Table VIII-4. The maximum of THG power was found by using a BBO-I crystal of 2 mm thickness and a LBO-II crystal of 5 mm thickness as presented in Table VIII-4.

SHG crystal BBO-I	THG crystal LBO-II	Input power (FW) [mW]	Interm. power (SH) [mW]	Output power (TH) [mW]
1 mm	5 mm	500	85	20
2 mm	5 mm	550	200	205
4 mm	5 mm	550	190	220
4 mm	7 mm	550	190	N/A

Table VIII-3: Third-harmonic generation for maximum SHG after BBO crystal.

SHG crystal BBO-I	THG crystal LBO-II	Input power (FW) [mW]	Interm. power (SH) [mW]	Output power (TH) [mW]
1 mm	5 mm	500	N/A	20
2 mm	5 mm	550	180	250
4 mm	5 mm	550	140	190
4 mm	7 mm	550	175	185

Table VIII-4: Third-harmonic generation for the maximum THG.

The power conversion efficiency is defined by the expression[33]

$$\eta_{THG} = \frac{P_{3\omega}}{\sqrt{P'_{\omega} P_{2\omega}}}. \qquad \text{(VII.1)}$$

In our case, this gives a value of about 97% that does not completely reflect the physical limit. The physical limit of two-stage THG can be considered when we have annihilation of three photons of the FW to give one photon at the TH. This drives us to define the quantum conversion of two-stage THG as follows

$$\eta_{THG} = \frac{3N_{3\omega}}{N_{\omega}} = \frac{P_{3\omega}}{P_{\omega}}, \qquad \text{(VII.2)}$$

which gives a value of about 45 %. This means that 45 % of the pump beam is transformed into TH power, indicating a very good conversion process.

Tunable short pulses in the visible spectral range

The same configuration as for the IR-OPO is adopted to build the OPO in the visible spectral range, except that the pump beam is at the tripled frequency of the Nd:YAG fundamental wave beam. The third harmonic is obtained by two successive conversion steps. The first one is the frequency doubling by a SHG BBO crystal. The second step is the frequency tripling by mixing the FW and SH generated by the preceding step, into a THG LBO crystal, as we mentioned in the previous section. The generated TH is separated by a 60° quartz prism. A BBO crystal of 20 mm thickness, cut for type II interaction, is placed in the OPO cavity. The generated beam can be tuned from 410 to 2600 nm, covering thus the entire visible spectral region as shown in Figure VIII-3. The power spectrum is depicted on Figure VIII-5. For these data, the power output fluctuates around 11 mW whereas the pump beam power was about 140 mW. These fluctuations may be due either to the absorption of the idler beam in the air (see Figure VI-9), or to the crystal transmission (as shown in Figure VIII-2). The output power increases by about 100% when we remove the etalon plate from the OPO cavity. The power conversion efficiency is presented in the Figure VIII-6 (curve A). The latter curve shows efficiency as high as 40 %, although 50 % of this depletion is transformed into useful power, as shown by the curve B in Figure VIII-6. The pointing of the tunable laser beam is made independent on the output frequency by using two rotating mirrors, as illustrated in Figure VIII-4. The rotation of the crystals, of the etalon plates and of the pointing mirrors, is computer controlled, as will be described in the next chapter.

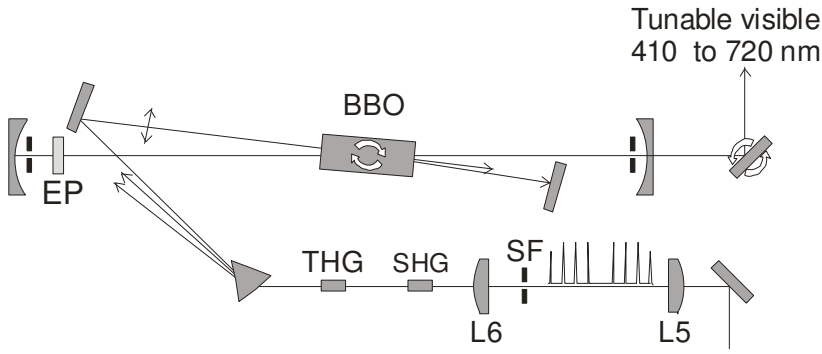

Figure VIII-4: Visible OPO based on BBO crystal of type I and pumped by the TH beam of Nd:YAG.

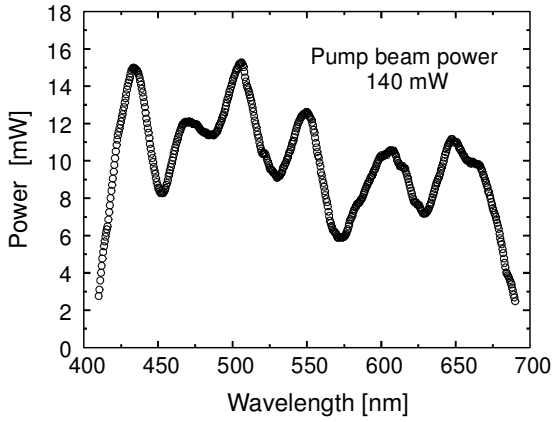

Figure VIII-5: Power spectrum of BBO-OPO output in the case of fine bandwidth.

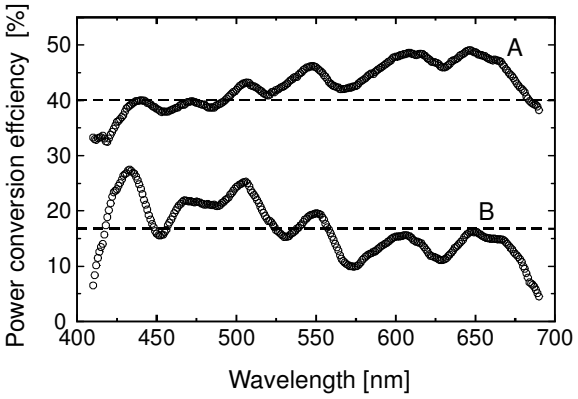

Figure VIII-6: Power conversion efficiencies for the depletion of the power pump beam (A) and for the signal power (B).

Conclusion

We built an optical parametric setup based on a BBO crystal pumped by the Nd:YAG third harmonic, which is obtained by the combination of BBO and LBO crystals for second and third harmonics generation, respectively. The average power was of the order of 10 mW, but can be improved by increasing the power of the pump beam. This shows an excellent power conversion efficiency of about 40%.

Chapter IX Sum-Frequency Spectrometer, Calibration and Functioning

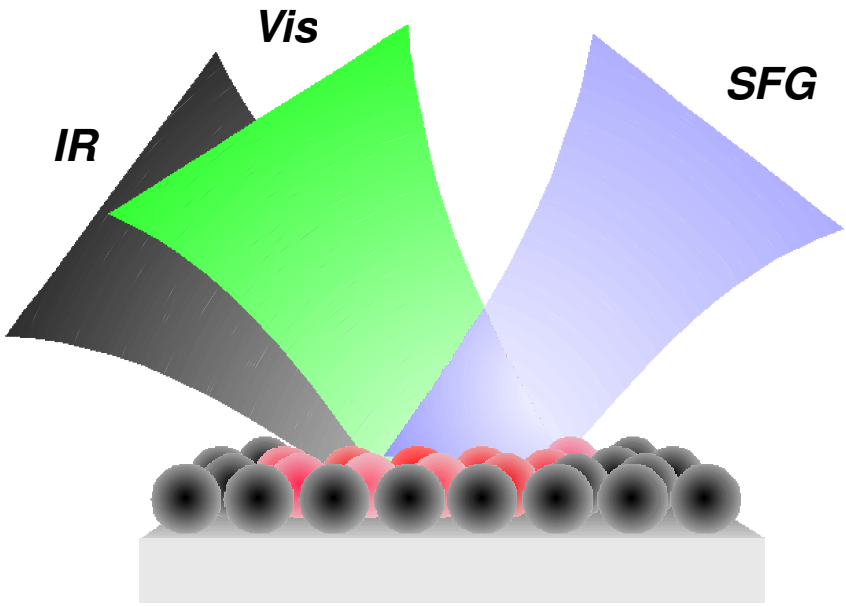

Since the first demonstration of SFG spectroscopy,[43] this vibrational technique has thriven in surface science. Based on a second-order nonlinear optical process forbidden in centrosymmetric media, SFG is intrinsically interface sensitive and has opened up new research fields by enabling vibrational spectroscopy of molecules at liquid/air interfaces,[44] at electrochemical interfaces in overpotential range,[45] or of adsorbed catalysts under low and high pressures.[46] All SFG studies using a tabletop laser were so far limited to the spectral range from 2.5 and 9 μm, with one record set at 11 μm.[47] This results from the difficulty of generating a tunable laser beam of picosecond duration and of adequate power at longer wavelengths. Although this range covers the vibrational fingerprint of important chemical groups such as OH, CH, and CO, extending SFG spectroscopy over the broad spectral range of molecular vibrations requires the use of a free electron laser.[45,48]

The general schematic view of the experimental setup is drawn in Figure IX-1. The configuration can be divided into six major parts. The first one is the optical oscillator that generates pulse train (about 100 pulses) at 25 Hz repetition rate. This oscillator, as we have already described, has been modelocked actively, by an AOML and passively, by a FDNLM in combination with a GaAs platelet (stage I). The pulse train is amplified by a double pass through a Nd:YAG amplifier head that provides around 1 W power for both IR and visible OPO (stage II). One third of the power is then directed into a beam reducer (L_3 and L_4) and into the IR OPO crystals (stage III). The extension module to 20 μm has already been described in chapter VI. The remainder of the amplified beam i.e. about two-thirds of it, is converted into TH for pumping the visible OPO crystal (stage IV). The two tunable beams generated by the IR and visible OPO are synchronized and slightly focused on the sample to be studied. A reference crystal, like ZnSe, is used to compensate the intensity fluctuations. The detection of the SFG signals is done by a dual beam monochromator (stage V), in such a manner that both beams are diffracted by two successive gratings before entering the photomultipliers. This detection system has the advantages of high sensitivity, very good resolution, and compactness. The tuning of the laser beams and of the detection frequency is computer controlled via a user interface (stage VI) that will be described in the next section.

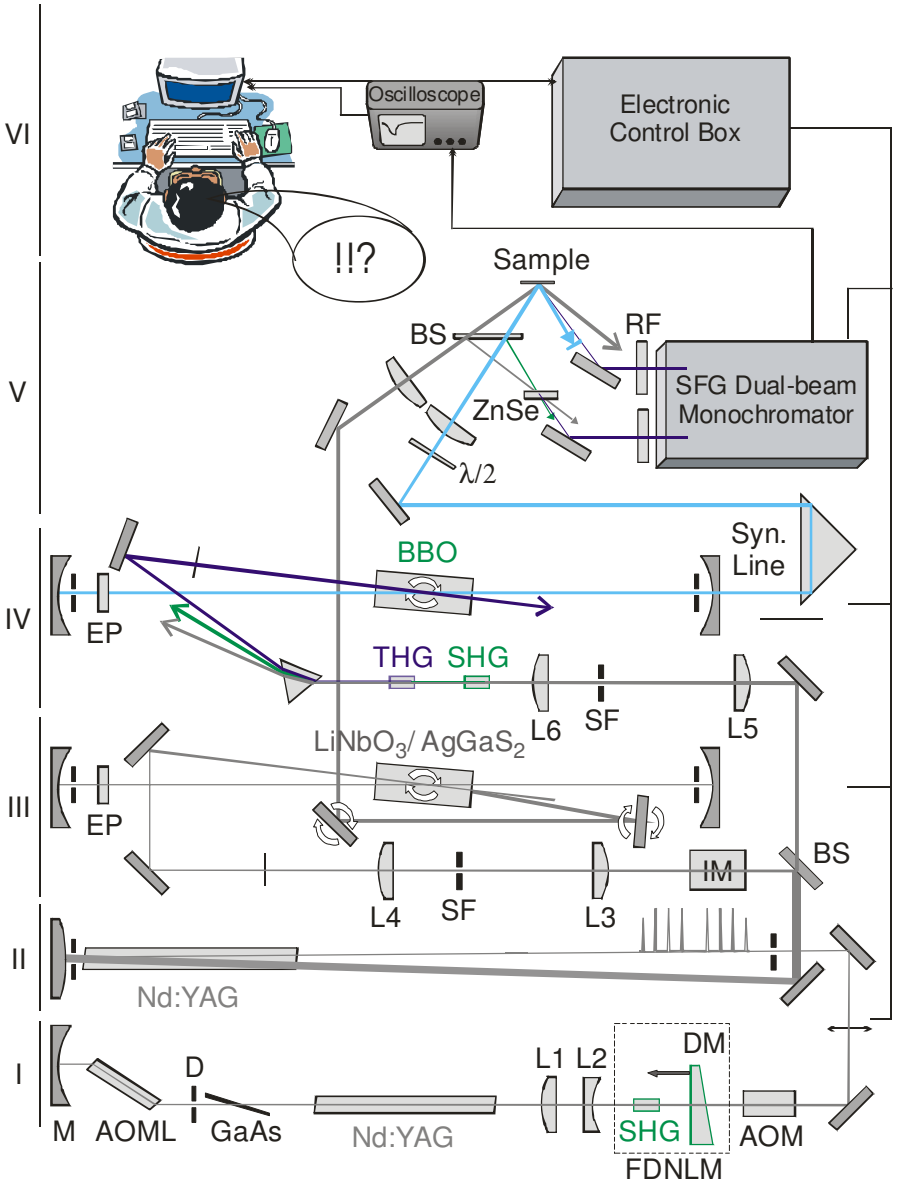

Figure IX-1: Schematic view of the SFG setup. The setup consists of I: Nd:YAG mode-locked oscillator; II: Amplification stage; III: IR OPO; IV: Visible OPO; V: the detection system of the SFG signal; VI: User interface and control system.

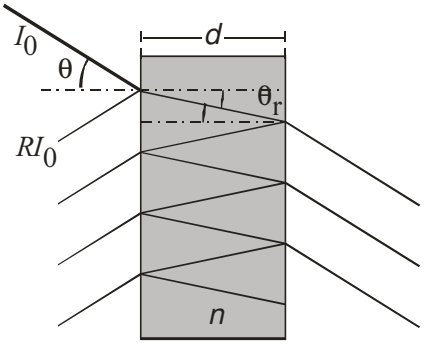

Figure IX-2: Schematic description of an etalon plate of thickness *d* and reflectivity *R*.

Calibration of the $LiNbO_3$ crystal

PRINCIPLE

The basic equation of the intensity transmitted by an etalon plate (EP) (Figure IX-2) at a wavenumber ν, is readily obtained as a function of the angle of refraction (θ_r) and the reflectivity of the surface coatings *R*:

$$T(\tilde{\nu}) = \left[1 + \frac{4}{\pi^2} F^2 \sin^2\left(\pi \frac{\tilde{\nu}}{\Delta\tilde{\nu}}\right)\right]^{-1}, \qquad \text{(VIII.1)}$$

$$\text{with} \quad F = \frac{\Delta\tilde{\nu}_0}{\delta\tilde{\nu}} = \frac{\pi\sqrt{R}}{1-R} \quad \text{and} \quad \Delta\tilde{\nu} = \frac{\Delta\tilde{\nu}_0}{\cos\theta_r},$$

where *F,* which is the ratio of the free spectral range $\Delta\nu_0 = 1/2nd$ and the bandwidth $\delta\nu$, is the finesse of the EP. The transmission function $T(\nu)$ is plotted in Figure IX-3 for normal incidence ($\theta_r = 0°$) and for the following parameters: $d = 0.1$ mm, $n = 1.47$ and $F = 17$ corresponding to a bandwidth $\delta\nu = 2$ cm^{-1}. When the etalon is oriented perpendicular (i.e. the etalon tilt angle $\theta = 0$) to the intracavity OPO beam, its transmission spectrum presents a series of fringes at wavelengths defined by the equation

$$\tilde{\nu} = i\,\Delta\tilde{\nu} \quad \text{where } i \in \mathbb{Z}. \qquad \text{(VIII.2)}$$

In the case of Figure IX-3, *i* would be equal to 91, 92, and 93 according to the first (3094 cm^{-1}), second (3128 cm^{-1}), and third fringe at 3162 cm^{-1}.

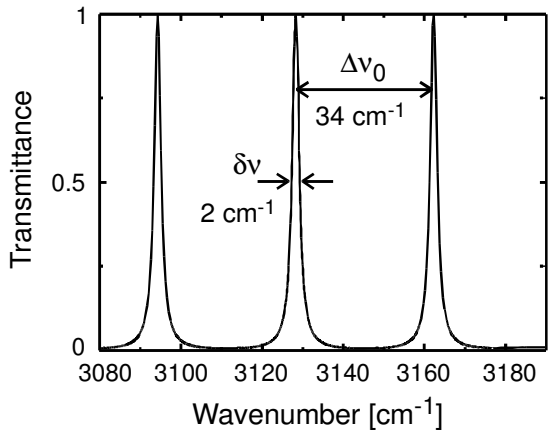

Figure IX-3: Transmission spectrum of an etalon plate of 0.1 mm thickness, the refractive index n = 1.47 and finesse of about F = 17, in the case of normal incidence.

Inserting the etalon plate inside the OPO cavity has the advantage of reducing the bandwidth of the OPO emission to almost the one of the optical pulses, as shown schematically in Figure IX-4. In our setup, we use an etalon plate with bandwidth ~2 cm^{-1} and F = 17. Tuning the OPO output frequency imposes to shift the EP fringe to match the output frequency. This mechanism can be obtained by tilting the EP with respect to the cavity axis.

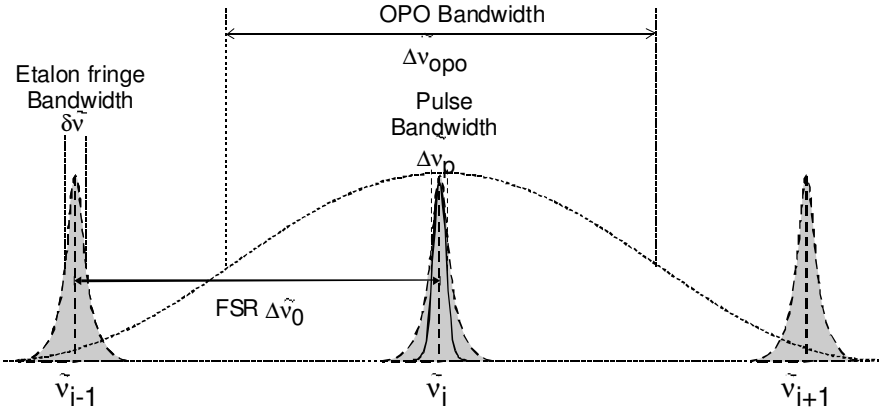

Figure IX-4: Spectral bandwidths of the optical pulse, the OPO generated pulse, and the etalon plate transmission.

For a desired frequency ν, the corresponding internal angle θ_r is given by

$$\theta_r = \text{acos}\left(i \frac{\Delta\tilde{\nu}_0}{\tilde{\nu}} \right). \qquad \text{(VIII.3)}$$

In this equation i is the number of the shifted fringe that can be calculated by

$$i = \text{integer}\left(\frac{\tilde{\nu}}{\Delta\tilde{\nu}_0} \right). \qquad \text{(VIII.4)}$$

It results e.g. that scanning the region from 3094 to 3196 cm^{-1} can be achieved by a rotation of the internal refraction angle θ_r from 0° to 8.4°, that corresponds to a rotation of the EP of 8.4°×1.47 = 12.35°*. Figure IX-5 shows that tuning the EP to an output frequency of 3100 cm^{-1} necessitates shifting fringe number 91 by rotating the EP by 3.565°, but an output frequency of 3140 cm^{-1} necessitates shifting fringe number 92 by rotating the EP by 5.011°, etc. In summary, tuning the output frequency of the OPO with limited bandwidth imposes the rotations of the crystal and of the EP simultaneously. This operation calls for a calibration algorithm that will be described hereafter.

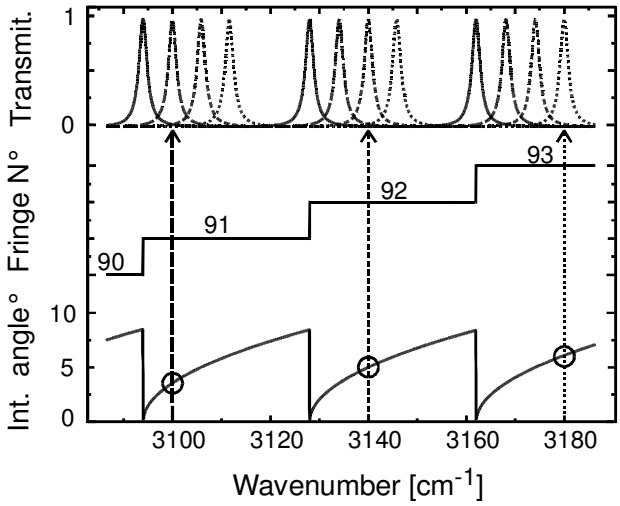

Figure IX-5: Fringe shifting by EP tilting. Upper panel: EP transmission spectrum, Central panel: fringe number. Lower panel: internal angle rotation of EP.

* We use the approximation for small angles $\theta_i \simeq n\theta_r$

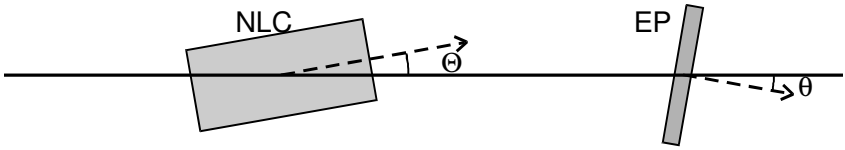

Figure IX-6: Definition of the tilt angles of the etalon plate (θ) and of the nonlinear crystal (Θ).

CALIBRATION PROCEDURE

The calibration procedure is intended to yield the relationship between the output wavelength and the rotation angles of the nonlinear crystal (Θ), and of the inserted etalon plate (θ). Its starts by recording the fringe spectrum obtained by measuring the output intensity of the OPO as a function of the NLC angle Θ when the EP is fixed at normal incidence with respect to the cavity axis. Figure IX-7 shows an algorithmic presentation of the experimental calibration measurement taken for the OPO built on a $LiNbO_3$ crystal.

After the fringe spectrum is taken, an automatic detection of the maxima is performed by a subroutine that permits fringe counting and numbering. Some fringes can be missing due to absorption in the bulk of the crystal: this is the case for fringes between –3 and –1 in the $LiNbO_3$ fringe spectrum. The NLC angle Θ can be represented as a function of the fringe number *i,* and a 6^{th} order polynomial interpolation yields:

$$\Theta(I) = \sum_{s=0}^{6} A_s I^s \quad \text{where } A, I \in \mathbb{R}. \tag{VIII.5}$$

Fringe numbers *i* correspond to integer values of *I.* Then the wavenumbers ν corresponding to a few selected fringes are measured with the monochromator and a second-order polynomial interpolation gives:

$$\tilde{\nu}(I) = \sum_{s=0}^{2} B_s I^s \quad \text{where } B, I \in \mathbb{R}. \tag{VIII.6}$$

As can be shown from Figure IX-7, the wavenumber curve has an almost linear behavior with respect to *i,* which permits us to restrict ourselves to a second-order polynomial while Θ requires a higher-order polynomial, as show in equation (VIII.5).

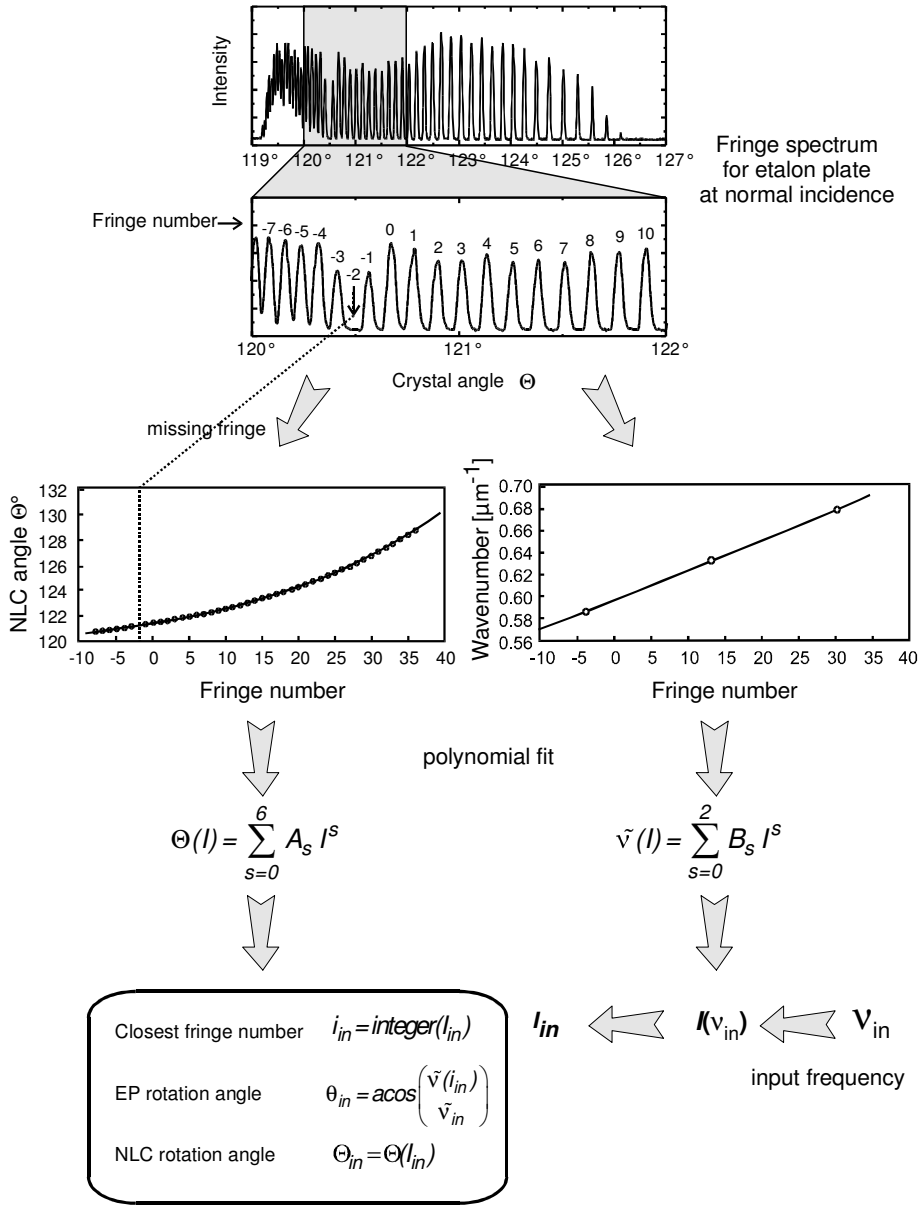

Figure IX-7: NLC calibration procedure flowchart.

Up to this point, the principal part of the calibration has been done. Thus for a selected wavenumber ν_{in} (or wavelength λ_{in}), one can infer the corresponding fringe fit variable I_{in} (the fringe that should be shifted to match the input frequency ν_{in}) from the positive root of equation (VIII.6)

$$\sum_{s=0}^{2} B_s \, {I_{in}}^s - \tilde{\nu}_{in} = 0 \,. \qquad \text{(VIII.7)}$$

From the obtained value of I_{in}, the NLC angle Θ_{in} can be calculated from equation (VIII.5), and the EP angle θ_{in} can be calculated from (VIII.3) recalling that the fringe number i_{in} is the integer part of the fit variable I_{in} .

CALIBRATION OF THE LASER POINTING

The output direction of the idler beam is frequency dependent. Two mirrors placed on two rotation stages can correct this direction as shown in Figure IX-8. The first mirror, M1, ensures that the beam always hits the center of the second mirror (M2). The second mirror keeps the beam output direction constant.

Calibration of the M1 mirror motion is straightforward by using the following procedure. Firstly, we set the M2 mirror at a fixed angle of approximately 45°. We place a vertical slit about 2 mm wide in front of M2 and a power meter (or piezo) which intercepts the beam, as depicted in Figure IX-8. Then we select one idler wavelength and rotate M1 while recording the power reflected by M2, until a maximum is found. This procedure is repeated for a few wavelengths spanning the desired range of operation of the OPO (in our case: 2.5 to 4 μm). The set of detected maxima is then fitted to a second-order polynomial as a function of the idler wavelength:

$$\theta_{m1}(\lambda) = \sum_{s=0}^{2} C_s \lambda^s \,. \qquad \text{(VIII.8)}$$

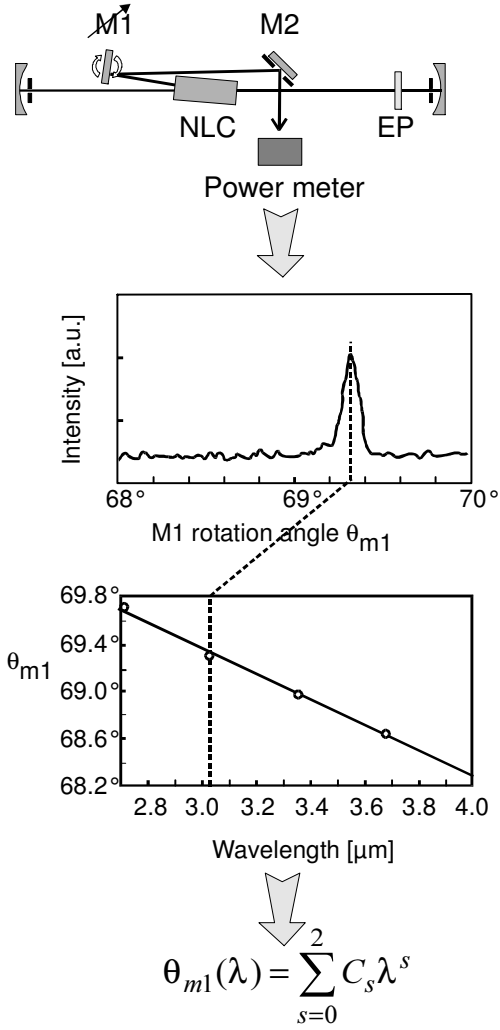

$$\theta_{m1}(\lambda) = \sum_{s=0}^{2} C_s \lambda^s$$

Figure IX-8: Calibration procedure of the M1 mirror.

In order to calibrate M2, we place a pinhole a few meters away from the OPO output, as depicted in Figure IX-9. Then we rotate M2 while recording the power transmitted at large distance through the pinhole and we obtain a set of maxima that can be fitted to the wavelength, with a sixth order polynomial:

$$\theta_{m2}(\lambda) = \sum_{s=0}^{6} D_s \lambda^s \qquad \text{(VIII.9)}$$

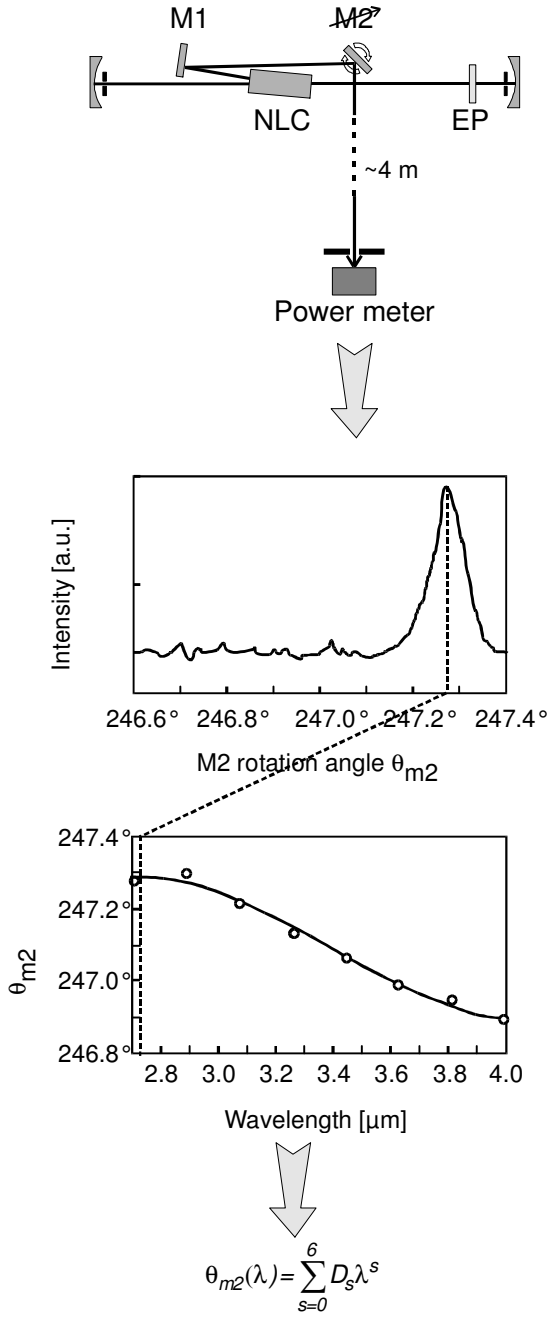

Figure IX-9: M2 calibration procedure flowchart.

A few SFG spectra

In this final section, we shall present experimental SFG spectra obtained with the spectrometer setup that we developed. We have deliberately selected spectra covering different frequency ranges, in order to demonstrate the agility and versatility of our system. In addition, we distinguish different operational modes, depending on whether we have a fixed visible frequency beam or a variable one. In the latter case, the SFG setup is called doubly resonant SFG (DRSFG) spectrometer as it employs the tunability of the visible OPO.

SFG IN THE SPECTRAL RANGE 2.5 μM TO 7μM

The SFG photons are detected by a photomultiplier after passing through a dual-beam monochromator. The SFG spectrometer sensitivity can be evaluated with respect to the characteristics of the laser beams. As in any nonlinear process, the interface SFG response is enhanced upon focusing the two laser beams up to reaching the damage threshold of the sample. Maximum SFG yield can thus be evaluated with regard to the sample thermal response and/or the maximum temperature rise allowed on the surface. For metallic surfaces irradiated by subnanosecond laser pulses, the surface temperature rise is proportional to the incident pulse fluence, independently of the pulse duration and pulse separation larger than 5 ns.[49] This enables to derive a simple scaling law between the maximum SFG yield (SFG_{yield}), the pulse duration (t_{ir}), and the power (P_{ir}) of the tunable infrared beam:[50]

$$SFG_{yield} = \frac{P_{ir}}{t_{ir}}. \qquad \text{(VIII.10)}$$

Equation (VIII.10) was derived assuming that the visible beam power is similar or higher than that of the infrared beam. It shows that, for equivalent infrared power, higher SFG sensitivity is achieved by using shorter pulses. However, a trade off has to be made with the spectral resolution. The sensitivity as given by equation (VIII.10) with t_{ir}=11 ps and P_{ir} = 35 mW* (at 3 μm) with a bandwidth of about 1.8 cm^{-1} compares favorably with the

* 25 Hz × 70 pulses × 20 μJ

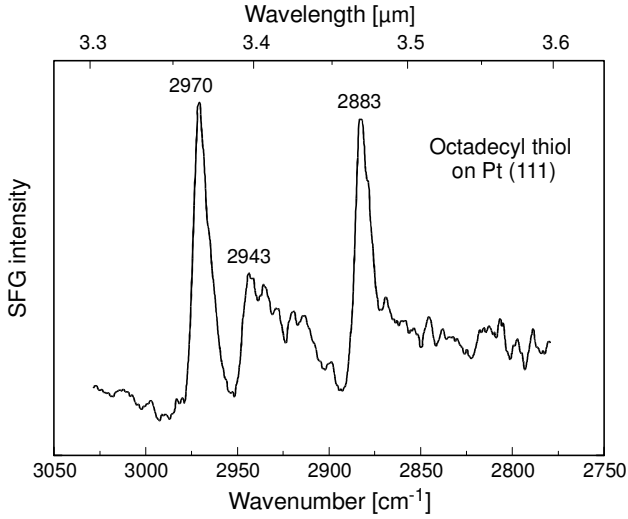

Figure IX-10: SFG Spectrum of octadecylthiol on Pt(111).[42]

characteristics of other SFG spectrometers using an OPG/OPA configuration with t_{ir}=20 ps and P_{ir} = 1.5 mW* at 3 μm with a bandwidth of about 10cm^{-1}. [51]

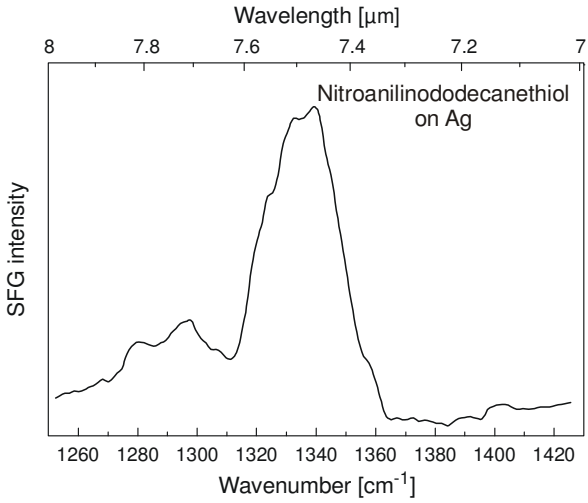

Figure IX-11: SFG spectrum of self-assembled *nitroanilinododecane thiol* on Ag.

* 10 Hz × 150μJ at 3 μm

One can observe that the proposed scheme offers the combined advantages of high spectral resolution (as illustrated by the atmospheric absorption spectrum in Figure VI-7) and high sensitivity. This sensitivity is illustrated by the SFG spectra in Figure IX-10 (for the 3-µm region) and Figure IX-11 (7-µm region) recorded with an acquisition time of 2 s per data point.

SFG IN THE SPECTRAL RANGE FROM 10 TO 20 µM

Figure IX-12 shows SFG spectra of self-assembled monolayers of thiophenol (TP) and 2-naphtalenethiol (NTT) grown on preferentially oriented Ag(111) films deposited on mica. These spectra were recorded from 10 to 20 µm with the DFG stage with the CdSe nonlinear crystal.[52]

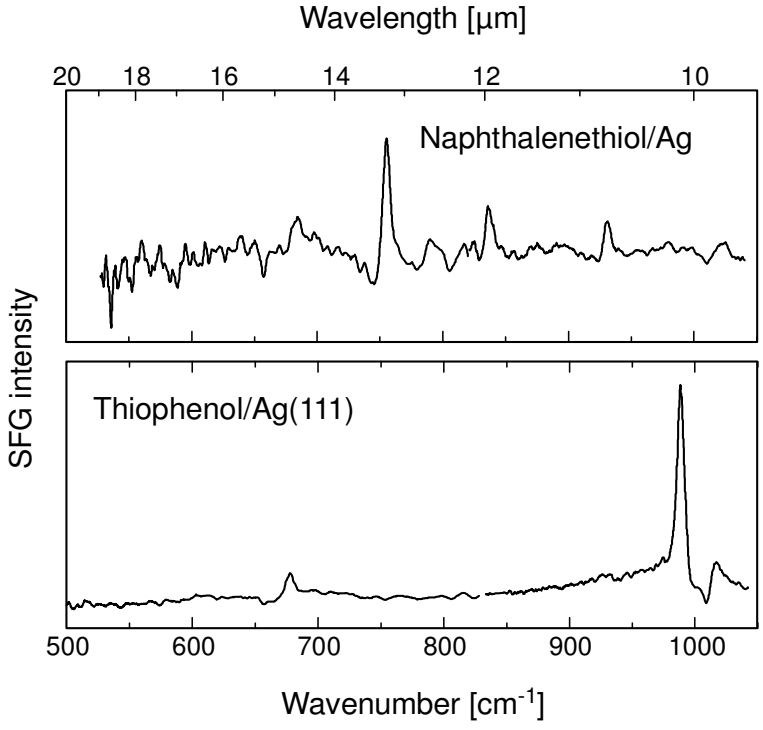

Figure IX-12: SFG spectra acquired from *2-naphthalenethiol* on Ag(111) (upper curve) and *thiophenol* on Ag(111) (lower curve).[37]

DOUBLY RESONANT SFG SPECTROMETER

Previous works have largely demonstrated the adequacy of nonlinear spectroscopy for the study of the vibrational and electronic transitions at interfaces using laser beams tunable either in the infrared or in the visible spectral ranges. [53,54,55,56] Combining the tunability of both visible and infrared beams in one single SFG spectrometer enables to study the coupling between these two types of degrees of freedom. Indeed, Electron-Phonon Couplings (EPC) play a dominant role in various processes such as the accommodation of the adsorbate vibrational energy in surface reactions, the conductivity of polymer films, and super-conductivity. In comparison to HREELS and Resonant Raman Scattering already used for studying EPC in adsorbed molecules, DRSFG is applicable to a wide range of environments and substrates (from insulators to conductors), to well-ordered surfaces, and enables a systematic investigation of EPC at interfaces.

A first step towards that objective has recently been announced[57] by demonstrating the enhancement of the ad-molecule SFG signal when the visible beam frequency is tuned in resonance with an intramolecular electronic transition.

Doubly resonant SFG (DRSFG) also provides a convenient means to modulate the relative importance of the substrate non-resonant contribution to the SFG signal with respect to the resonant signal of the adsorbate. In the past, this objective has been achieved by using difference-frequency generation (DFG),[58] which shifts the frequency of the SFG resonances out of the substrate interband transitions; however, DRSFG is more convenient to use because the generated signal cannot be perturbed by the sample fluorescence which falls in the same spectral range as that of the DFG response. This is clearly illustrated by the results presented in Figure IX-13, showing the SFG spectra of a CH_3-C_6H_4-C_6H_4-$(CH_2)_3$-SH adsorbed on polycrystalline gold[59] and recorded for different values of the visible frequency. The amplitude of the SFG resonances with respect to the non-resonant SFG signal is the smallest for a visible beam frequency of 550 nm, corresponding to the Au interband transition. The relative amplitude of the SFG resonance can be enhanced if the visible beam frequency is tuned to 460 or 720 nm, out of the substrate interband transition.

DRSFG also represents an upgrade of the resonant-SHG spectroscopy that has been used, in the past decade, to study the electronic structure of metallic surfaces. Indeed, as experimentally demonstrated in recent announcements,[60,61] DRSFG of ad-molecules on metallic substrates enables to retrieve both the amplitude and phase of the substrate nonlinear susceptibility. This will enable to achieve better comparison between the experimental data and the theoretical modeling of the metal surface nonlinear response.[62] In addition to providing deeper insight into the substrate electronic structure, DRSFG gives access to the relative phase and amplitude of the adsorbate nonlinear susceptibility with respect to that of the substrate, enabling the determination of the ad-molecule orientation.

Finally, in order to summarize the performances of the setup that we realized during this work, we present in the next Figure (Figure IX-14) a collection of representative SFG spectra that have been recorded so far in our laboratory with our spectrometer, in order to show the vast range of wavelengths now available for SFG investigation. The wavelength range from 2.5 µm up to 4 µm is generated by the $LiNbO_3$ based OPO; the range from 4 µm to 10 µm is covered by the $AgGaS_2$ OPO and the range from 10 to 20 µm is obtained by combining KTP and CdSe crystals.

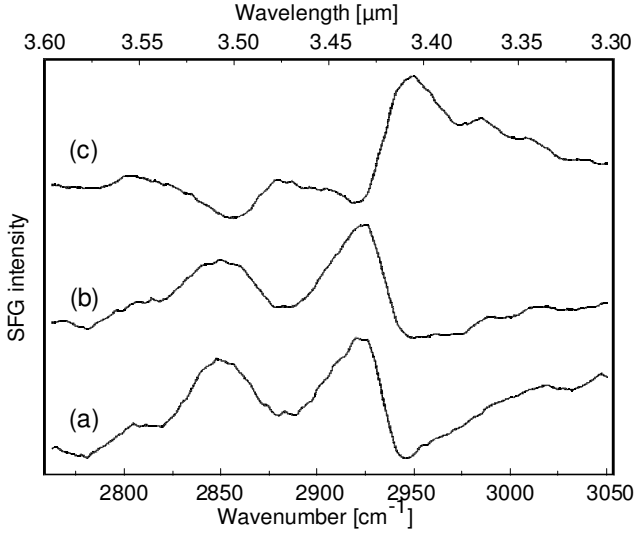

Figure IX-13: SFG spectra of a CH_3-C_6H_4-C_6H_4-$(CH_2)_3$-SH self-assembled monolayer on Au for three visible wavelengths: 720 nm (a), 550 nm (b), and 460 nm (c).

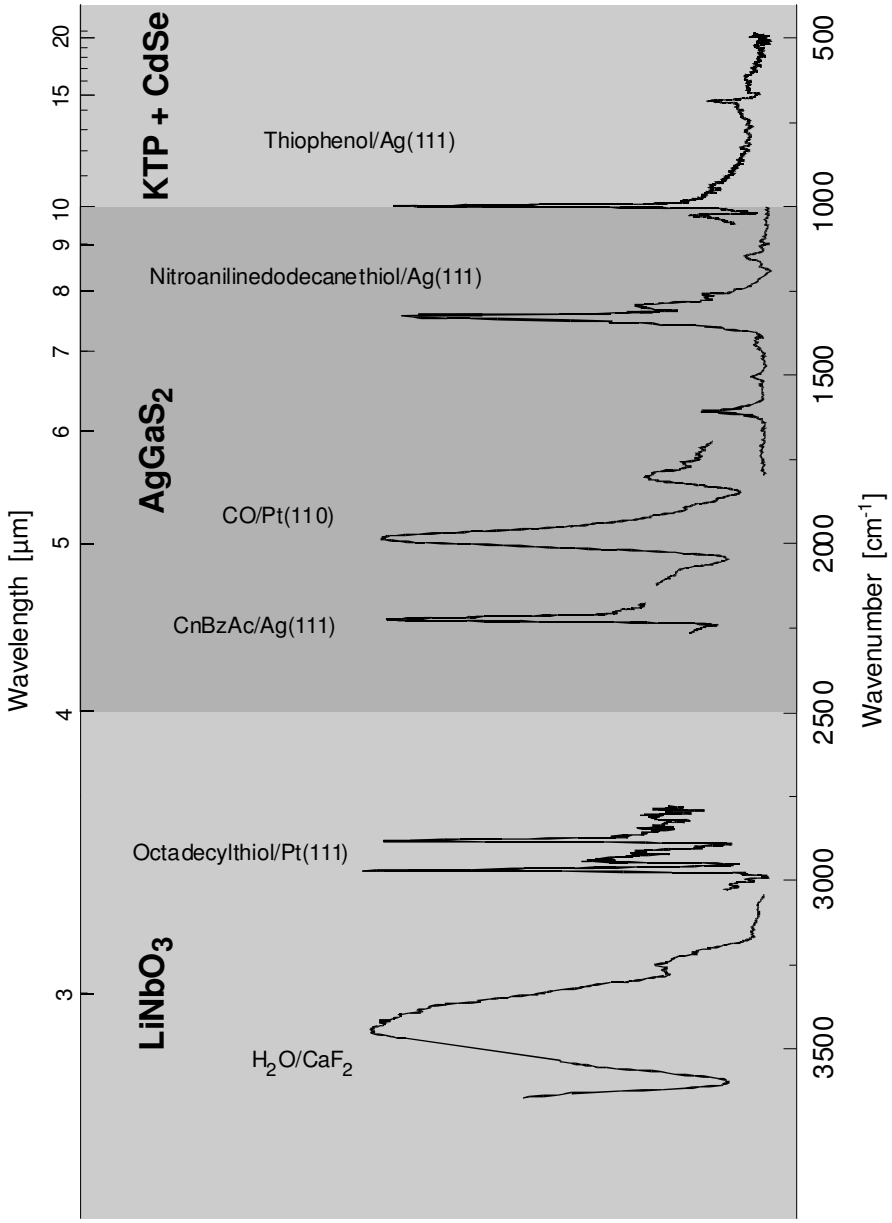

Figure IX-14: Synoptic presentation of a collection of representative SFG spectra recorded with the present setup and covering the wavelength range from 2.5 µm to 20 µm.

Chapter X Conclusion and Perspectives

In this thesis, we presented our achievement on the development of a Sum-Frequency Generation spectrometer dedicated to the study of nonlinear vibrational signatures of samples deposited on centrosymmetric substrates. This vibrational spectroscopy has the following advantages:

- It is sensitive to monolayer samples.
- It enables the determination of molecule orientation.
- Versatility of the methods to explore nonlinear vibrations using the possibility of scanning independently the incident beams wavelengths with detection of single resonances in either the infrared or the visible spectral ranges, and eventual by double resonance on both wavelengths, as shown in Figure X-1. The latter configuration is called doubly resonant Sum-Frequency Generation (DRSFG).[42]
- A special attention is made to the extension of the spectral agility up to 20 μm, with continuous scanning over a large IR domain that will make it a very flexible apparatus for scientific research.[37]
- Usually no vacuum condition is necessary, unless the sample, like C_{60}, is unstable under normal conditions.
- The use of picosecond optical pulses is, in our opinion, a good compromise between improving the sensitivity of the SFG spectrometer (determined by the pulsewidth of 12 ps), and keeping a good spectral resolution (which depends on the pulse bandwidth, ~2 cm^{-1}).
- Moreover, the use of an all-solid-state technology provides a good reliability by keeping a relative simple setup. Both reliability and simplicity are the best arguments for maintenance-free systems.

The SFG spectrometer can be regarded as the assembly of six different parts, as we have seen in chapter IX: (1) the mode-locked picosecond Nd:YAG oscillator, (2) the Nd:YAG amplifier stage, (3) the infrared optical parametric oscillator (IR-OPO), (4) the visible OPO, (5) the sample support with dual-beam monochromator, and (6) the control system.

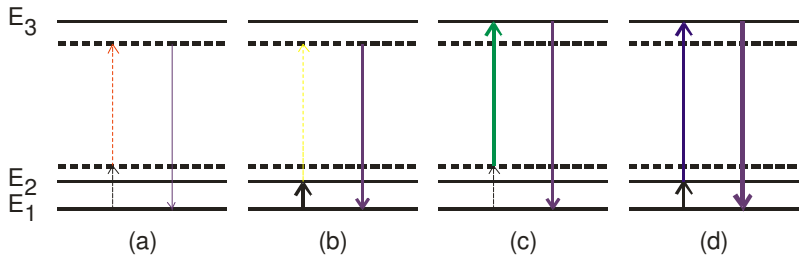

Figure X-1: Three-level model of the SFG processes. The dashed lines are virtual energy levels. We can distinguish four different situations with respect to incident photon energies: (a) Non-resonant SFG (SFG background signal); (b) and (c) correspond to a single resonance SFG on either the infrared photon or the visible photon, respectively; (d) Doubly resonance SFG.

First, we focused our work on the generator of the optical pulses, a 1.5-m cavity built around a Nd:YAG crystal pumped by pulsed flashlamps at a repetition rate of 25 Hz.

The generation of short and stable optical pulses is achieved by combining the passive, positive and the passive, negative mode locking of a FDNLM and a GaAs semiconductor platelet, respectively, as well as active mode locking using an AOML. We demonstrated in a paper, Ref. 30, the possibility of generating optical pulses as short as 12 ps by using this kind of hybrid mode locking, and we described the pulse-shortening mechanism. After that, we concentrated our work on optimizing the laser parameters in order to generate quasi-uniform trains of a hundred pulses of 12 ps pulses, with eight-μJ energy. These characteristics are particularly interesting for pumping synchronously optical parametric oscillators.[34,42]

The improvement of the passive mode locking obtained with a FDNLM in a pulsed laser led to a patent application WO0067351 for this technique.

Further research can be focused on the optimization of the FDNLM configuration using curved dichroic mirrors instead of a flat mirror. This has the advantages of a higher focusing. As a result, we could obtain a faster optical response, a lower walk-off angle, and better phase-matching (as the beam waist is the crystal, so that the beam has planar wavefronts in the crystal), as shown in Figure X-2.

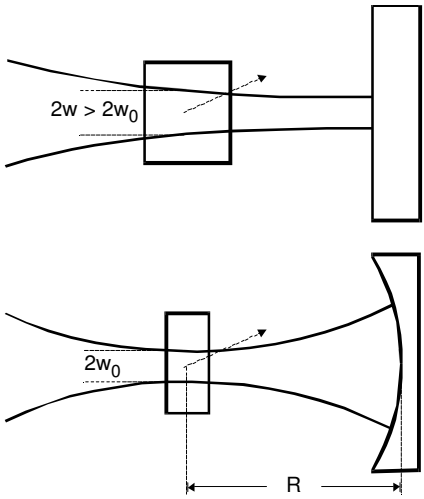

Figure X-2: Beam profiles for flat mirror configuration (upper panel) and for curved mirror configuration (lower panel).

In addition, the hybrid mode locking could be applied to another type of gain media like, for example, Nd:YLF under pulsed regime, which can produce pulses as short as 2 ps (the gain bandwidth is about three times larger than for Nd:YAG[16]).

In SFG spectroscopy, irradiating liquid or ice surfaces at high repetition rate of the optical pulses (here, we speak about the 100-MHz repetition rate that gives a time spacing of about 10 ns between the pulses) could change the physical properties of the surface by heating effects. The latter problem can be solved by selecting one pulse of each train, which results in a very low repetition rate similar to the flashlamps (about 25 Hz in our setup).

The pulse selection, or what it is called a *single-pulse oscillator* can be done in different ways, as shown in Figure X-3. Pulse selection from the oscillator could be done simply by inserting a Pockel's cell (PC) outside the cavity (upper panel) or, in a more complicated manner, inside the cavity, as shown in the central and lower panels of Figure X-3. Inserting the PC inside the cavity can give better pulse to noise ratio and higher energy. We propose the configuration presented in the lower panel in Figure X-3, which combines pulse selection and pulse amplification using multitiming PC.

Figure X-4 illustrates the PC timing with the corresponding beam paths in the cavity. In the beginning, we leave the oscillator function as usual, then we fire the PC in order to rotate the polarization of the optical pulse that circulate in the auxiliary cavity formed by M_2 and the DM. In this case, the pulse will not be limited in intensity by the GaAs platelet that permits multi-amplification in the YAG rod depending on the number of round trip inside the auxiliary cavity before the depletion of YAG rod energy. Preliminary results have shown that pulse energy five times larger that one extracted by simple-timing scheme and about 10 times when PC is outside the cavity; moreover, this configuration has the advantages to clarify the operation of the hybrid mode locking in decoupling the part of FDNLM from that of GaAs.

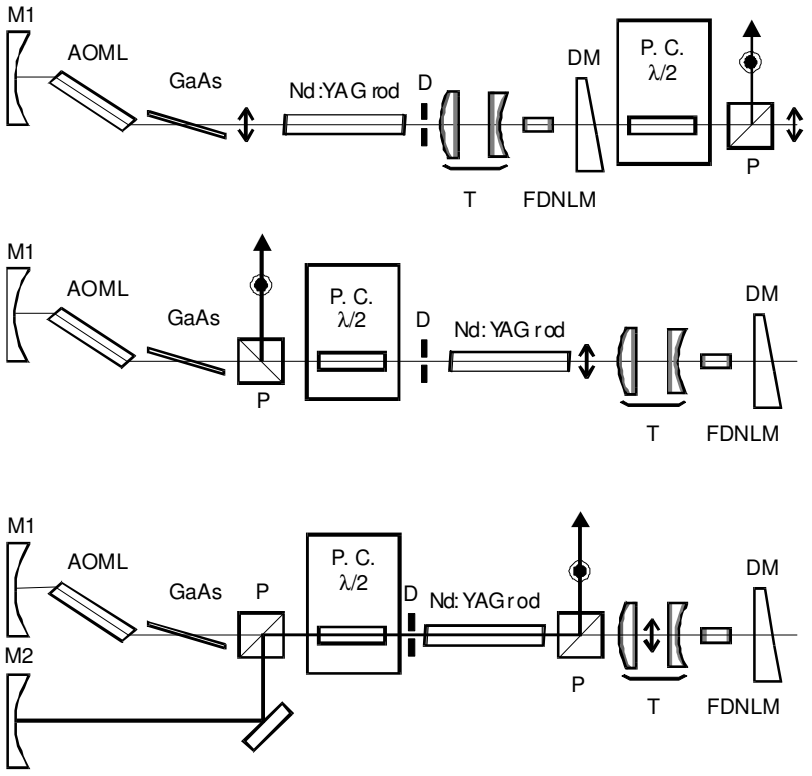

Figure X-3 : Single-pulse selection from the laser oscillator. In the upper panel, the PC is installed outside the cavity. In the central panel, the PC is installed inside the cavity. In the lower panel, PC is inside the cavity with multi-timing configuration.

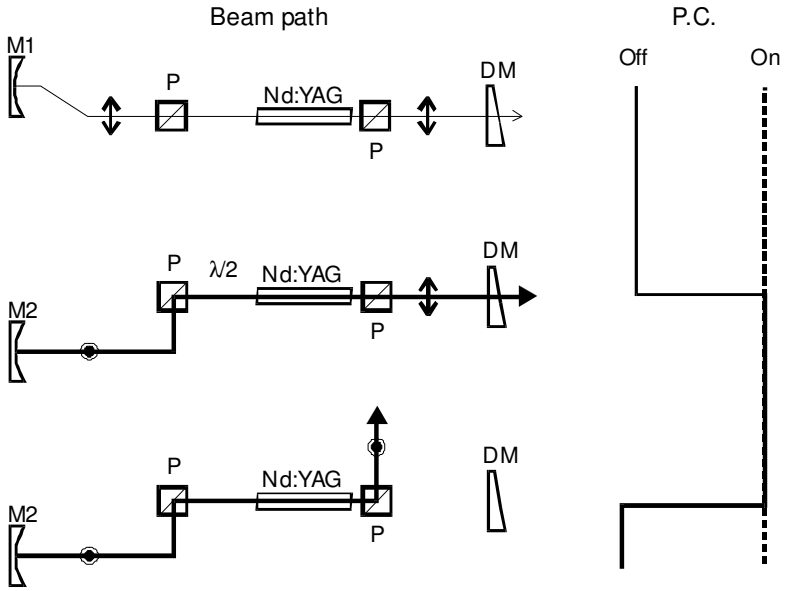

Figure X-4: Beam paths for different PC timing. The PC is represented as half-wave plate.

For a single-pulse SFG spectrometer, the pulse selection stage will be followed by an optical parametric generator and amplifier (OPG/OPA) in order to tune the pulse wavelength and then illuminate the sample.

This apparatus will be also tunable in the visible spectral range and in the IR spectral range from 2.5 up to 20 μm, using all-solid-state picosecond technology.

Finally, we hope that these small features added on the SFG setup will make it a powerful tool for scientific research at the fundamental as well as at the applied level.

Chapter XI Appendices

Nonlinear reflection coefficient of FDNLM (Stankov model)

As we have already described, the operation of FDNLM is based on two passes through the NLC optimized for SHG. In both passes, the parameter Γ is equal to zero, which means the coupled-wave equations, under CW and plane wave assumptions, take the following solutions

$$\begin{aligned} u(\xi) &= \operatorname{sech}(\xi + m\xi_c) \\ v(\xi) &= \tanh(\xi + m\xi_c) \end{aligned}, \tag{XI.1}$$

where u and v are the normalized FW and SH field amplitudes that satisfy the relation

$$u^2(\xi) + v^2(\xi) \equiv 1. \tag{XI.2}$$

In this case, ξ is the normalized propagation distance inside the nonlinear medium and ξ_c is a constant determined by the initial condition as follows

$$\xi_c = \operatorname{arctanh}(V_0), \tag{XI.3}$$

where $V_0 = v(0)$ [*].

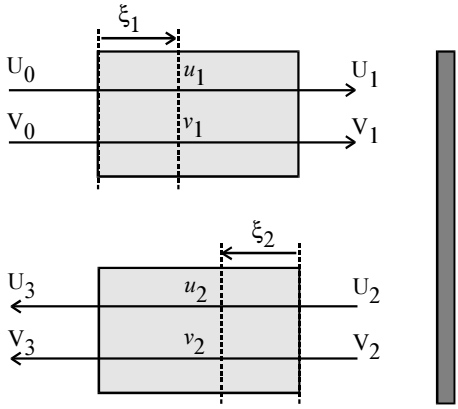

Figure XI-1: FDNLM scheme.

[*] We prefer to use capital letters to indicate the initial values.

The parameter *m* takes +1 for the first pass through the crystal (SH generation, under perfect phase-matching conditions), and –1 for the second pass (down conversion process).

FIRST PASS $M = 1$

The initial conditions are

$$\begin{aligned} U_0 &= 1 \\ V_0 &= 0 \end{aligned} \tag{XI.4}$$

From Eq. (XI.1) the amplitudes *u* and *v* are given at position ξ for *m*=1 by

$$\begin{aligned} \xi_1 &= Cz \\ u_1(\xi_1) &= \operatorname{sech}(\xi_1) \\ v_1(\xi_1) &= \tanh(\xi_1) \end{aligned} . \tag{XI.5}$$

Where *C* is a constant depending on the nonlinear crystal properties. Then, at the exit surface of the NLC, the amplitudes take the following values

$$\begin{aligned} U_1 &= u(\xi_{1ex}) = \operatorname{sech}(\xi_{1ex}) = \sqrt{1-\eta} \\ V_1 &= v(\xi_{1ex}) = \tanh(\xi_{1ex}) = \sqrt{\eta} \end{aligned} . \tag{XI.6}$$

After the reflection by the dichroic mirror (DM), the amplitudes of FW and SH waves will be

$$\begin{aligned} U_2 &= \sqrt{(1-\eta)R_\omega} \\ V_2 &= \sqrt{\eta} \end{aligned} . \tag{XI.7}$$

These values are the initial conditions for the second pass through the nonlinear crystal.

SECOND PASS $M=-1$

In the second pass, the FW and SH wave amplitudes are given by Eq. (XI.7). at position ξ_2

$$\begin{aligned} u_2(\xi_2) &= \sqrt{B}\,\mathrm{sech}(\xi_2 - \xi_c) \\ v_2(\xi_2) &= \sqrt{B}\,\tanh(\xi_2 - \xi_c) \end{aligned}, \tag{XI.8}$$

where

$$\begin{aligned} B &= U_2^2 + V_2^2 = (1-\eta)R_\omega + \eta \\ \xi_2 &= C\sqrt{B}\,z = \sqrt{B}\,\xi_1 \\ \xi_c &= \mathrm{acrtanh}\left(\frac{V_2}{\sqrt{B}}\right) = \mathrm{acrtanh}\left(\sqrt{\frac{\eta}{B}}\right) \end{aligned} . \tag{XI.9}$$

At the exit surface of the crystal the amplitude of the FW can be seen as the reflected amplitude of the FW by the FDNLM device. Therefore, the nonlinear reflection coefficient is given

$$R_{NL} = \left(\frac{U_4}{U_0}\right)^2 = B\left[1 - \tanh^2(\xi_{2ex} - \xi_{2c})\right]. \tag{XI.10}$$

Note that using Eq. (XI.6) yields:

$$\xi_{2ex} = \sqrt{B}\,\xi_{1ex} = \sqrt{B}\,\mathrm{arctanh}\left(\sqrt{\eta}\right). \tag{XI.11}$$

Substitute Eq. (XI.9) and (XI.11) into (XI.10)

$$R_{NL}(\eta, R_\omega) = B\left[1 - \tanh^2\left(\sqrt{B}\,\mathrm{arctanh}\sqrt{\eta} - \mathrm{acrtanh}\sqrt{\frac{\eta}{B}}\right)\right] \tag{XI.12}$$

finally gives the nonlinear reflection coefficient as a function of η and R_ω.

Fit of autocorrelation measurements with a set of Gaussian pulses

We prefer to fit the autocorrelation (AC) measurement by using functions that share the same FWHM and peak intensity (or normalized intensity data). This procedure conserves the FWHM (τ_{AC} =12.44 ps) and the peak intensity, which are physical parameters.

Figure XI-2 shows a variety of optical functions defined by:

$$I_G(t) = \exp\left[-4\ln 2\left(\frac{t}{FWHM}\right)^2\right], \tag{XI.13}$$

Sech pulse

$$I_S(t) = \operatorname{sech}^2\left(1.763\frac{t}{FWHM}\right), \tag{XI.14}$$

Lorentzian form

$$I_L(t) = \left[1+4\left(\frac{t}{FWHM}\right)^2\right]^{-1}, \tag{XI.15}$$

and ArcSinhc function

$$I_{AS}(t) = \left[\frac{\operatorname{arcsinh}(4.213t)}{4.213t}\right]^2. \tag{XI.16}$$

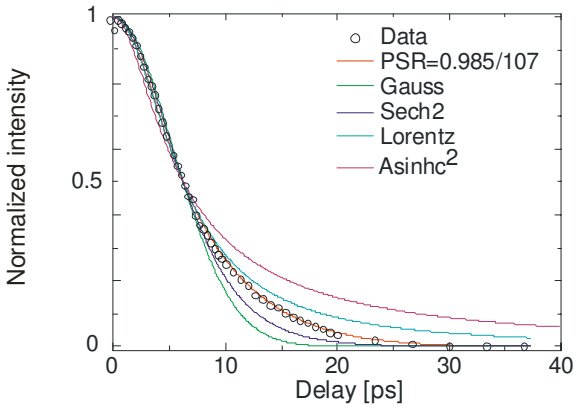

Figure XI-2: AC experimental data fitted with different optical functions that share the same FWHM and peak intensity.

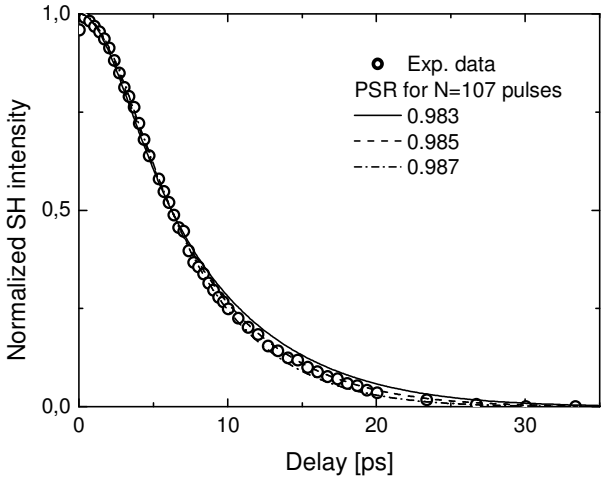

Figure XI-3: Fit with GSP for fairly compressed pulses.

We can see that all these functions do not fit very well the AC data form. For the latter reason we introduce Gaussian Set Pulses (GSP) that gives the total intensity function for a superposition of N Gaussian pulses.

$$I_{GSP}(t) = \frac{1}{N}\sum_{n=1}^{N} \exp\left[-4\ln 2\left(\frac{t}{PSR^{n-1}\tau_1}\right)^2\right], \qquad \text{(XI.17)}$$

where τ_1 is the pulsewidth of the first pulse.
Calculating this function at $t=\tau_{AC}/2$ will give

$$I_{GSP}(\tau_{AC}/2) = \frac{1}{2} = \frac{1}{N}\sum_{n=1}^{N} \exp\left[-4\ln 2\left(\frac{\tau_{AC}/2}{PSR^{n-1}\tau_1}\right)^2\right]. \qquad \text{(XI.18)}$$

For weakly compressed pulses (PSR ~1), the value of each exponential function at $t = \tau_{AC}/2$ can be obtained by developing each function around the point $t = (PSR^{n-1}\tau_1)/2$. and then solving the equation(XI.18) will give

$$PSR_{app} = \frac{\tau_{AC}}{\tau_1} \cong N\frac{1-PSR}{1-PSR^N}PSR^{N-1}. \qquad \text{(XI.19)}$$

In order to fit with this function we need to know the number of averaged optical pulses, which is about 107 pulses. Then we can choose the *PSR* for the best fitting of the data. Note that τ_1 is calculated from Eq.(XI.19), as follows

$$\tau_1 = \frac{\tau_{AC}}{PSR_{app}}. \qquad \text{(XI.20)}$$

Figure XI-2 shows that GSP fits perfectly the AC measurement for *PSR*=0.985 (ratio between two successive pulses) with PSR_{app} (ratio between the first and the first one) is about 0.387. Moreover Figure XI-3 shows the sensitivity of the fit the low intensity parts (*N* intensity lower than 0.5) for *PSR* value to fit for a tolerance about 0.2 %, which give a good tool to determine the *PSR* value. In the other hand, we can tolerate variation on the number of pulses *N* by about 11%, which is about two orders of magnitude higher than the *PSR* tolerance.

References

[1] H.W. Mocker and J.R. Collins, *Applied Physics Letters* 7, 270 (1965).

[2] A.J. DeMaria, D.A. Stetser, H. Heynau, *Applied Physics Letters* **8**, 174 (1965).

[3] A. Del Corno, G. Gabetta, and G.C. Reali, *Optics Letters* **15**, 734 (1990).

[4] K.A. Stankov, *Applied Physics B* **45**, 191 (1988).

[5] I. Buchvarov, S. Saltiel, K.A. Stankov, D. Georgiev, *Optics Communications* **83**, 65 (1991).

[6] K.A. Stankov, and J. Jethwa, *Optics Communications* **66**, 41 (1988).

[7] K.A. Stankov, *Optics Letters* **14**, 359 (1989).

[8] K.A. Stankov, *Applied Physics Letters* **58**, 2203 (1991).

[9] K.A. Stankov, V.P. Tzolov, and M.G. Mirkov, *Optics Letters* **16**, 639 (1991).

[10] K.A. Stankov, *Applied Optics* **28**, 942 (1989).

[11] I. Buchvarov, G. Christov, and S. Saltiel, *Optics Communications* **107**, 281 (1994).

[12] I. Buchvarov, S. Saltiel, and S. Gagarskii, *Optics Communications* **118**, 51 (1995).

[13] O.V. Chekhlov, and V.A. Zaporozhchenko, *J. Optical Society of America B* **15**, 210 (1998).

[14] W. Koechner, *Solid-State Laser Engineering*, ISBN: 3-540-65064-4, Springer (1999).

[15] J.E. Geusic, H.M. Marcos, L.G. Van Uitert, *Applied Physics Letters* **4**, 1704 (1964).

[16] A.A. Kaminskii, *Laser Crystals*, ISBN: 3-540-09576-4, Springer (1981).

[17] A.E. Siegman, *Lasers*, ISBN: 0-935702-11-3, University Science Books (1986).

[18] D.J. Kuizenga, D.W. Phillion, T. Lund, A.E. Siegman, *Optics Communications* **9**, 221 (1973).

[19] D.J. Kuizenga, IEEE, QE, **17**, 1694 (1981).

[20] A. Yariv, *Optical waves in crystals*, ISBN: 0-471-43081-1, Wiley-Interscience (1984).

[21] E.G. Sauter, *Nonlinear Optics*, ISBN: 0-471-14860-1, Wiley-Interscience (1996).

[22] N. Bloembergen, *Nonlinear Optics*, ISBN: 981-02-2598-9, World Scientific (1996).

[23] D.A. Kleinman, *Physical Review* **126**, 1977 (1962).

[24] P.E. Ciddor, *Applied Optics* **35**, 1566 (1996).

[25] http://patapsco.nist.gov/mel/div821/Wavelength/Ciddor, (2004)
[26] R.C. Eckardt and J. Reintjes, *IEEE J. of Quantum Electronics* **20**, 1178 (1984).
[27] J. Reintjes and R.C. Eckardt, *Applied Physics Letters* **30**, 91 (1977).
[28] I.V. Tomov, R. Fedosejevs, and A.A. Offenberger, *IEEE J. of Quantum Electronics* **18**, 2048 (1982).
[29] J.R.M. Barr, *Optics Communications* **70**, 229 (1989).
[30] A.A. Mani, Ph. Hollander, P.A. Thiry, and A. Peremans, *Applied Physics Letters* **75**, 3066 (1999).
[31] V. Kubecek, S. Kumazaki, Y. Takagi, K. Yoshihara, and C. Reali, *Jap. J. Applied Physics* **30**, L1805 (1991).
[32] A.A. Mani, L. Dreesen, Ph. Hollander, C. Humbert, Y. Caudano, P.A. Thiry, and A. Peremans, *Applied Physics Letters* 79, 1945 (2001).
[33] V.G. Dmitriev, G.G. Gurzadyan and D.N. Nikogosyan, *Handbook of Nonlinear Optical Crystals*, ISBN: 3-540-65394-5, Springer (1991).
[34] A.A. Mani, L. Dreesen, Ph. Hollander, P.A. Thiry, and A. Peremans, Photomec'99-ETE'99, 153 (1999).
[35] I.B. Zotova and J. Ding, *Applied Optics* **40**, 6654 (2001).
[36] S. Guha, E.W. Van Stryland, and M.J. Soileau, *Optics Letters* **10**, 285 (1985).
[37] A.A. Mani, Z. D. Schultz, B. Champagne, C. Humbert, L. Dreesen, Y. Caudano, A. Gewirth, J.O. White, P.A. Thiry, and A. Peremans. *Optics Letters* **29**, 274 (2004).
[38] A. Dhirani and P. Guyot-Sionnest, *Optics Letters* **20**, 1104 (1995).
[39] K.S. Abedin, S. Haider, Y. Konno, C. Takyu, and H. Ito, *Applied Optics* **37**, 1642 (1998).
[40] U. Simon, Z. Benko, M.W. Sigrist, R.F. Curl, and F.K. Tittel, *Applied Optics* **32**, 6650 (1993).
[41] D. Andreou, *Optics Communications* **23**, 37 (1977).
[42] A.A. Mani, L. Dreesen, C. Humbert, Ph. Hollander, Y. Caudano, P.A. Thiry, A. Peremans, *Surface Science* **502**, 261 (2002).
[43] P. Guyot-Sionnest, R. Superfine, J.H. Hunt and Y.R. Shen, *Chemical Physics Letters* **144**, 1 (1988).
[44] Q. Du, E. Freysz, Y.R. Shen, *Science* **264**, 826 (1994).
[45] A. Peremans et A. Tadjeddine, *Physical Review Letters* **73**, 3010 (1994).
[46] X.C. Su, Y.R. Shen, and A. Somorjai, *Physical Review Letters* **77**, 3878 (1996).

[47] P. Guyot-Sionnest, in Laser Techniques for state-selected and State-to-State Chemistry, edited by N. Cheuk-Yu (Porc. SPIE 1858, 1993), pp 334.

[48] R. Braun, B.D. Casson, C.D. Bain, E.W.M. van der Ham, Q.H.F. Vrehen, and E.R. Eliel, A.M. Briggs, and P.B. Davies, *J. of Chemical Physics* **110**, 4834 (1990).

[49] J.M. Hicks, L.E. Urbach, E.W. Plummer, and H.-L. Dai, *Physical Review Letters* **61**, 2588 (1988).

[50] A. Peremans, A. Tadjeddine, W.Q. Zheng., P. Guyot-Sionnest, P. Remy, G Ryschenkow, M. Buck, Y. Caudano, L.-M. Yu, P.A. Thiry, B. Bourguignon, H. Dubost, B. Draggnea, and S. Carrez, *Nuclear Instruments and Methods A* **375**, 657 (1996).

[51] Q. Du, E. Freysz, Y.R. Shen, *Science* **264**, 826 (1994).

[52] A. A. Mani, L. Dreesen, C. Humbert, P. Hollander, Y. Caudano, P. A. Thiry and A. Peremans, *Applied Surface Science* **237**, 443 (2004).

[53] Y.R. Shen, *Nature* **337**, 519 (1989).

[54] T.F. Heinz, F.J. Himpsel, and E. Palange, E. Burstein, *Physical Review Letters* **63**, 644 (1989).

[55] L.E. Urbach, K.L. Percival, J.M. Hicks, E.W. Plummer, and H.L. Dai, *Physical Review B* **45**, 2769 (1992).

[56] L. Dreesen, C. Humbert, Y. Sartenaer, Y. Caudano, C. Volcke, A. A. Mani, A. Peremans, P. A. Thiry, S. Hanique, and J.-M. Frère, *Langmuir* **20**, 2701 (2004).

[57] M.B. Raschke, Y.R. Shen, abstract G13.005 of the March meeting of the American Physical Society, March 2001.

[58] A. Le Rille, A. Tadjeddine, W. Quan Zheng, and A. Peremans, *Chemical Physics Letters* **271**, 95 (1997).

[59] T.F. Heinz, F.J. Himpsel, and E. Palange, E. Burstein, *Physical Review Letters* **63**), 644 (1989).

[60] T.-A. Ishibashi and H. Onishi, abstract O-37 of the conference "Vibration at Surfaces 10", June 2001.

[61] C. Humbert, L. Dreesen, A.A. Mani, Y. Caudano, J.J. Lemaire, P.A. Thiry, and A. Peremans, abstract O-17 of the conference "Vibration at Surfaces **10**", June 2001.

[62] T.A. Luce, and K. H. Bennemann, *Physical Review B* **58**, 15821 (1998).